CANADIAN THESES

THÈSES CANADIENNES

NOTICE

The quality of this microfiche is heavily dependent upon the quality of the original thesis submitted for microfilming. Every effort has been made to ensure the highest quality of reproduction possible.

If pages are missing, contact the university which granted the degree.

Some pages may have indistinct print especially if the original pages were typed with a poor typewriter ribbon or if the university sent us an inferior photocopy.

Previously copyrighted materials (journal articles, published tests, etc.) are not filmed.

Reproduction in full or in part of this film is governed by the Canadian Copyright Act, R.S.C. 1970, c. C-30.

AVIS

La qualité de cette microfiche dépend grandement de la qualité de la thèse soumise au microfilmage. Nous avons tout fait pour assurer une qualité supérieure de reproduction.

S'il manque des pages, veuillez communiquer avec l'université qui a conféré le grade.

La qualité d'impression de certaines pages peut laisser à désirer, surtout si les pages originales ont été dactylographiées à l'aide d'un ruban usé ou si l'université nous a fait parvenir une photocopie de qualité inférieure.

Les documents qui font déjà l'objet d'un droit d'auteur (articles de revue, examens publiés, etc.) ne sont pas microfilmés.

La reproduction, même partielle, de ce microfilm est soumise à la Loi canadienne sur le droit d'auteur, SRC 1970, c. C-30.

THIS DISSERTATION
HAS BEEN MICROFILMED
EXACTLY AS RECEIVED

LA THÈSE A ÉTÉ
MICROFILMÉE TELLE QUE
NOUS L'AVONS REÇUE

NL-339 (r. 86/06)

Canada

SOME PROPERTIES OF THE SEMIMAGNETIC SEMICONDUCTOR ALLOY

$(Cd_{1-z}Mn_z)(Te_{1-y}Se_y)$

by

SAMIR CHEHAB

Thesis

Submitted to the School of Graduate Studies

in partial fulfillment of the requirements

for the degree of Ph.D. in Physics

University of Ottawa

Department of Physics

Ottawa, Ontario

K1N 6N5

1986

ISBN 0-315-33271-9

UNIVERSITÉ D'OTTAWA
UNIVERSITY OF OTTAWA

ABSTRACT

The thesis gives details of some of the crystallographic magnetic and optical properties of the semimagnetic semiconductor alloy system $(Cd_{1-z}Mn_z)(Te_{1-y}Se_y)$.

Polycrystalline samples were prepared over most of the composition range, Debye-Scherrer X-ray powder photographs were used to investigate the equilibrium conditions and to determine the lattice parameter values for the various samples, in which the presence of one, two or three phases was established. The resulting isothermal sections at 600 and 960°C are presented.

Measurements of low-field magnetic susceptibility and electron spin resonance (ESR) were made as a function of temperature on the various samples of both the zinc blende and wurtzite phase fields of the alloy system.

From the susceptibility measurements, values were obtained for the spin-glass transition temperature T_g, the Curie-Weiss temperature θ and the Curie constant C. The variation of these three parameters with both composition and crystal structure were considered in some detail. A study of the exchange interaction using the T_g values, suggested that the magnetic spins were indirectly coupled to each other through antiferromagnetic superexchange, involving virtual transitions between the valence band and a non-localized 3d band. Predictions of the exchange parameter values, based on these results, agreed with those determined previously from other types of measurements.

The ESR linewidth was studied as a function of composition and temperature. The linewidth was observed to increase with decreasing temperature. At lower temperatures, the ESR line became asymmetrically broadened and then split into two parts well above any magnetic transition point. The dependence of the linewidth on temperature results were analyzed using a theory based on inhomogeneous broadening.

The room temperature optical energy gap was measured as a function of composition by wavelength modulated reflectance. Temperature-dependent energy gap measurements were also carried out on the diagram edge $Cd_{1-z}Mn_zSe$; two different structures were observed in the low temperature regions, corresponding to the fundamental transition and to the transition from the crystal-field-split valence band to the conduction band. An extra increase ΔE in the fundamental energy gap was observed at low temperature and was found to increase with Mn content. ΔE which was attributed to magnetic contribution was estimated by extrapolating the high temperature behaviour. The results were then analyzed using an equation which depended on the spin-glass transition temperature T_g. Previously obtained data for the observed crystal-field and spin-orbit splittings were used to estimate the variation of the Mn d-orbitals contribution to the valence band, with Mn concentration.

Magnetic susceptibility and ESR experiments were also carried out on the various samples of the cubic NaCl phase field, which are derived from the antiferromagnetic compound MnSe. The anomalies and thermal hysterisis observed in the magnetic susceptibility results

could be interpreted in terms of an incomplete structural phase transition from NaCl-type phase to hexagonal NiAs-type. The results for the $Cd_{1-z}Mn_zSe$ alloys showed that the low temperature phase transition is strongly influenced by the substitution of Mn by Cd. In the ESR work, the results obtained for the Mn^{2+} resonance linewidth dependence on temperature, were analyzed in terms of a critical effect near the Neel temperature T_N, and a paramagnetic effect at high temperature. Values of the Curie-Weiss temperature θ and of the Neel temperature T_N obtained from the ESR analysis, were used together to estimate the nearest and next nearest neighbour exchange interaction parameters J_1 and J_2.

ACKNOWLEDGMENTS

I would like to express my sincere gratitude to my supervisor, Professor John C. Woolley for his assistance and invaluable suggestions during the course of this work. I would also like to thank Professor Woolley for the opportunity of working with him and for his guidance which was always available throughout the preparation of this thesis.

I wish to express my sincere gratitude to my supervisor Professor Armen Mannogian for his assistance and encouragement, and for the many valuable discussions with him.

Many thanks are also due to Professor Gilles Lamarche for his aid in the magnetic susceptibility experiments and for the useful discussions with him.

I would like to acknowledge the help I received from Professor Richard Hodgson in quantum mechanical calculations and to thank Mr. Tom Donofrio, a friend and classmate, for the many beneficial discussions and for the help received on the use of the computing facilities.

I would also like to thank my colleagues Dr. Kajornyod Yoodee and Dr. Miguel Quintero for their interest and suggestions concerning the optical work.

Special thanks are due to Mr. Bei Wah Chan for handling the technical aspects of the ESR measurements, and to Mr. Munkid El-Najjar for technical assistance on some of the magnetic susceptibility measurements.

The financial support provided by Professors John C. Woolley and Armen Manoogian from their NSERC grants is gratefully acknowledged.

My gratitude also goes to a very special person, my fiancee Judith, for her patience, understanding and love.

I wish to pay special tribute to my parents who supported me in my early education, especially to my mother; I would not have made it without her loving support and to her I dedicate this work.

Finally, I wish to thank Mrs. Line Robitaille who did an excellent job in typing this manuscript.

TABLE OF CONTENTS

LIST OF FIGURES

LIST OF TABLES

Chapter I

Introduction

Considerable interest has been shown in recent years in the properties associated with a novel class of semiconductors known as semimagnetic semiconductors (SMSC's). The term "semi" in semimagnetic, was coined by R.R. Galazka [1], and arises from an analogy with the same term in the word semiconductor. In a semiconductor, the carrier concentrations may be varied by introducing impurities into the crystal lattice. If these impurities are magnetic, then the semiconductor will possess some magnetic properties which may be changed by varying the concentration of the impurities. The general usage of the term "semimagnetic" has come to encompass all semiconductor systems which possess a magnetic component whose concentration may be varied.

The most common SMSC's are the solid solutions of the type $II_{1-z}\ Mn_z\ VI$, such as $Hg_{1-z}\ Mn_z\ Te$, $Cd_{1-z}\ Mn_z\ Te$, $Cd_{1-z}\ Mn_z\ Se$ etc. The most interesting aspect of these mixed crystals is the presence of the half-filled $3d^5$ levels of the manganese ions. The localized magnetic moment of the $3d^5$ electrons interact with each other as well as with band electrons via exchange interaction, giving rise to unusual magnetic and magneto-optical phenomena [1-3].

In the present work an investigation of certain properties of the semimagnetic semiconductor system $[Cd_{1-z}Mn_z][Te_{1-y}Se_y]$ will be presented. This alloy system can be represented by a square as shown in fig. 1.1. Each point in the square represents a particular value of

z and y and hence a particular composition. The system $Cd_{1-z}Mn_zTe$ and $Cd_{1-z}Mn_zSe$ which were mentioned above, are represented by the left hand edge and the right hand edge, respectively, of the diagram. The corners of the square are the binary compounds CdTe, CdSe, MnSe and MnTe. We note that a sample with a particular composition may be referred to by a label of the form (Z,Y) where Z and Y are the percentage compositions of Mn and Se.

Various types of measurement, have previously been performed on both pseudo-binary systems $Cd_{1-z}Mn_zTe$ [4-6] and $Cd_{1-z}Mn_zSe$ [6-7]. Some of these measurements will be extended to the entire alloy system $[Cd_{1-z}Mn_z][Te_{1-z}Se_y]$ where Te is progressively replaced by Se or vice versa. This would provide much more data to analyze which in turn would shed more light on the properties of such materials and may, therefore, reveal previously undetected effects.

The following measurements, were carried out on the system. First, in chapter 2, the variation of the lattice parameters with composition were measured, and hence the limits of solid solutions were also determined. Some magnetic measurements were then performed on the single-phase regions of the diagram, in order to study the magnetic behaviour of the alloys. These measurements involved magnetic susceptibility and electron spin resonance experiments, described in chapters 3, 4 and 6. Next, in chapter 5, the variation of the energy gap as a function of composition was measured. The dependence of the energy gap on temperature was also studied for $Cd_{1-z}Mn_zSe$ edge of the diagram.

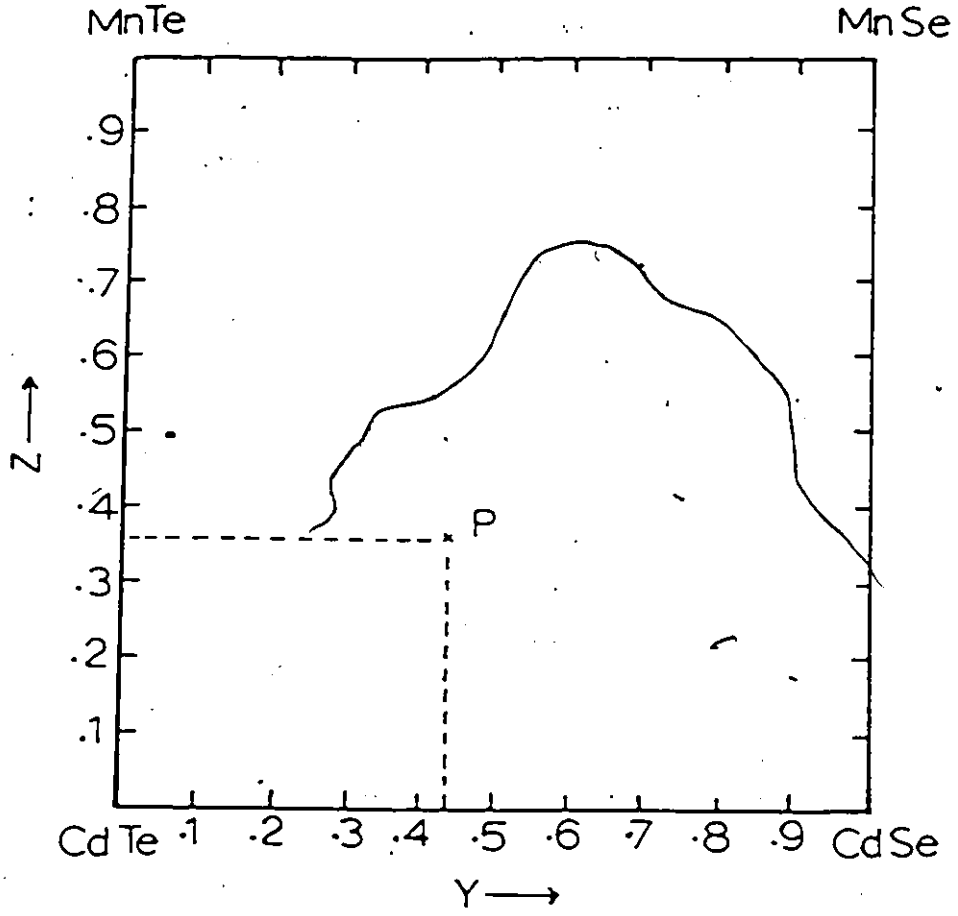

Fig. 1.1. Representatif diagram for (Cd_{1-z} Mn_z) (Te_{1-y} Se_y). Any point "P" in the diagram represents a sample of composition z and y .

References

1- J.A. Gaj, Proc. 15th Int. conf. Physics of Semiconductors, Kyoto, (1980).

J. Phys. Soc. Japan 49 suppl. A 797 (1980).

2- J.K. Furdyna, J. Appl. Phys. 53, 7637 (1982)

3- N.B. Brandt and V.V. Moshchalkov, Advences in Physics 33, 193 (1984).

4- J.A. Gaj, R.R. Galazka, M. Nawrocki, Solid State Commun. 25, 193 (1978).

5- R.R. Galazka, S. Nagata, P.H. Keeson, Phys. Rev. B22, 3344 (1980).

6- S. Oseroff, Phys. Rev. 25B, 6584 (1982).

7- H. Wiedemeier and A.B. Sigai, J. Electrochem. Soc. 117, 551 (1970).

Chapter 2

Solid Solution and Lattice Parameter Values

2.1 Introduction

An alloy is a combination of two or more metals, or of metals and non-metals. It may consist of a single phase or of a mixture of phases, depending on the composition and temperature of the alloy, provided that the alloy is at equilibrium and held under the constant atmospheric pressure. However, the term has come to be used in semiconductor work to indicate a material in which single phase behaviour occurs over an appreciable composition range.

The initial requirement in the study of any of the physical properties of an alloy is to determine the range of single-phase solid solutions which can be obtained; and this certainly applies to our alloy system $(Cd_{1-z}Mn_z)$ $(Te_{1-y}Se_y)$. The boundary edges of the diagram of this system, all of which have been investigated previously, are the pseudo-binary sections CdTe - CdSe [1], CdTe - MnTe [2], CdSe - MnSe [3,4] and MnTe - MnSe [5]. These show wide ranges of solid solution in all four pseudo-binary sections and a variation in these ranges with temperature. Two isothermal sections of the $(Cd_{1-z}Mn_z)$ $(Te_{1-y}Se_y)$ phase diagram obtained during the investigation of solid solubility are presented in this chapter as functions of z and y.

2.2 Preparation of samples and X-ray Work:

A little more than one hundred samples of different

compositions had to be made up in order to cover the whole diagram. In each case one gram samples were prepared using the standard melt and anneal technique. The appropriate amounts of the elements were weighed and then sealed under vacuum in small quartz ampoules which has previously been carbonized to prevent any interaction of the components with the quartz. The material was held at 1200°C for approximately 15 min, quenched and then annealed to equilibrium at a chosen temperature; temperatures of 960 and 600°C were used in the present work. The condition of each sample after annealing was determined from X-ray diffraction experiments.

X-ray diffraction data at room temperature were obtained with Debye-Scherrer powder photographs (Straumanis film loading method) using CuKα radiation and 114.6 mm cameras, manufactured by Phillips (Holland).

It was found that, for samples in the form of solid ingots, very long annealing times were necessary to attain an equilibrium condition. In the initial work the annealing temperature of 600°C was used and very few samples were in a state approaching equilibrium. The annealing temperature was raised to 960°C and annealing times of up to 3 months were required before equilibrium conditions (as indicated by sharp high angle diffraction lines) were obtained. As had been found previously for other alloys [6], equilibrium was attained much more quickly if the sample was powdered after melting and quenching and the powder was compressed and annealed. Thus a large number of samples were made and annealed in compressed powdered form. In these cases, samples annealed at 960°C for 2 weeks showed equilibrium had been

attained, and those annealed at 600°C required a little longer. However, when optical measurements were to be made, solid samples were required and so samples of each type were prepared in the single-phase ranges.

As indicated below, the 960°C section gave a larger single-phase field for the wurtzite structure and, since this was of interest for magnetic measurements, most of the samples were annealed at this temperature. However, sufficient work was done at 600°C to determine the form of the diagram at the latter temperature.

2.3 Lattice parameter measurements:

The process of measuring a lattice parameter from a powder photograph begins with the measurement of the positions of the diffraction lines on the film. A travelling microscope is used for this purpose. Knowing the position of the diffraction lines allows us to deduce each corresponding Bragg angle θ, and thus $\sin^2\theta$. The latter is directly related to the crystal lattice parameters, the values of which can now be determined. A cubic crystal gives diffraction lines whose $\sin^2\theta$ values satisfy the following equation (Ref. (7)):

$$Q = \frac{\sin^2\theta}{\lambda^2/4} = \frac{1}{a_c^2}(h^2 + k^2 + \ell^2) \qquad (2.1)$$

where λ is the wavelength of the X-ray radiation, a_c is the lattice parameter and h,k,ℓ are Miller indices.

In the hexagonal case: $$Q = \frac{\sin^2\theta}{\lambda^2/4} = 4/3 \cdot \frac{h^2 + hk + k^2}{a_h^2} + \frac{\ell^2}{c_h^2} \qquad (2.2)$$

where a_h and c_h are the hexagonal lattice parameters.

The observed values of $\sin^2\theta$ always contain small systematic

errors; and that is mainly due to off-centering of the specimen and to absorption in the specimen. A precise parameter measurements would then require the removal of such errors from the data. Two methods were used in order to achieve this, the first one is known as the extrapolation method, the second one as the internal calibration method (Ref. (7)).

Extrapolation method:

It is mostly used in the case of cubic crystal where there is one unknown parameter to determine (a_c). A value of a_c is obtained from each diffraction line (by using eq. (2.1)). Now the true value a_{oc} of the lattice parameter can be found by plotting a_c against $f(\theta) = (\frac{\cos^2\theta}{\sin\theta} + \frac{\cos^2\theta}{\theta})$ which approches zero as θ approches 90°. This plot is linear at least at higher θ values, and extrapolates to a_{oc} at $f(\theta) = 0$. Least squares fit is used to draw the best straight line through the experimental points which minimizes the effect of the random errors.

Internal calibration method:

We used this method in the case of noncubic crystals (namely hexagonal) where there are two unknown parameters to determine. This method is based on a calibration of the camera film by means of a substance of known lattice parameter such as silicon. The powder of the specimen whose parameter is to be determined, is mixed with a small amount of powdered silicon, and a pattern is made of the composite powder. The true angle θ for any diffraction line from the silicon can

be calculated, and then the difference between the observed and calculated values of $\sin^2\theta$ for the silicon is calculated and plotted as a function of the observed values of $\sin^2\theta$, a calibration curve is then obtained. The errors represented by the ordinates of such a curve can now be applied to each of the observed $\sin^2\theta$ for the diffraction lines of the specimen, in order to find the true $\sin^2\theta$. Knowing the true values of $\sin^2\theta$, one can apply the principles of the least squares method to eq. (2.2) and obtain a set of two equations with the two unknowns a_h and c_h. These two equations can be simultaneously solved, giving the required values of the parameters a_h and c_h.

2.4 Results and Analysis:

The equilibrium samples showed one-, two- and three-phase behaviour, with the phases observed corresponding to the structure shown by the four compounds i.e. CdTe (cubic, zinc blende), CdSe (hexagonal, wurtzite), MnTe (hexagonal, NiAs) and MnSe (cubic, NaCl). Lattice parameter values were determined for all of the single phase samples and for those two- or three-phase samples, where such parameters values were useful in determining the limits of solid solubility or the form of the two- or three-phase fields.

The variation in the lattice parameter with composition for the various fields is shown in Figs. 2.1-2.5. Figures 2.1 and 2.2 show the variation in the zinc blende parameter a for samples annealed at 600°C; curves of a versus z at constant y and of a versus y at constant z are given. In Figs. 2.3 and 2.4 the variation in the parameters a and c of the wurtzite phase are given for samples annealed at 960°C; in

each case the variation in the parameter with z for lines of constant y is shown. The values of the parameter a for the NaCℓ structure for samples annealed at 960°C are given in Fig. 2.5; curves of a versus z at constant y are shown.

In order to use these results in locating the different phases boundaries, one has to remember that, first of all, in any single-phase field, the lattice parameter always varies in smooth and continuous way with composition. In a two-phase region "tie lines" exist, along which the relative amounts of the two phases change but their compositions and hence lattice parameters remain constant. However, the compositions of the two phases and consequently their lattice parameters will vary along any line which is not a "tie line". A three-phase field should be always a triangle the corners of which fix the compositions of the three phases, so that the lattice parameters remain constant throughout this field.

As a consequence of these "rules" in most cases, a break in curve of a against the relevant composition parameter gives a good indication of a field boundary; for example the lattice parameter usually changes at a different rate in the two-phase field than in the single-phase field, which causes a break in the parameter composition curve. Each break in each lattice parameter curve would then allow us to determine one point on the corresponding phase boundary on the isothermal section. Let us consider fig. 2.2 for example, in this figure, the lattice parameter a shows a linear variation with y in the single-phase field as indicated by the solid lines. The strange and irregular behaviour in the dashed lines of the two-phase field is due

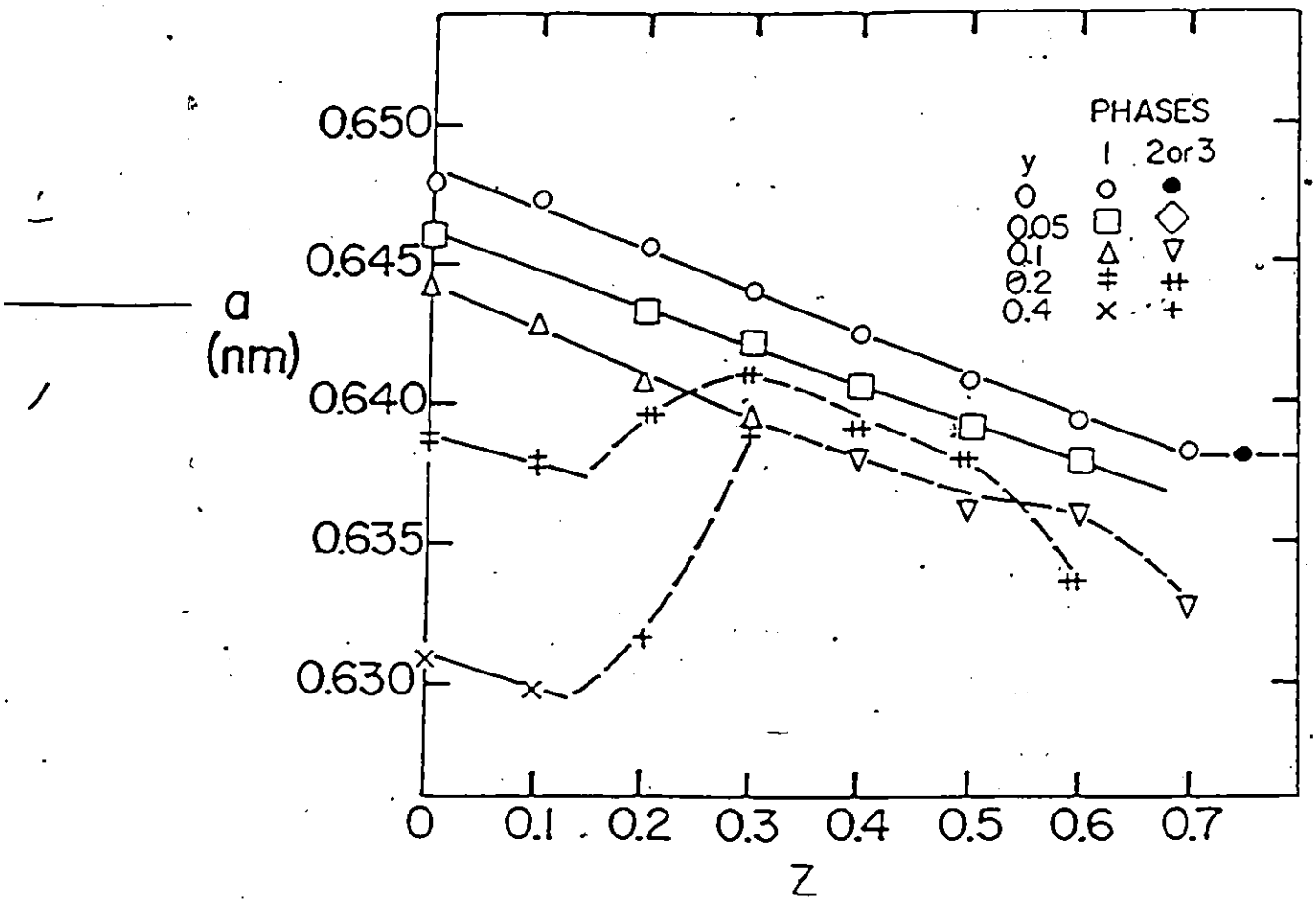

Fig. 2.1. Variation of lattice parameter a with z for lines of constant y for the cubic zinc blende phase α.

Values of y shown in figure

—— single phase field —— two or three phase field.

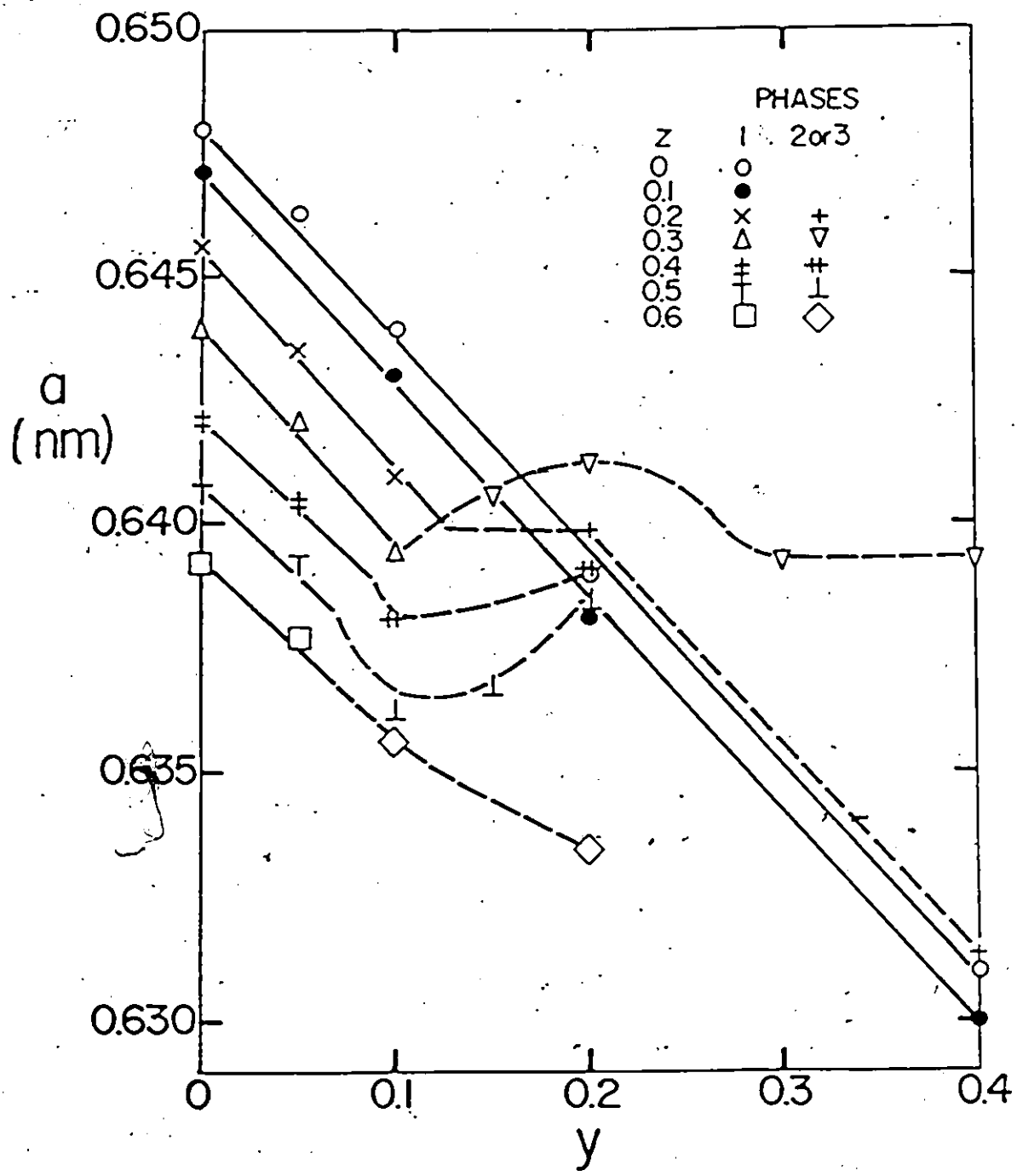

Fig. 2.2. Variation of lattice parameter a with y for lines of constant z for the cubic zinc blende phase α.

Values of z shown in figure

—— single phase field —— two or three phase field.

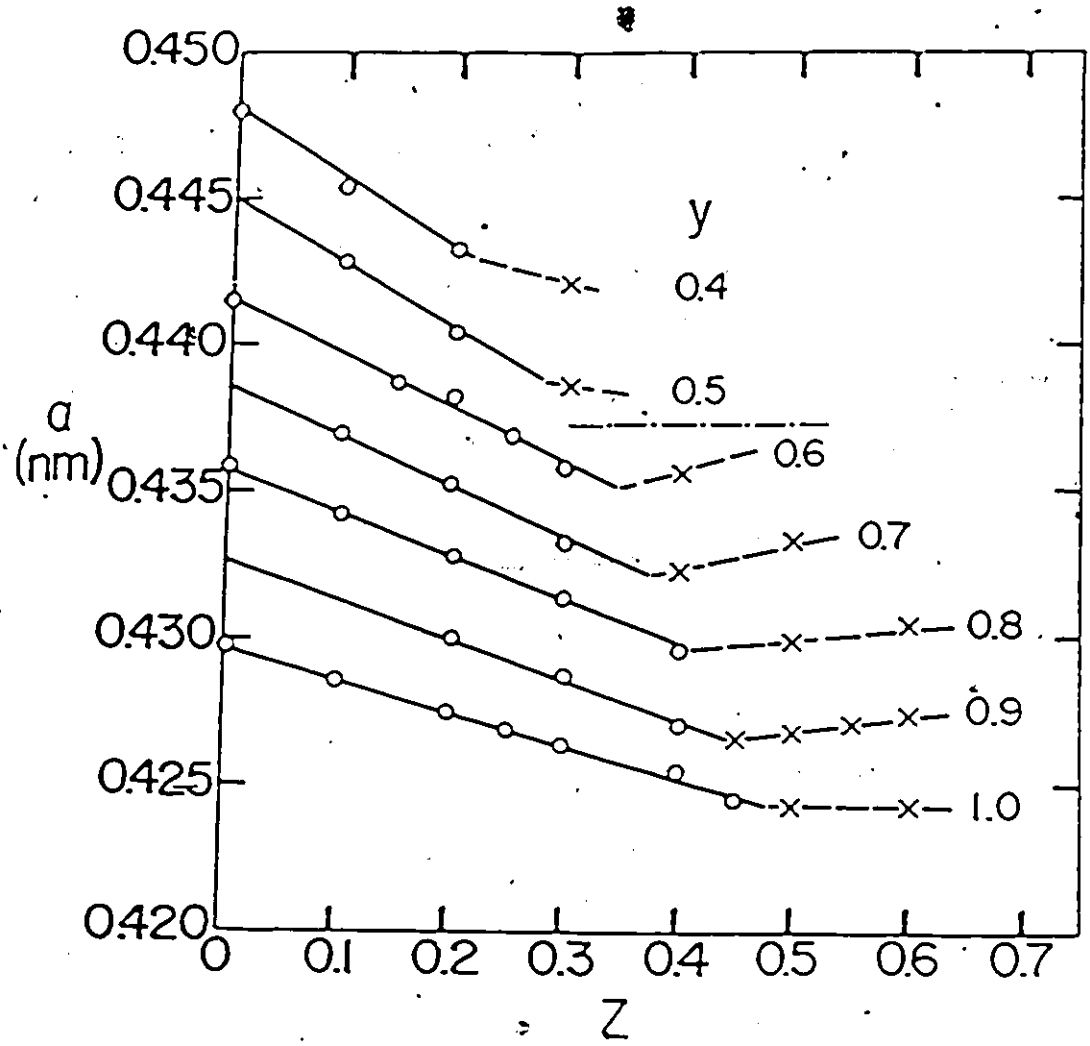

Fig. 2.3. Variation of lattice parameter a with z for lines of constant y for hexagonal wurtzite phase β.

Values of y shown in figure

o single phase sample x two or three phase sample

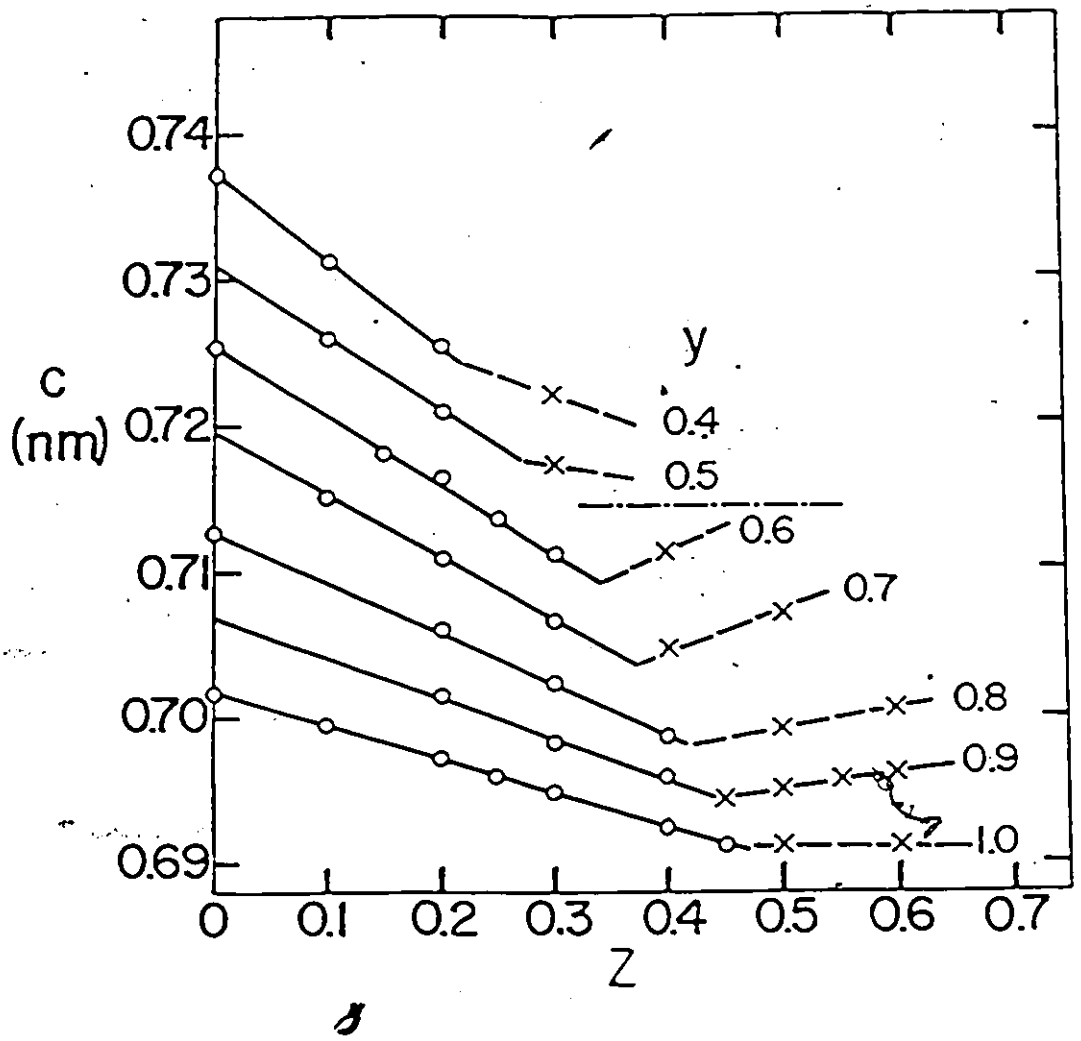

Fig. 2.4: Variation of lattice parameter c with z for lines of constant y for hexagonal wurtzite phase β.

Values of y shown in figure

o single phase sample x two or three phase sample.

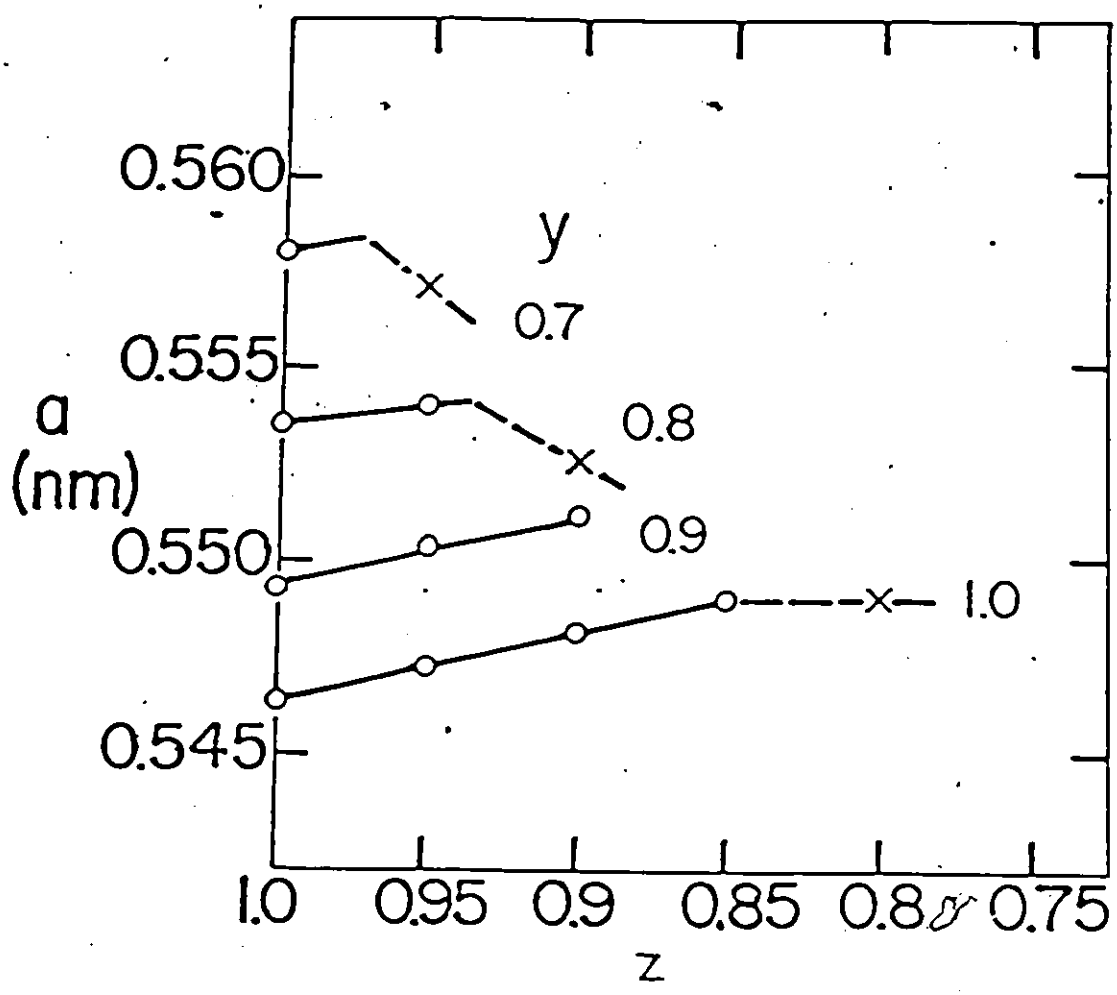

Fig. 2.5. Variation of lattice parameter a with z for lines of constant y for cubic sodium chloride phase δ.

Values of y shown in figure

o single phase sample x two or three phase sample.

to the fact that the section considered does not lie along a tie line. When any of the lines pass through the three-phase region, a remains constant. For example if we look at the line with z = 0.3, this line is straight from y = 0 up to y around 0.1 where a break occurs indicating the end of the single-phase field. Then the line shows kind of a bump until just before y = 0.3 where it breaks again and becomes horizontal indicating the end of the two-phase field and the beginning of the three-phase field. Note that different symbols were used in order to distinguish between the single-phase points and the two-phase points. The analysis of the remaining figures 2.1, 2.3, 2.4 and 2.5 was also carried out in the same manner. However, in attempt to construct the two isothermal sections shown in Figs. 2.6 and 2.7, it was not possible to do this using only these results, they had to be used in conjunction with other informations obtained from x-ray photographs observations and with previously published data for the pseudo-binary edges [1-5]. In most cases for samples which were not single phase, we were able to see on the x-ray photographs the diffraction lines belonging to two or three different phases, then to identify these phases and, where possible, measure the corresponding lattice parameters. In addition, in some previous work done on the pseudo-binary edges [1-5], the variation of the range of solid solution with temperature for these edges was studied in some detail. All these data and information put together, helped us to determine the boundaries of the various fields, and the change of these boundaries when changing the annealing temperature. To illustrate this, let us consider for example the wurtzite B phase in the 960°C isothermal

section; from the breaks in the parameter composition curves in Figs. 2.3 and 2.4, we could determine the single-phase field boundary. Beyond this boundary, any existing two-phase field must be crossed by "tie lines", along each of which the composition and hence the lattice parameter of each of the two phases remains constant and has the same value as that at the intersection of the tie line with the corresponding two-phase field boundary [7,8]. Since the lattice parameter values at the two-phase fields boundaries as well as, where possible, inside these fields could be obtained for both phases, we were able to estimate the positions of the tie lines in the $\alpha + \beta$ and $\beta + \delta$ two-phase regions. These are shown in Fig. 2.6. Again from Figs. 2.3 and 2.4, we see that the change in the variation in the a and c parameters with z in the two-phase region, indicates a change from $\alpha + \beta$ to $\beta + \delta$ between $y = 0.4$ and $y = 0.5$, and this is reinforced by the observed phases in neighbouring two-phase samples. Between these two-phase field, there is a three-phase field confirmed by checking the presence of three-phases α, β and δ in samples of this region. Now for the α-phase, an identical method was used in determining the boundaries, however it is to be noted that in this case three two-phase fields were observed ($\alpha + \beta$, $\alpha + \delta$ and $\alpha + \gamma$) with two three-phase fields ($\alpha + \beta + \delta$ and $\alpha + \gamma + \delta$) separating them. However, some of the fields involving δ and γ were approximately estimated from previous work [2-5]. Finally, this lengthy investigation resulted in the 960°C isothermal section shown in Fig. 2.6. Less work was carried out for the 600°C section, but sufficient samples were investigated to determine the forms of the α and β single-phase fields. However the

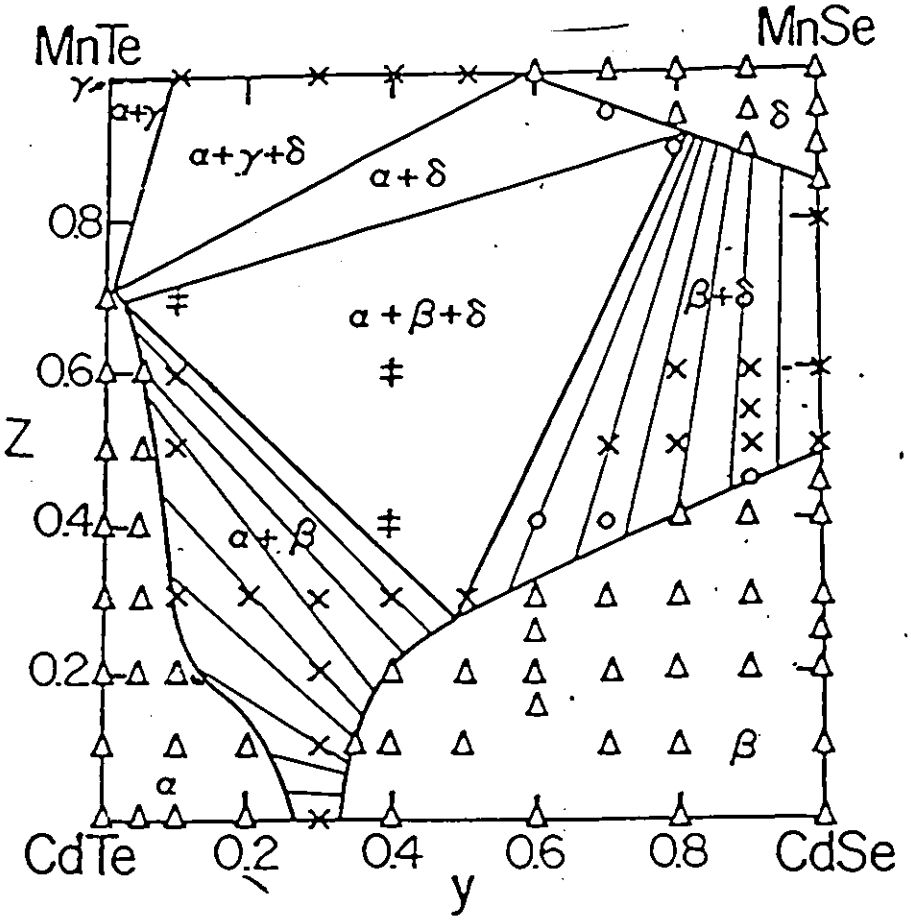

Fig. 2.6. Isothermal section at 960° C.

Δ single phase sample x sample observed to be two or three phase

o sample assumed to be two or three phase from lattice parameter curves.

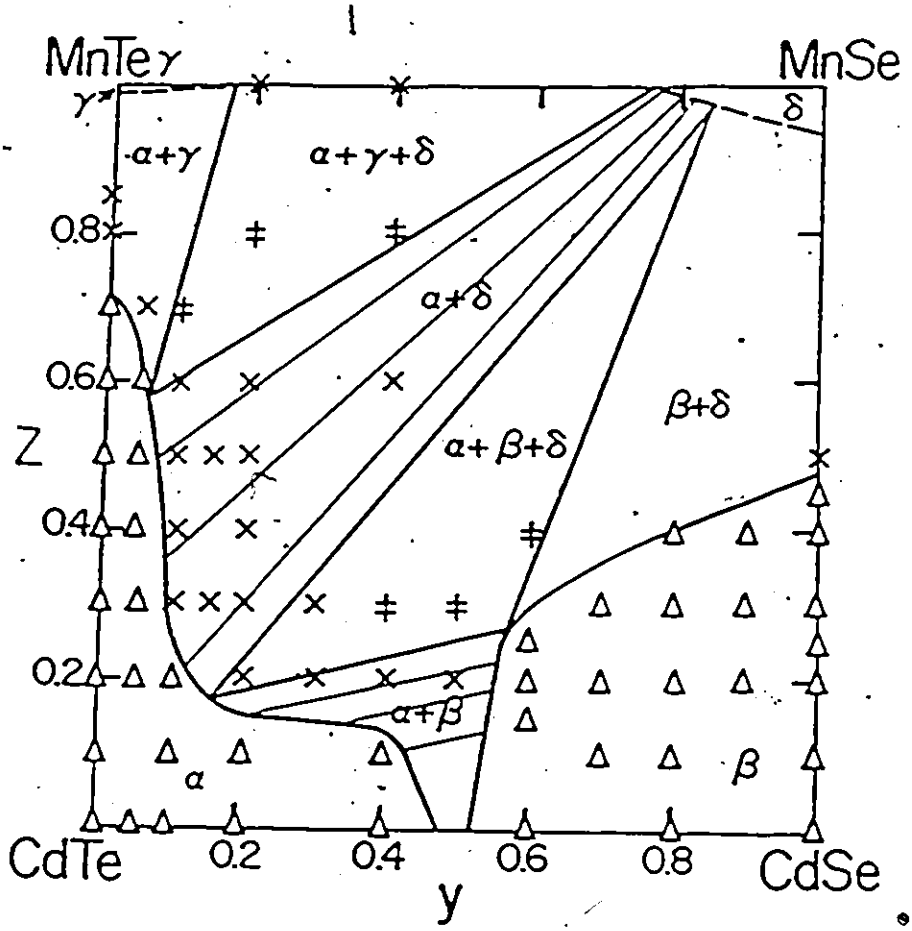

Fig. 2.7. Isothermal section at 600° C.

Δ single phase sample

‡ samples for which three phases were observed

x samples for which two phases were observed

form of the γ and δ fields in this case are approximated from previous work [2-5].

Turning to the values of the lattice parameters, it is usual in cases of this type to look for a convenient mathematical expression to represent the parameter as a function of the composition variables. This is convenient for purposes of interpolation etc. It was found that for each single-phase field the dependence of the lattice parameters on y and z could be expressed by a simple mathematical equation. Looking at Fig. 2.3, for instance, we saw that the experimental points on each line representing the variation in a with respect to z at constant y could be easily fitted to a straight line equation of the form: $a = n + mz$ where n and m respectively the intercept and the slope, were found to be y-dependent. All the values of n and m obtained for all the lines of constant y were then plotted as a function of y, these plots showed a linear dependence of m and n on y. The same kind of results were obtained from the data of Figs. 2.1, 2.2 and 2.4, so that the required mathematical equation would have the following form:

$$a = A + Bz + Cy + Dzy \qquad (2.3)$$

where A, B, C and D are constants. These constants could be obtained from a least square fit calculation which was carried out using an Apple II computer program (see Ref. (9)). In the zinc blende (α) region we have:

$$a(nm) = 0.6483 - 0.0145z - 0.0437y + 0.0141zy$$

with a standard deviation σ of 0.0003(nm). In the wurtzite (β) region we have:

$$a(nm) = 0.4595 - 0.0294z - 0.0297y + 0.0177zy$$

$$c(nm) = 0.7615 - 0.0867z - 0.0601y + 0.0639zy$$

with a standard deviation σ for a of 0.0002(nm) and for c of 0.0003 nm. In the NaCl (δ) region:

$$a(nm) = 0.4896 + 0.0958z + 0.0792y - 0.1216zy$$

with σ = 0.0004(nm). The small value of σ obtained in each case indicates that equation (2.3) is satisfactory for the present purpose.

2.5 Discussion and Conclusion

Two isothermal sections of the phase diagram of the semimagnetic semiconductor alloy system $(Cd_{1-z}Mn_z)(Te_{1-y}Se_y)$ were determined. In both sections, our system showed one-, two- and three-phase behaviour. However, in the investigation of the properties of semimagnetic semiconductors, only the single-phase fields are of interest, and the wider the range of single solution the better it is for the comparison of magnetic properties. The narrowness of the zinc blende field above z = 0.2 thus limited the range of investigation in that case and hence the selenium-rich β and δ phases were of greater interest for the magnetic work. The present results for $z < 0.2$ confirm the results of the CdTe - CdSe pseudo-binary alloy [1] that there is a considerable change with temperature in the range of the α and β phase fields. Thus around y = 0.4, it is possible to obtain single-phase samples with the same composition either in the zinc blende or the wurtzite structure depending on the annealing temperature. This is illustrated if we look at the sample $(Cd_{0.9}Mn_{0.1})(Te_{0.6}Se_{0.4})$. In the α-phase this sample has a lattice parameter of a = 6.302 Å. In the β-phase the lattice parameter are a = 4.454 Å and

c = 7.313 Å. A calculation of the spacing between nearest neighbors shows that it is the same in both structures, this is also true for next nearest neighbors spacing. These results are in agreement with the fact that the cubic zinc blende and hexagonal wurtzite structure are identical to the nearest and next nearest neighbors, but would differ beyond that.

References

1- Y. Steininger and A.J. Strauss, J. Cryst. Growth, 13-14 (1972) 657.

2- R.T. Delves and B. Lewis, J. Phys. Chem. Solids, 24 (1963) 549.

3- H. Wiedemeier and A.G. Sigai, J. Solid State Chem. 2 (1970) 406.

4- W.R. Cook Jr., J. Am. Ceram. Soc. 57 (1968) 518.

5- A.J. Panson and W.D. Johnson, J. Inorg. Nucl. Chem. 26 (1964) 701.

6- J.C. Woolley, in R.K. Willardson and H.L. Goering (eds), Compound semiconductors I, Reinhold, New York, 1962 p.3.

7- B.D. Cullity, elements of X-ray diffraction, Addison Wesley Publishing Company (1956) Chap. 11,12.

8- Peter Haasen, Physical metallurgy, Cambridge University press 1978, chap. 5.

9- "Science and Engineering Program Apple II", edited by John Heiborn, published by Osborne/McGraw-Hill.

Chapter 3

Magnetic Susceptibility Measurements

3.1 Introduction

The quantum mechanical theory of the atom tells us that the permanent magnetic moment of a free atom has two principal sources: the spin with which electrons are endowed; and their orbital angular momentum about the nucleus. However, atoms with filled electrons shells have zero spin, zero orbital moment and consequently zero magnetic moment. Only atoms with unfilled shells and unpaired spins possess a net magnetic moment, $\vec{\mu}$ given by [1]:

$$\vec{\mu} = -g\mu_B\vec{J} \qquad (3.1)$$

where g is the gyromagnetic ratio, μ_B is the Bohr magneton ($\mu_B = \frac{e\hbar}{2mc}$), $\vec{J}$ is the total angular momentum vector ($\vec{J} = \vec{L} + \vec{S}$). For example, the manganese atom which has a half filled 3d subshell with five unpaired electrons, possesses a net magnetic moment of $5\mu_B$, and consequently is said to be a magnetic atom.

When a solid is constituted of magnetic atoms or has some of these incorporated in it, it will consequently show certain magnetic behaviour, the nature of which depends on the way the magnetic moments interact with each other in the solid. One of the most effective ways to investigate the magnetic behaviour of a solid is the study of its response to an applied magnetic field; one aspect of this is known as the magnetic susceptibility χ. The magnetic susceptibility of a material is defined as the magnetic moment per unit volume M(the

magnetization) divided by the applied magnetic field H;

$$\chi = M/H. \tag{3.2}$$

In 1895 Curie showed that a certain class of substances had a positive and temperature dependent susceptibility given by

$$\chi = \frac{C}{T} \tag{3.3}$$

This is known as Curie's law and C is called Curie's constant. Substances that obey Curie's law, at least to a first approximation are usually called normal paramagnets. In a normal paramagnet the interaction between the magnetic dipoles is negligible and consequently always overcome by the disordering effect of the temperature which tends to randomize the magnetic dipoles orientations, so that the net magnetization vanishes as soon as the applied magnetic field is switched off. However, in other paramagnetic material, the dipole-dipole interaction is not negligible and as a result these materials obey a modified Curie's law, known as the Curie-Weiss law:

$$\chi = \frac{C}{T-\theta} \tag{3.4}$$

where θ is a constant which takes into account the effect of the inter-dipoles interaction and called the Curie-Weiss paramagnetic temperature. When this internal interaction tends to line up the magnetic moment parallel to each other, we have a ferromagnetic behaviour and the constant θ is positive. Such a material goes into an ordered state below a characteristic temperature T_c where all of its spins are aligned parallel to each other. The susceptibility goes to infinity at this temperature. When the internal interaction favors, an antiparallel orientations of neighbouring spins, we have antiferromagnetic behaviour and θ is negative in this case. The

magnetic susceptibility of an antiferromagnet increases, according to the Curie-Weiss law, when the temperature is decreased; however, the susceptibility shows a singularity in its curve at a critical temperature T_N, known as the Neel temperature, below which the spin system is in an ordered state of antiparallel alignment.

In the new class of magnetic materials known as spin-glass, the magnetic spins interact with each other in such a way that when the temperature is low enough for this interaction to overcome the thermal agitation, the spins freeze into a completely random configuration [3-6]. This is basically due to "frustration" of the spin system. This concept of "frustration" was first introduced by Toulouse [21-22]. It expresses the fundamental consequence that not all interactions can be satisfied simultaneously.

The magnetic susceptibility of a spin-glass material shows to some extent, similar behaviour to that of an antiferromagnet with a singularity occurring at the freezing temperature T_g [7-12]. Neutron diffraction [13-15] and Mössaber effect [16-18] experiments have confirmed the random freezing of the spins. According to these results it would seem that a magnetic phase transition occurs at this freezing temperature. However, in contrast to the magnetic propetties no discontinuity at T_g has been observed in the specific heat behaviour [19-20]. Knowing that such a discontinuity is an essential indication for a phase transition and that the freezing process takes place over a narrow range of temperatures rather than at a unique temperature [3-6], cast doubts on the occurrence of a phase transition in a spin-glass. So the question of whether there is in fact a phase transition has

still not been resolved although the evidence is clear that it is certainly not a simple type of phase transition.

What causes the spins to orient themselves parallel to each other in a ferromagnet or antiparallel in an antiferromagnet is the kind of internal interaction between the spins. This interaction is known from quantum mechanics, as the exchange interaction which is characterized by the so-called exchange integral, J_e; $E_{exch} = -J_e \vec{S}_i \vec{S}_j$. The exchange energy appears from the above equation as though there exists a direct coupling between the two spins (S_i and S_j). However, this interaction is fundamentally electrostatic and the spin enters into the expression of the energy as a consequence of the Pauli exclusion principle [1]. The sign of the exchange integral j_e, which depends on the distance between the interacting spins (see Fig. 3.1 for example), determines the kind of alignment of the spins. A positive J_e gives a ferromagnetic behaviour a negative J_e gives an antiferromagnetic behaviour. The randomness of the spins freezing in metallic spin-glass systems such as CuMn, AgMn, etc., is attributed to an oscillating J_e between positive and negative values as the distance between spins increases (fig. 3.2) [3]. This interaction known as the RKKY (Ruderman-Kittel-Kasuya-Yosida) interaction, results in a competition between ferromagnetic and antiferromagnetic interactions between the randomly distributed magnetic spins, which consequently become "frustrated" and freeze in a disordered fashion which minimizes the system energy.

The RKKY interaction arises from the large charge carrier concentration in metals [2,23]. However, stoichiometric semiconductors with wide energy gaps (which include the system under investigation)

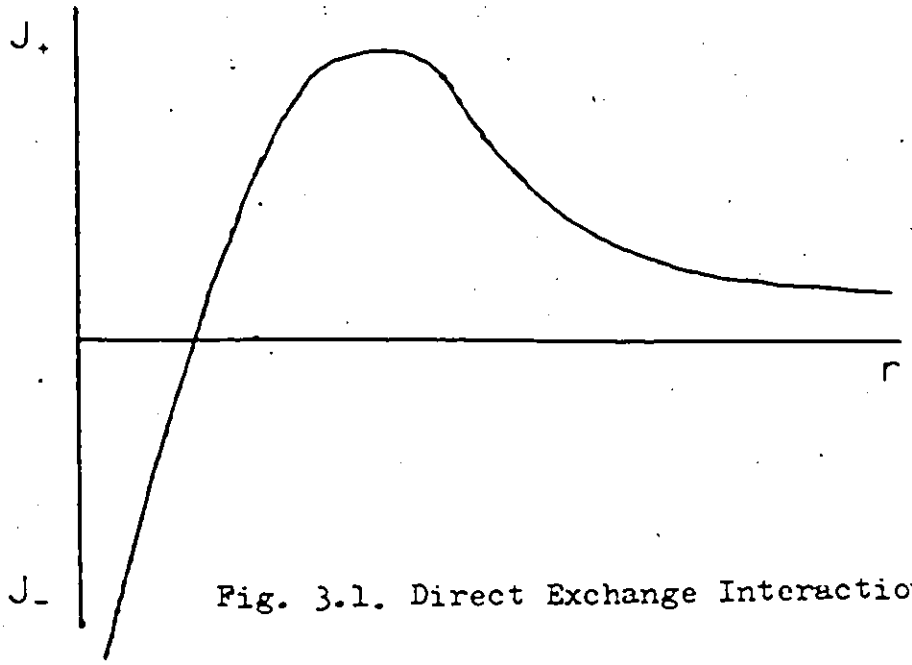

Fig. 3.1. Direct Exchange Interaction

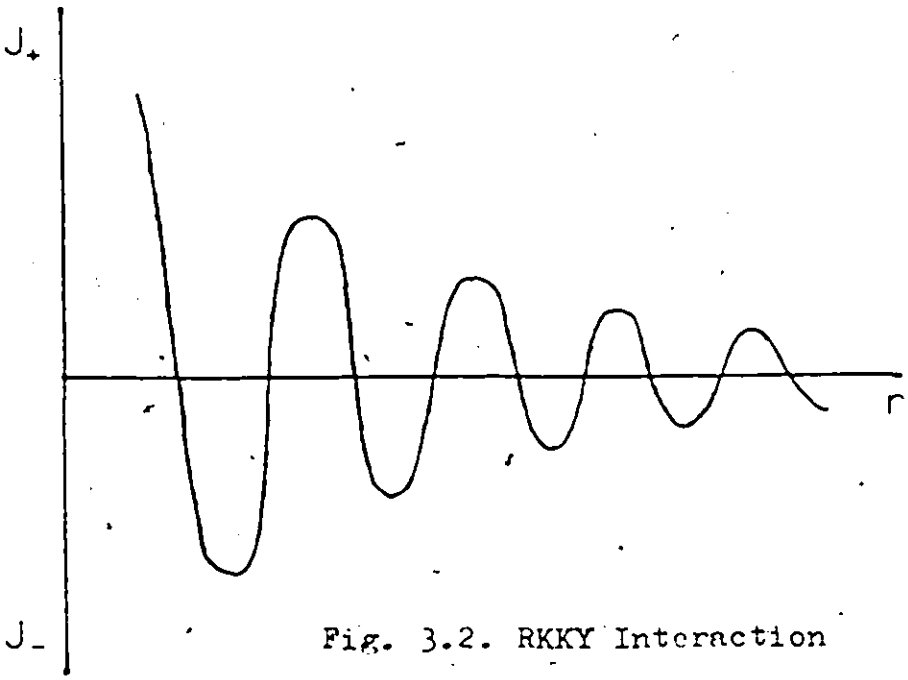

Fig. 3.2. RKKY Interaction

have low carrier concentration so that the RKKY interaction between spins can only give a negligible contribution in determining the spin-glass behaviour. It has been suggested by De Seze [24] and discussed by Villain [25] that a spin-glass behaviour could be obtained in insulator by using frustrated disordered systems with only antiferromagnetic interactions. Our alloy system $(Cd_{1-z}Mn_z)(Se_{1-y}Te_y)$ is a good example of an insulating spin-glass, where the Mn atoms randomly replace Cd atoms in a zinc blende lattice or in a wurtzite lattice (see chapter 2). A spin-glass regime with only AF interaction was predicted for a fcc lattice due to frustration [21,22]. A similar behaviour can be expected for a hcp arrangement.

A basic question about the nature of the antiferromagnetic coupling between a pair of Mn ions is still not fully resolved. Some theoretical work suggested that the indirect exchange interaction between two localized moments; which arises from the virtual transitions between the filled valence band and the empty conduction band in insulators (Bloembergen - Rowland mechanism [28]), is a possible mechanism [26,27]. However, there has been no experimental evidence which supports this theory in our case. To explain the magnetic properties of rare earth compounds, Goncalves et al [51] proposed an Anderson-type superexchange the theory of which they had developed. Geertsma et al [50] extended this theory to include the transition metals compounds. This will be discussed later in some detail.

One of the main objects of our investigation of the magnetic susceptibility is to try and identify the right exchange mechanism

which is taking place in our alloys and consequently in all similar wide gap semimagnetic semiconductors.

3.2 Experimental Procedures:

The d.c. magnetic susceptibility of a sample is obtained by measuring the magnetization induced in the sample by an applied steady magnetic field. An rf biased SQUID magnetometer was used for this purpose. The word SQUID is an acronym for Superconducting Quantum Interference Device. This instrument is capable of sensing very small magnetic fluxes ($\sim 10^{-11}$ gauss. cm^2) with an extremely high degree of accuracy [29-31]. Consequently a small amount of samples ($\sim$ 20 mg) and a small applied magnetic field ($\sim$ 30 gauss) only are needed.

Conceptually, the magnetic flux sensor of such magnetometer, consists of a pair of astrotically wound superconducting pickup coils which are part of a continuous superconducting transformer circuit coupled to a superconducting ring with a single weak-link which in turn is coupled inductively to an rf resonant circuit. The superconducting ring-resonant circuit arrangement is commonly called an rf-SQUID. When the sample is inserted into one of the pickup coils, the change in magnetic flux is transmitted to the SQUID producing a change in the magnetometer output proportional to the sample's magnetization.

An actual susceptometer system must, of course, be considerably more complex. Fig. 3.3 shows a schematic representation of the system we used. This system was designed and developed by Dr. Gilles Lamarche and was constructed in the Physics department work shop. The cryostat is a typical double, dewer system with liquid

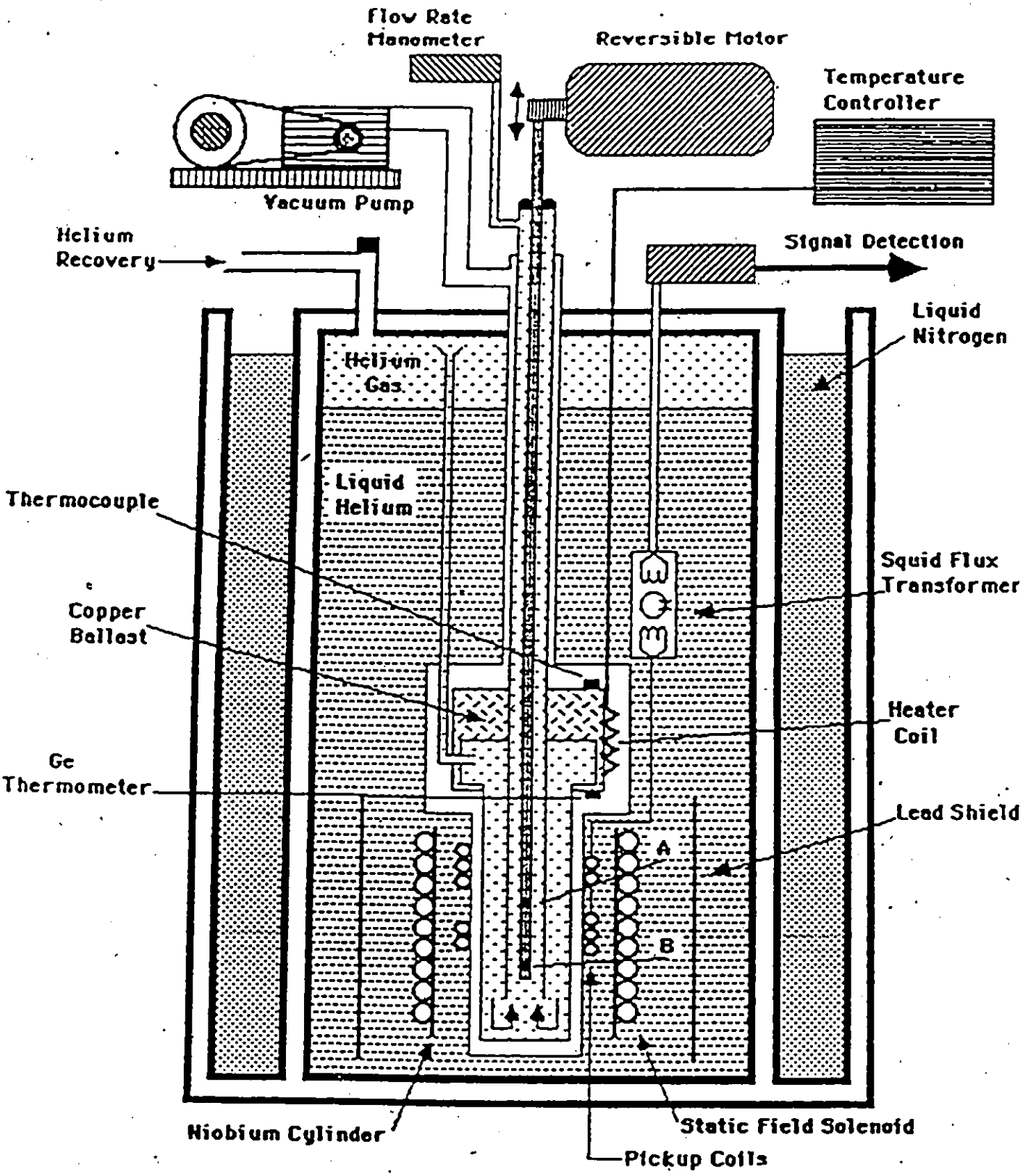

Fig. 3.3. Magnetic Susceptibility Apparatus. A sample is placed in position B. A second sample or a paramagnetic salt is placed in position A.

helium in the inner dewer and liquid nitrogen in the outer. A lead shield inside the helium bath surrounded the inner part of the system and so reduced any penetration from external stray field. A solenoid and a niobium cylinder were placed inside this shield in the helium bath. The solenoid provided a magnetic field which was trapped by the superconducting niobium when liquid helium was transferred into the dewer. A field ranging between 25 to 30 gauss was applied through the solenoid. The niobium cylinder also provided additional magnetic shielding.

A S.H.E. model 330 SQUID was used. The SC pickup coils are located inside the niobium cylinder and are rigidly affixed to the outside wall of a vacuum can inside of which an exchange helium gas chamber is placed. This gas chamber contains the sample holder which consists of a very pure copper container attached to a long plastic rod which extends outside the cryostat and is attached to a reversible motor. This enabled different samples to be inserted and extracted without opening the whole system as well as provided a means for driving the sample through the pickup coils.

What we could measure with this system is the SQUID voltage from which the absolute susceptibility could determined through the use of the following calibration relation:

$$\chi = \frac{(1.25 \times 10^{-5})\ V}{(\frac{i}{2} + 0.23)\ M}\ \text{emu/gm}$$

where V is the SQUID voltage, M the mass of the sample in gram and i the current through the solenoid in mA.

The temperature of the system was controlled by circulating helium gas around the sample. The gas from over the helium bath could

enter the gas chamber through a tube which was wrapped several times around a copper ballast attached to the outside wall of the top part of the gas chamber. The copper ballast was heated so in turn it heated up the He gas as the latter was going through. This system allowed us to control the temperature in the range between 4.2 K and 275 K. Three different thermometers placed at different locations were used to monitor the temperature. A chromel gold 7% iron thermocouple was positioned at the top of the copper block. A calibrated Ge resistance thermometer was placed near the bottom of the block. Finally a magnetic thermometer (a paramagnetic salt) was placed on the sample holder about 10 cm above the sample. Thus the magnetic susceptibility could be determined as a function of temperature.

3.3 Results:

The magnetic susceptibility measurements were carried out for all the single-phase samples in the wurtzite and zinc blende regions. These measurements were made as a function of temperature to determine values for spin-glass transition temperature T_g, the Curie-Weiss paramagnetic temperature θ and the Curie constant C for the alloys.

For zero-field-cooled samples with $z > 0.25$, the values of the magnetic susceptibility χ as a function of temperature T showed a well defined cusp at a temperature T_g. This is illustrated in Fig. 3.4a where values of $1/\chi$ are plotted as a function of T for a sample with $z = 0.4$, $y = 0.9$. For $z < 0.25$ any such cusp occurs at or below 4.2 K, and so could not be observed with the present equipment. The values of T_g obtained are plotted in Fig. 3.5 as a function of z for

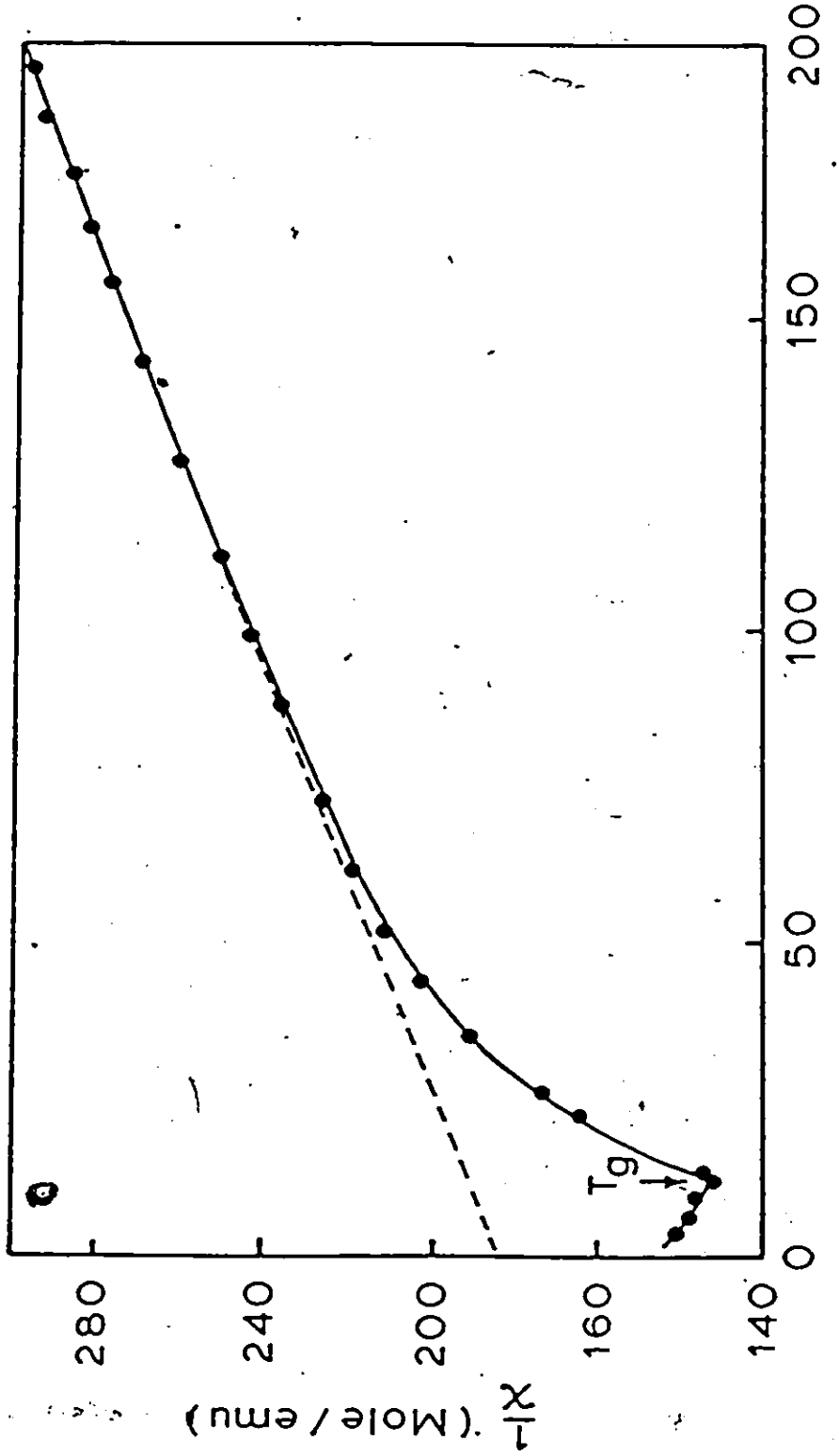

Fig. 3.4a. A typical curve showing the variation of the reciprocal magnetic susceptibility $1/\chi$ versus temperature (χ is measured in emu per mole of sample). The curve shown is for the sample with, $z = 0.40$, $y = 0.90$. T_g is the spin-glass transition temperature.

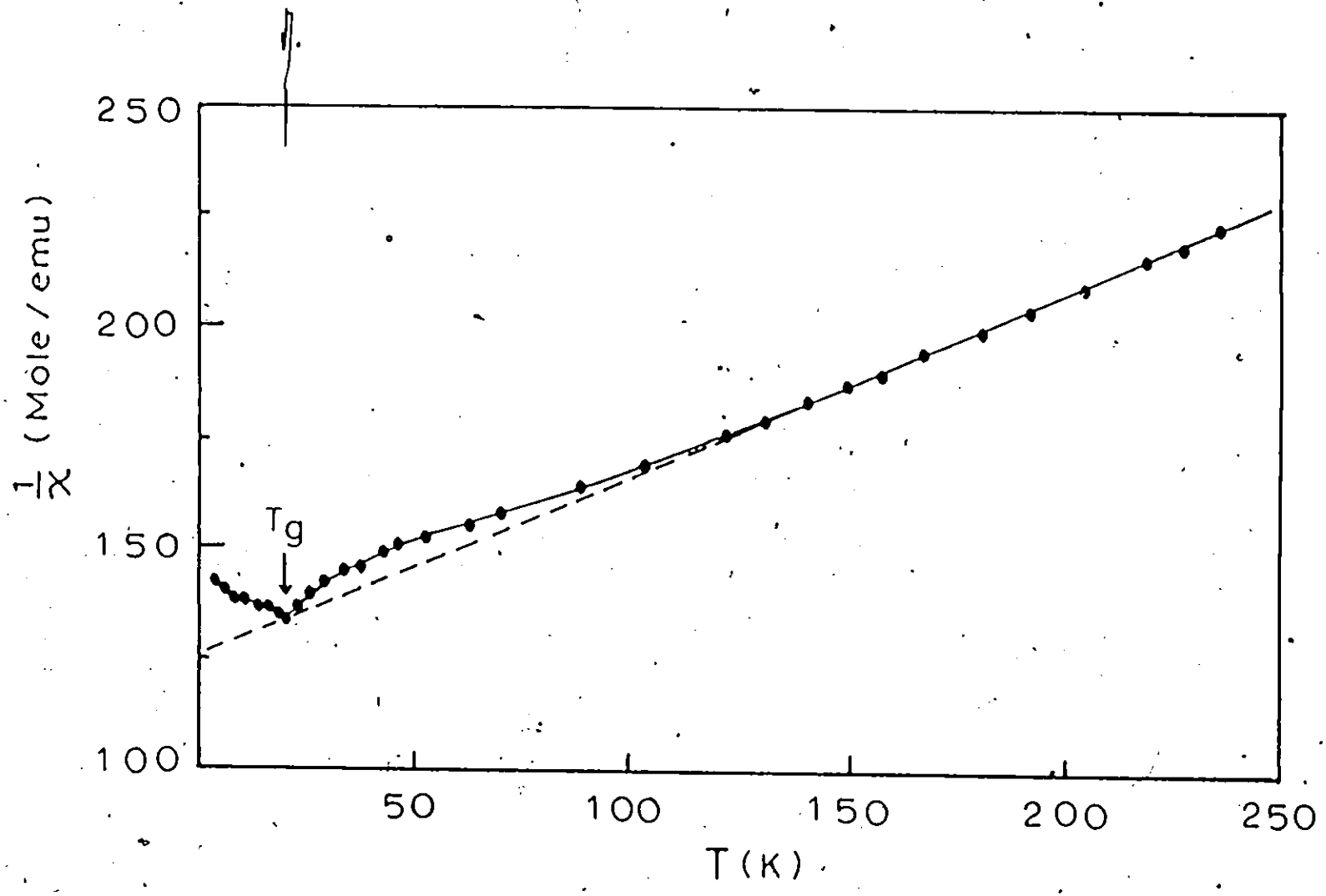

Fig. 3.4b. Varition of the reciprocal magnetic susceptibility with temperature for the sample with z = 0.50, y = 0.05. This curve is typical for all samples with z ≥ 0.50.

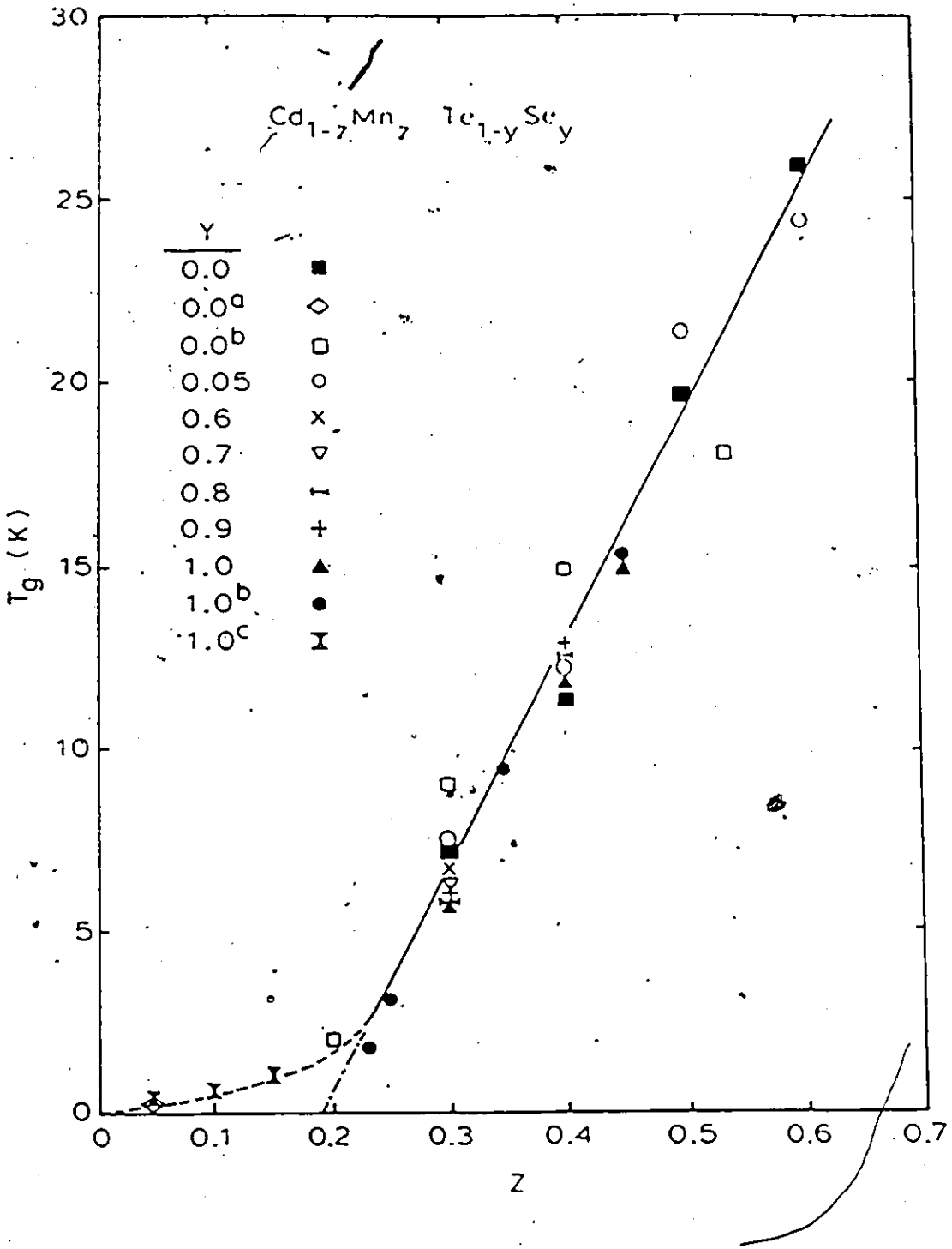

Fig. 3.5. Plot showing the spin-glass transition temperature T_g, measured by magnetic susceptibility, versus the Mn concentration z for alloys in the cubic zinc blende α phase and the hexagonal wurtzite β phase fields. [a]Ref. 44 , [b]Ref. 32 , [c]Ref. 45 .

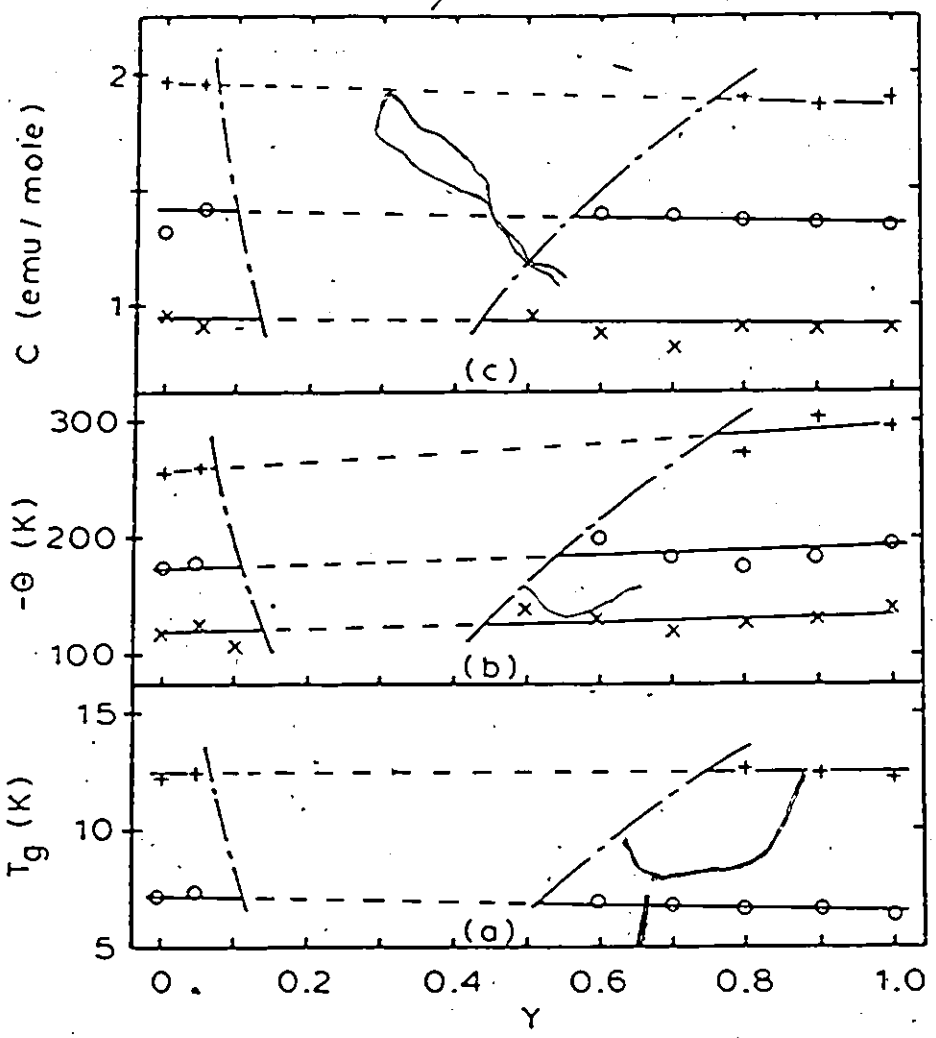

Fig. 3.6. Plots of the parameters T_g, θ and C obtained from susceptibility measurements versus the fraction y of Se atoms for various concentrations z of Mn. (a) gives the spin-glass transition temperature T_g, (b) gives the Curie-Weiss temperature θ, and (c) gives the Curie constant C. (C is measured in emu per mole of sample). The dot-dashed lines indicate the boundaries of the single phase fields. The symbols representing the z values are (x) = 0.2, (O) = 0.3 and (+) = 0.4.

various y values and in Fig. 3.6(a) as a function of y for various z, in both the zinc blende α and wurtzite β fields. Also shown in Fig. 3.5 are the values of T_g given by Oseroff [32] for the $Cd_{1-z}Mn_zTe$ and $Cd_{1-z}Mn_zSe$ alloys. It is seen that the values of T_g are relatively insensitive to the value of y so that within the limits of experimental error the variation of T_g with y at constant z for a given phase field is too small to be determined with any accuracy. Therefore in Fig. 3.5 only a mean line of T_g vs z is shown. This graph of T_g vs z appears to be linear within the limits of experimental error and to extrapolate to $T_g = 0$ at $z = 0.2$.

It is seen from Fig. 3.4 that for values of T well above T_g the $1/\chi$ vs T results have the linear Curie-Weiss form and can be extrapolated to give a Curie-Weiss temperature θ. Values of θ so obtained are shown in Fig. 3.6(b) and 3.7 together in Fig. 3.7 with the values given by Oseroff [32] for the $Cd_{1-z}Mn_zTe$ and $Cd_{1-z}Mn_zSe$ alloys.

As is seen from Fig. 3.6(b) the variation of θ with y is only a little larger than the experimental scatter and so in Fig. 3.7 the various values for y are not distinguished. The lines drawn in Fig. 3.7 indicate approximatively the values of θ for the $y = 1$ edge (selenide) and for $y = 0$ edge (Telluride). The values for the quaternary alloys should lie in the area between the two lines. The dot-dashed lines show the limits of single-phase behaviour.

The slope of the linear part of the $1/\chi$ vs T graph gives the values of the Curie constant C. The values of C (emu per mole of sample) so obtained are shown plotted as a function of the composition parameters in Fig. 3.6(c) and 3.8. At temperatures nearer to T_g, the

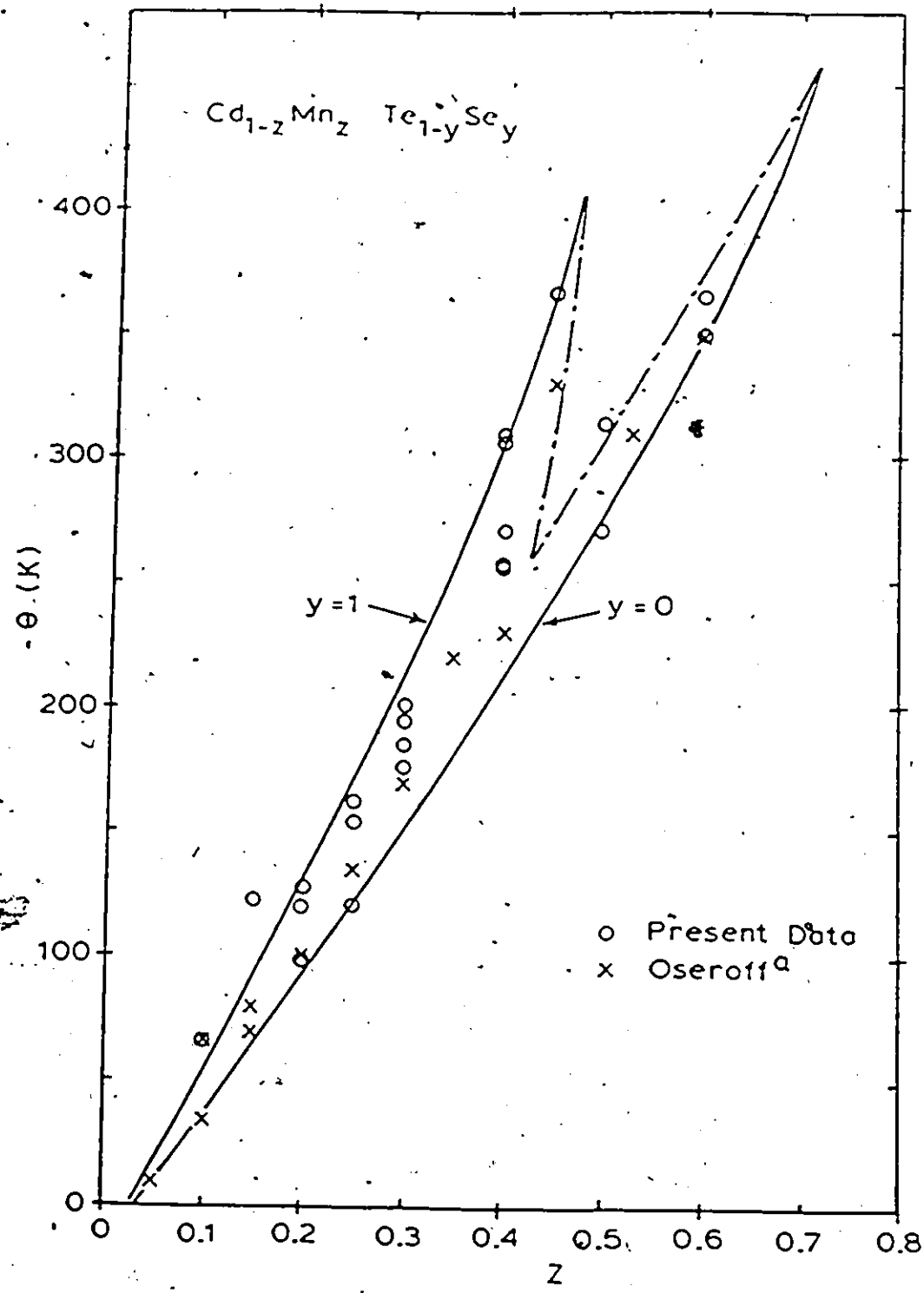

Fig. 3.7. Plot of the Curie-Weiss temperature θ versus the Mn concentration z. The points representing the present data are obtained over the whole range of the α and β single phase fields. The dot-dashed lines show the boundaries of the single phase fields. [a]Ref. 32 .

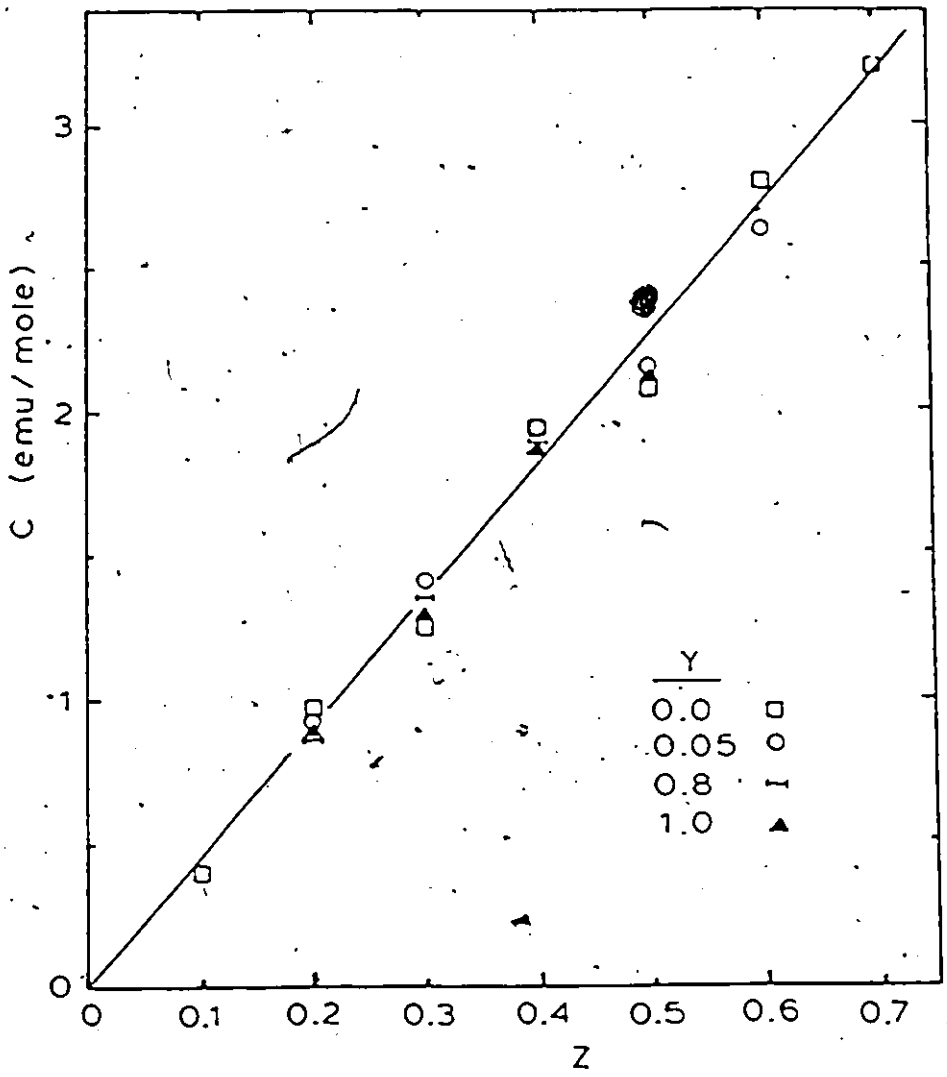

Fig. 3.8. Plot of the Curie constant C versus the Mn concentration z for various alloy compositions covering the α and β single phase fields. (C is measured in emu per mole of sample).

$1/\chi$ vs T curve shows a downturn deviation from the linear Curie-Weiss behaviour, as shown in Fig. 3.4a showing a strongly enhanced paramagnetism. This behaviour is typical for all samples with $z < 0.5$. However samples with $z > 0.5$ shows an upward deviation from the Curie-Weiss line indicating a decrease in their magnetic susceptibility. An example is given in Fig. 3.4b for a sample with $z = 0.5$, $y = 0.05$. These downward and upward deviations from the Curie-Weiss line will be discussed later.

3.4 Analysis and Discussion:

The results of the variation of the inverse susceptibility with temperature (Fig 3.4) are consistent with the behaviour of spin-glass material [3,4,33,40]. At high temperatures the Mn^{2+} spins interact weekly in a normal paramagnet fashion, giving the Curie-Weiss behaviour for the magnetic susceptibility, manifested by a linear variation of the $1/\chi$ vs T curve. The extrapolation of this linear portion intersects the negative T axis, implying that an antiferromagnetic interaction is taking place between the spins so in this high temperature region the susceptibility:

$$\chi(T)_{\text{per mole}} = \frac{zN_A\mu_B^2 g^2 S(S+1)}{3k(T-\theta)} \qquad (3.4)$$

where N_A is the Avogadvo number, z the Mn concentration and $\theta < 0$. As the temperature is lowered the spins begin to show greater correlation i.e. tend to stay antiferromagnetically aligned in small clusters for longer time intervals. As the temperature continue to fall the range of the interaction extend and the Mn clusters show greater correlation. The formation of these finite spin clusters and the growing interaction

between the spins in them, cause a superparamagnetic effect to come into play so that χ is increased and hence $1/\chi$ changes slope and falls below the Curie-Weiss line (Fig. 3.4a). The concept of superparamagnetism (or enhanced paramagnetism) was first intorduced by Neel (1955) [3,4] to explain some unusual effects seen in magnetic rocks. Similar effects has been observed in these class of materials exhibiting spin-glass or cluster-glass behaviour. This superparamagnetic effect here is believed to be due to the presence of uncompensated spins at the surface of finite independent clusters; not to forget the presence of isolated spins also which give a paramagnetic contribution.

According to Brandt et al [35] the susceptibility in this temperature region follows the Curie's law:

$\chi(T)_{\text{per mole}} = z\alpha N_A \frac{\mu_B^2 g^2 S(S+1)}{3kT}$ where here the factor α $(0 < \alpha < 1)$ is introduced so that αNa represents the effective number of magnetic ions with spin S, and that is because the effective number of free spins had been reduced through the antiferromagnetic coupling and hence the spins correlation in the clusters. As we mentioned before, this downward deviation from the Curie-Weiss line in the $1/\chi$ vs T results occurs for samples with Mn concentration $z < 0.5$. However for $z > 0.5$ an upward deviation occurs instead, indicating a decrease in χ, (Fig. 3.4b). This can be interpreted as follow: when the Mn concentration is high $(z > 0.5)$ large Mn clusters are most likely to form, so that the surface to volume ratio for these large clusters is small; consequently the number of uncompensated spins will be reduced relative to small sized clusters (for $z < 0.5$), so will be the probability of finding

isolated free spins. All that contribute to a diminishing of the superparamagnetic effect, which will be swamped by the effect of longer correlation time i.e. the spins in the big sized clusters tend to stay antiferromagnetically aligned for longer periods of time and over a range of temperatures, causing the decrease of χ below the Curie-Weiss behaviour and hence the upward deviation in the $1/\chi$ curve.

As the temperature is further lowered, the correlation range extends to include farther and originally independent spins; as a result the size of the magnetic clusters increases until they begin making contact with each other, i.e. they become strongly interacting. Finally, when the system reach a certain characteristic temperature T_g a percolation takes place which generates an infinite cluster of frozen spins. The spins inside the infinite cluster are strongly correlated, and have their directions governed by a uniaxial anisotropy field which is assumed to be randomly distributed over all directions. Thus the spins are no longer able to react to the external field since they are embedded in the infinite cluster; this causes the magnetic susceptibility χ to show a cusp maximum at T_g (which corresponds to the minimum in $1/\chi$ vs T curve in Fig. 3.4). It is this freezing process which made Oseroff describe this class of materials as cluster-glass [36] rather than spin-glass.

Escorne et al [37] have shown that for this class of materials, at $T \leq T_g$ there are still some free small clusters or isolated spins which are not part of the infinite cluster and which behave in a paramagnetic manner. However at $T << T_g$ more and more of those free clusters or spins will join the infinite cluster, thereby

producing a uniformly distributed collection of frozen spins.

It is worth noting that for $T < T_g$, χ shows a thermal hysteresis and the results depend on whether the sample was zero-field-cooled or field cooled. This behaviour was also observed by Oseroff et al. [32,36] and Nagata et al [38,39] for insulating spin-glasses and is similar to that of the metallic spin-glasses CuMn [33] and AuFe [40].

Considering now the variation of the parameters obtained from magnetic susceptibility measurements. As indicated above T_g varies very little with y at constant z, and for $z > 0.2$ appears to show a linear variation with z (Fig 3.5). This graph of T_g vs z extrapolated to zero T_g at $z \sim 0.2$, which is very close to the value of 0.195 calculated for the percolation limit for nearest neighbour interaction for an fcc lattice [41,46]. For an hcp a value of 0.204 has been reported [43]. The behaviour of T_g has been previously explained by postulating that spin-glass behaviour cannot occur for concentration less than this percolation limit. However results by Novak et al [44,45] have shown that values of T_g can be obtained at concentration down to $x = 0.05$. To discuss this point further, we saw that it was convenient to use the relation suggested by Escorne et al [46].

It is is assumed that the exchange parameter J between two Mn ions varies as

$$J = J_o \exp(-\alpha r) \qquad (3.5)$$

where r is the distance between the ions; then for a concentration z of Mn ions arranged at random on a cation sublattice of spacing d, the mean Mn^{2+} spacing can be written as $dz^{-1/3}$, so that the mean exchange interaction between the Mn ions can be taken as $J_m = J_o \exp(-\alpha\, dz^{-1/3})$.

If also it is assumed that $kT_g = -AJ_m$ where A is a positive constant independent of z then this gives:

$$\ell nTg = \ell n\left(\frac{-AJ_o}{k}\right) - \alpha\, dz^{-1/3} \qquad (3.6)$$

d is related to the lattice parameter, and for cubic zinc blende $d = a_c/\sqrt{2}$ while for hexagonal wurtzite $d = a_h$. A plot of ℓnT_g vs $dz^{-1/3}$ should give a straight line if the assumption concerning the exchange integral is valid.

The results for ℓnT_g vs $dz^{-1/3}$ have already been given for the $Cd_xZn_yMn_zTe$ alloys by Donofrio et al [47] and it was shown that for $z < 0.6$ a good straight line was obtained not only for the points with $z > 0.2$ but also for the point with a small value of z given by Novak et al [44,45]. It thus appears that the equation of Escorne et al is valid down to a very small value of z. Fig. 3.9 shows a plot of ℓnT_g vs $dz^{-1/3}$ for all samples investigated here, both cubic and hexagonal, and includes the the values of $Cd_{1-z}Mn_zTe$ given previously [47] and values for the low concentration alloys of Novak et al [44,45]. These results indicate that, within the limits of experimental error and for a given structure, the exponent α is constant and independent of composition, namely of the Mn concentration z.

Turning once more to the variation of T_g with z, it is seen that for $z > 0.2$, within the limits of experimental error, both the ℓnT_g vs $dz^{-1/3}$ (Fig. 3.9) and the T_g vs z (Fig. 3.5) plots appear to give a linear behaviour. However for $z < 0.2$, if the ℓnT_g vs $dz^{-1/3}$ result is followed, the variation of T_g with z deviates from linear behaviour as shown by the dotted curve in Fig. 3.5. The extrapolation of the linear region to the nearest neighbour percolation limit is

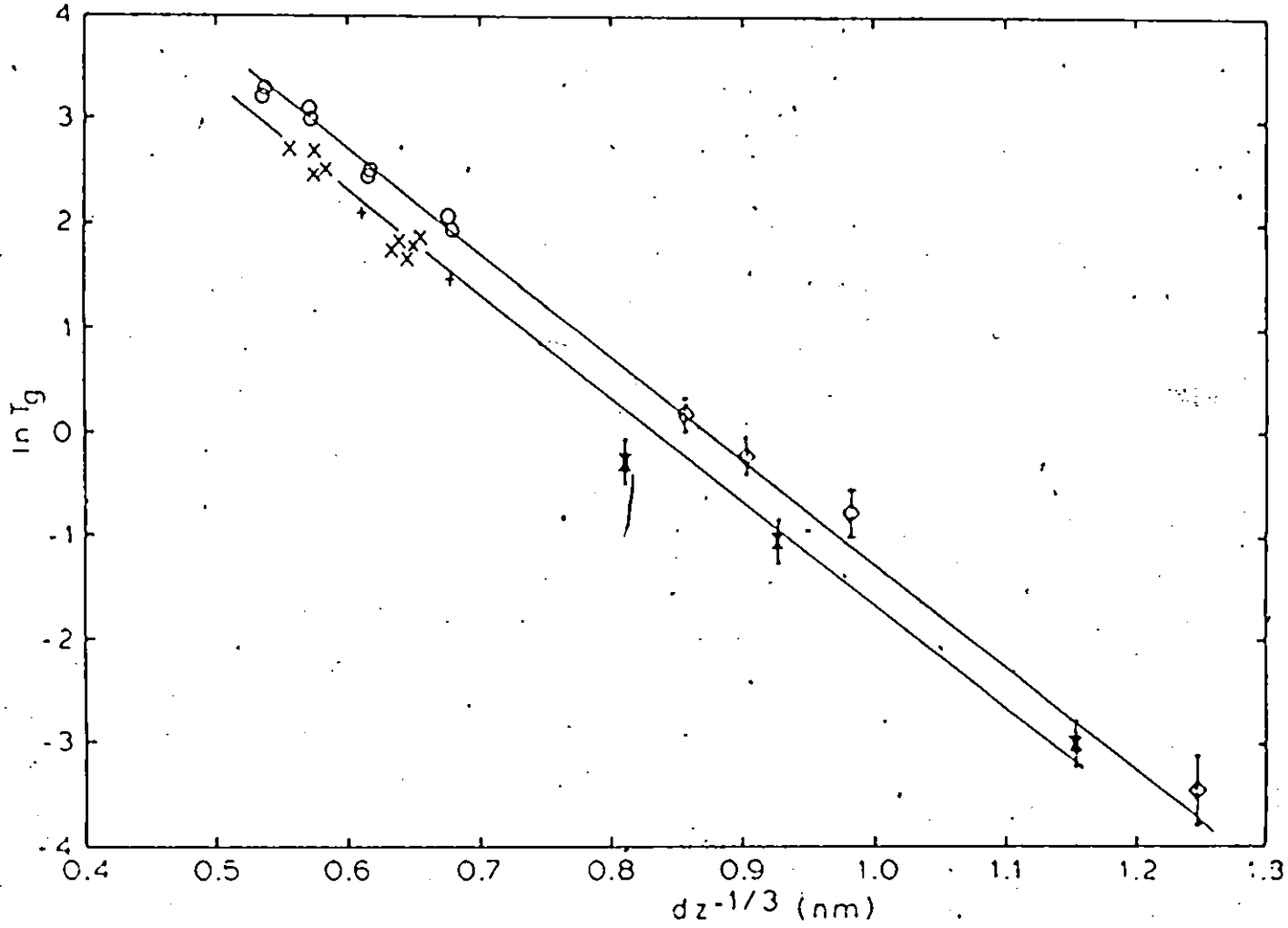

Fig. 3.9. Variation of ln T_g vs $dz^{-1/3}$ for $Cd_{1-z}Mn_z Te_{1-y}Se_y$.

a) Zinc blende structure o Present work ◇ Ref. 44

b) Wurtzite structure × Present work + Ref. 32

⧗ Ref. 45

explained by the fact that for $z > 0.2$ nearest neighbour effects dominate in the exchange process. However as z is reduced, the number of nearest neighbours correspondingly falls so that the next nearest neighbour and next next nearest neighbour effects expected from the equation of Escorne et al, begin to have noticeable effect. As shown by Domb and Dalton [41], the percolation limit for nearest neighbours is 0.195 for next nearest neighbours 0.136 and for the next next nearest neighbours 0.061. On this basis the T_g vs z variation shown by the dotted line is to be expected.

As we mentioned above, the result of $\ln T_g$ vs $dz^{-1/3}$ in Fig. 3.9 showed a linear variation implying that the exponent α is a constant independent of z and y. Consequently α is independent of the energy gap E_g which varies substantially with composition (see chapter 5 for details). Thus Escorne's equation indicates that there is a long range indirect antiferromagnetic exchange interaction between the Mn^{2+} ions which has an exponential variation with distance and for which the exponent α is independent of composition and hence various other parameters which are composition dependent.

Turning to the exchange mechanisms which have been proposed to explain spin-glass behaviour, clearly in this case the direct exchange is excluded from the considerations because of large distances between Mn ions (even in the case of nearest Mn neighbours there is an intervening anion situated between Mn ions). The RKKY is also eliminated because of the low charge carrier concentration in these materials. With regard to superexchange through anion p orbitals, in the present material, the tellenium and/or selenium p electrons are

part of the sp^3 hybridized valence-conduction band system, and so superexchange involving various interactions with valence and conduction band states as discussed by various authors [26,28,49-51,53] needs to be considered. One mechanism proposed by Bloembergen and Rowland [28] and discussed by various authors [26, 48] involves virtual transitions between valence and conduction bands. However, although this exchange has an exponential variation with distance $\{J(r) \alpha \exp(-\frac{2mE_g}{\hbar^2})^{\frac{1}{2}} r\}$, the exponent is a function of the band gap E_g. Thus, although this mechanism is important in low band gap materials e.g. $Hg_{1-z}Mn_zTe$ [26], it cannot be the dominant mechanism in the present case since E_g is of the order of 2eV in our materials.

Another mechanism is that proposed by Geertsma et al [50] based on the work of Goncalves da Silva and Falicov [51]. This give exchange interaction through virtual transitions between the valence band and a delocalized band of 3d states. The exponential term in this case has an exponent which is a function of the energy difference between the two states and the effective mass of the valence band. Since for the zinc blende and wurtzite semiconductors, the valence band is insensitive to changes in composition, it appears reasonable that this exponent should have a constant value as described above. Thus this exchange would appear to have the form required to explain the present results. This conclusion is consistent with recent results of Larson et al [49] who have given a general analysis of these interactions and show for $Cd_{1-z}Mn_zTe$ alloys that superexchange via the valence band, which is essentially what the work of Geertsma et al considers, is very much more important than the Bloembergen-Rowland

exchange involving the conduction band.

In the analysis of Geertsma et al [50] it has been shown that to a good approximation the exchange can be taken to have the form:

$$J(r) = I_o r^{-2} \exp(-\alpha r) \qquad (3.7)$$

i.e. there is an additional r^{-2} factor compared with Escorne's equation (equ. 3.5). When this term is included in the present analysis equation (3.6) must be replaced by

$$\ell n\, d^2\, T_g\, z^{-2/3} = \ell n\left(\frac{-AI_o}{k}\right) - \alpha d z^{-1/3} \qquad (3.8)$$

In Fig. 3.10 the data for our system $[Cd_{1-z}Mn_z][Te_{1-y}Se_y]$ are plotted as $\ell n\, d^2\, T_g\, z^{-2/3}$ vs $dz^{-1/3}$ together with those for the two system $Cd_xZn_yMn_zTe$ and $Cd_xZn_yMn_zSe$ investigated respectively by T. Donofrio and M. Manhas [47,52] members of our research group. In Fig. 3.11, the data for our system are plotted also as $\ell n\, d^2 T_g\, z^{-2/3}$ vs $dz^{-1/3}$ but in this case the data of Novak et al [44,45] (low Mn concentration) are included. It is seen from the two figures, that in this case also within the limits of experimental error the results lie on two straight lines, one for the cubic zinc blende and one for the hexagonal wurtzite structure. Both types of plot (Fig. 3.9 and Figs. 3.10, 3.11) appear to be straight lines because the variation of d is relatively small and so has little effect on the shape of the graph.

From the slope and the intercept of each of the lines in Figs. 3.10, 3.11 values of α and AI_o/k can be determined for each structure.

These are: Zinc blende $\alpha = 6.1\pm0.4\ nm^{-1}$ $\quad \frac{AI_o}{k} = -(2.03\pm0.5)\times10^2\ Knm^2$

Wurtzite $\quad \alpha = 8.0\pm0.4\ nm^{-1}$ $\quad \frac{AI_o}{k} = -(4.35\pm0.9)\times10^2\ Knm^2$

As indicated by Anderson [53], the parameter A can be equated

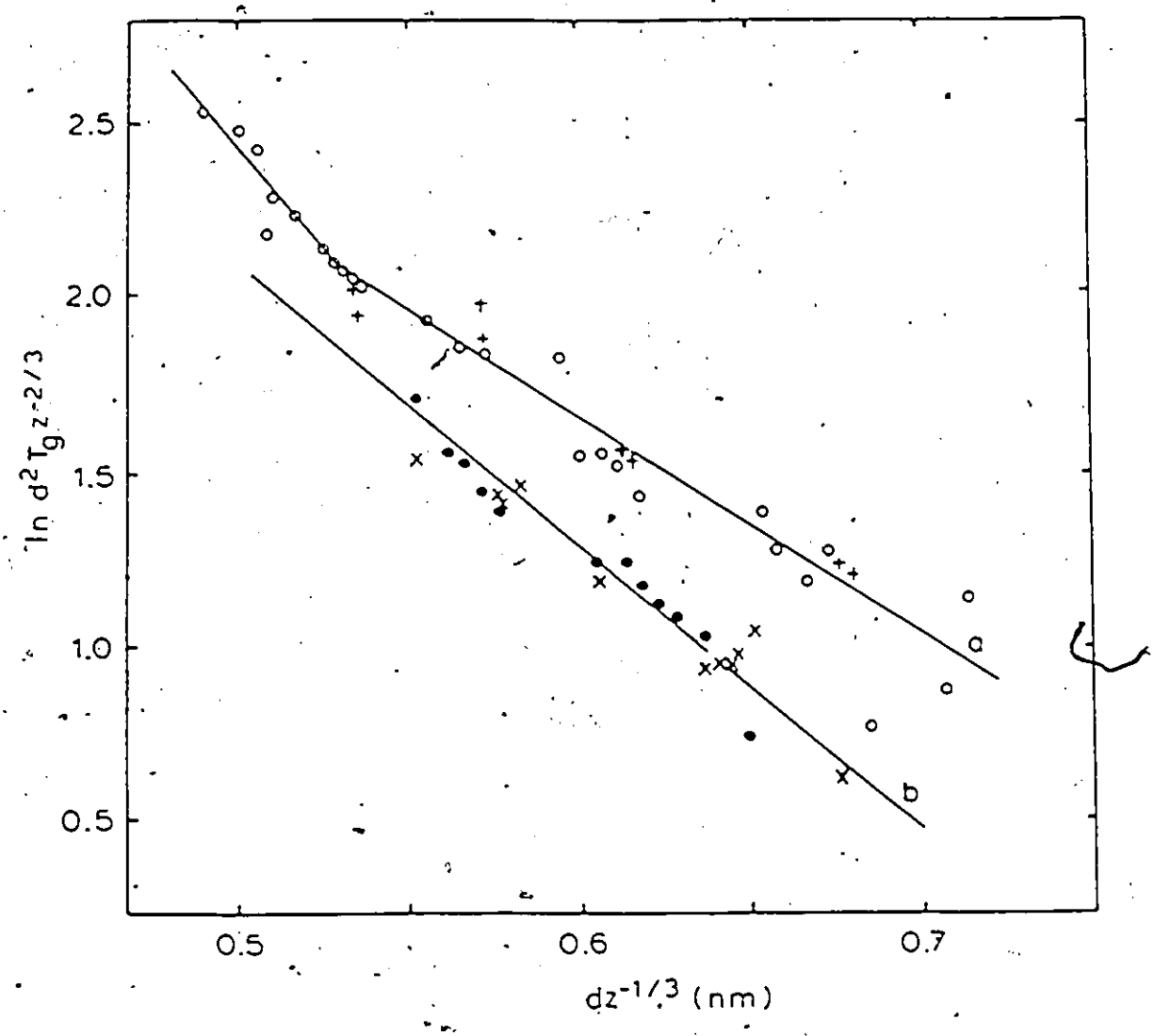

Fig. 3.10. Variation of $\ln dT_g z^{-2/3}$ vs $dz^{-1/3}$

a) Zinc blende structure ○ $Cd_xZn_yMn_zTe$ + $Cd_{1-z}Mn_zTe_{1-y}Se_y$

b) Wurtzite structure ● $Cd_xZn_yMn_zSe$ × $Cd_{1-z}Mn_zTe_{1-y}Se_y$

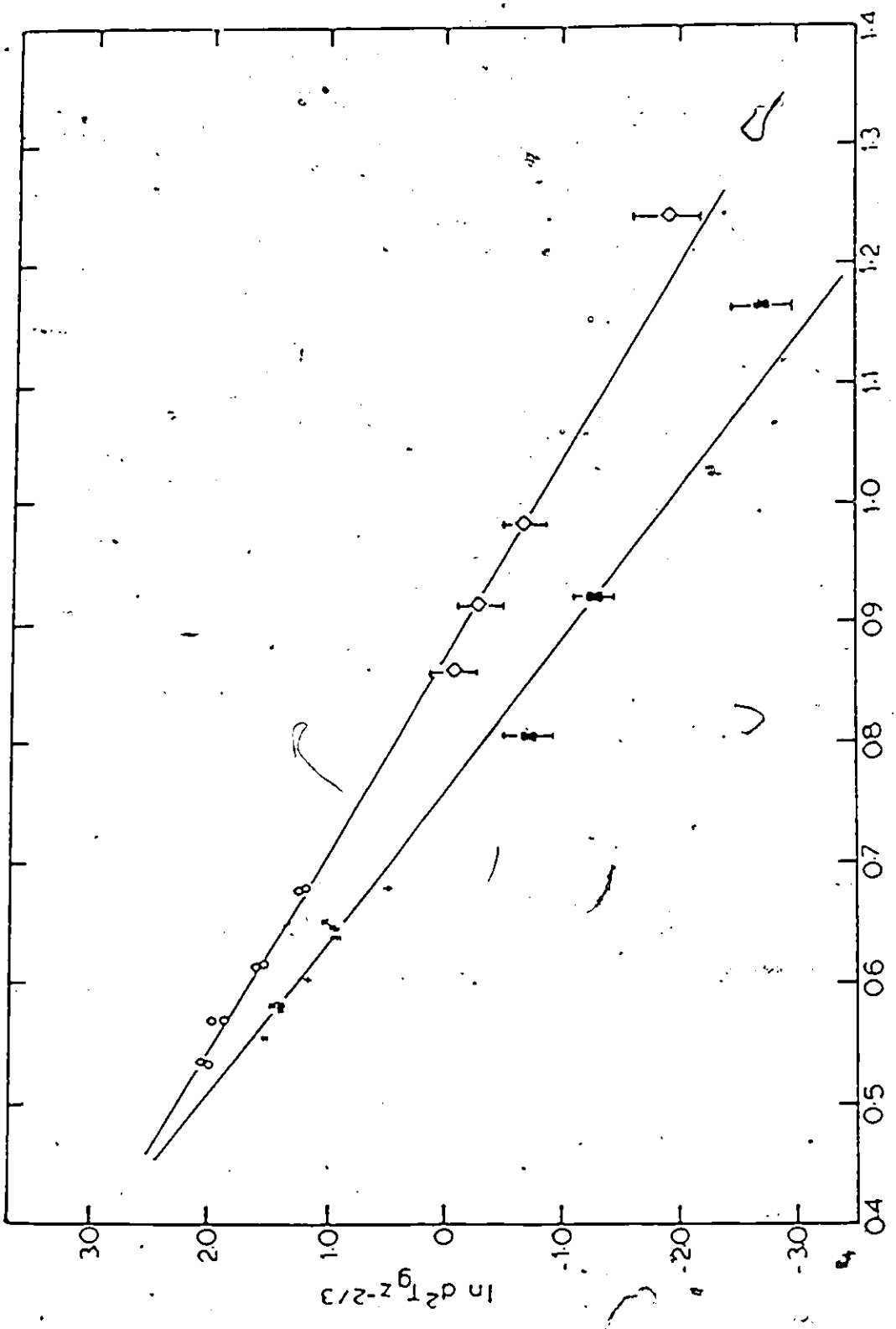

Fig. 3.11. Variation of $\ln d^2T_g z^{-2/3}$ vs $dz^{-1/3}$ for $Cd_{1-z}Mn_z Te_{1-y}Se_y$,

a) Zinc blende structure o Present work Ref. 44

b) Wurtzite structure x Present work + Ref. 32

■ Ref. 45.

to S(S + 1). The slope of the linear variation of the Curie constant C(emu/mole) values with Mn concentration z in Fig. 3.8 shows that in all cases S = 5/2 for these materials (this will be discussed in more details later) so that values of I_o/k can be obtained from the above data, and these are for zinc blende $I_o/k = -(23 \pm 6)$ Knm^2 and for the wurtzite $I_o/k = -(50 \pm 11)$ Knm^2.

The results for I_o/k allow values to be determined for the exchange between nearest neighbour and next nearest neighbour sites (J_1 and J_2 respectively) which can be compared with particular values quoted in the literature. For the case of $Cd_{0.95}Mn_{0.05}Se$ Aggrawal et al. [54] from measurements of A-exciton splitting give the value of J_1/k as -8.7 ± 0.3 K, while for the same alloy Shapira et al [55] from high field magnetization measurements gives $J_1/k = -8.3 \pm 0.7$ K. In the present work, the value of d for this composition (the hexagonal lattice parameter a_h) is 0.4242 nm (see chapter 2) and hence from equation (3.7), the value of J_1/k is -8.7 ± 0.7 K. For J_2/k the obtained value is -1.1 ± 0.06 K where the spacing r in this case is $\sqrt{2}d$ = 0.6070 nm. For the case of $Cd_{1-z}Mn_zTe$, taking the lattice parameters at z = 0.05, a = 0.6470 nm, so d = 0.4575 nm and $J_1/k = -6.8 \pm 0.4$ K. Shapira et al also quote for $Cd_{1-z}Mn_zTe$ a value of $J_1/k \sim -10$ K.

Ching and Huber [56] for $Cd_{1-z}Mn_zTe$ with $0.4 < z < 0.5$ quote a value of $J_1/k \sim -1.1$ K. As indicated by Shapira et al [55] this is probably J_2/k and not J_1/k. The appropriate value of r in that case is a = 0.647 nm and this gives a value of $J_2/k = -1.1 \pm 0.05$ K from the present results.

The analysis of Geertsma et al [50] indicates that the

exponent α has the value $2(2\epsilon m/\hbar^2)^{\frac{1}{2}}$ where ϵ is the energy difference in the virtual transition and m is the effective mass for the valence band. A reasonable estimate of m is given by the heavy hole mass CdTe which is close to the free electron mass m_o [57]. Thus with m taken as m_o the above values of α give values for ϵ of 0.34 ± 0.05 ev for the zinc blende structure and of 0.61 ± 0.06 eV for the wurtzite case.

Turning now to the Curie-Weiss temperature θ, it seen that in this case also the variation of θ with y at constant z is relatively small. Fig. (3.6), indicates that there is a small increase in θ as y is increased i.e. as Tellerium is replaced by selenium. Extrapolation through the miscibility gap indicates that there is a smooth variation of θ with y and there is no indication of any effect on θ due to the change in crystal structure. Fig. 3.7 shows the variation of θ with z. Since, as was seen above, θ varies smoothly with y, the two edges corresponding to y = 0 and y = 1 show the typical θ vs z variation. It is seen that in both cases there is some curvation of the θ vs z line and this can be attributed to the reduction in lattice parameter as z is increased. Thus the reduction in lattice parameter with higher z values increases the interaction between the manganese ions and results in an increase in θ with z above the linear variation.

After this qualitative description of the dependence of θ on composition, let us try now and make some quantitive predictions of the values of θ for our alloys and then compare it with experimental results.

We know that the standard mean field theory [58] gives

$$k\theta = \frac{2}{3} S(S+1) \sum_i n_i J_i \qquad (3.9)$$

Table 1.1 Values of r_i, distances between cations, and n_i, the number of neighbours at distance r_i, in terms of d the nearest neighbour cation spacing. Values for the zinc blende structure ($d = a/\sqrt{2}$) and wurtzite structure ($d = a$).

Zinc Blende

r_i	d	$\sqrt{2}d$	$\sqrt{3}d$	$2d$	$\sqrt{5}d$	$\sqrt{6}d$	$\sqrt{7}d$
n_i	12	6	24	12	24	8	48

Wurtzite

r_i	d	$\sqrt{2}d$	$\sqrt{\frac{8}{3}}d$	$\sqrt{3}d$	$\sqrt{\frac{11}{3}}d$	$2d$	$\sqrt{5}d$	$\sqrt{\frac{17}{3}}d$
n_i	12	6	2	18	12	6	12	12

where $\sum_i$ represents the summation over consecutive sets of neighbours i.e. 1 nearest neighbour, 2 next nearest neighbour, and where n_i is the number of neighbours in each case and J_i the appropriate value of the exchange parameter. If J_i is assumed to satisfy equation 3.7, and with concentration z of paramagnetic ions, n_i is replaced by zn_i, then

$$\theta = \frac{2}{3} S(S+1) I_o/k \; z \sum_i \frac{n_i \exp(-\alpha r_i)}{r_i^2} \qquad (3.10)$$

For both structure, values of n_i and r_i were calculated out to seventh nearest neighbours (Table 1.1). Then with S, I_o/k and lattice parameter values known, values of θ can be determined from equation 3.10 and compared with the experimentally determined values. This is shown in Fig. 3.12 where the dots represents the experimental values and the curves are calculated. It is seen that very good agreement is obtained and as indicated above, the nonlinearity of the θ vs z line

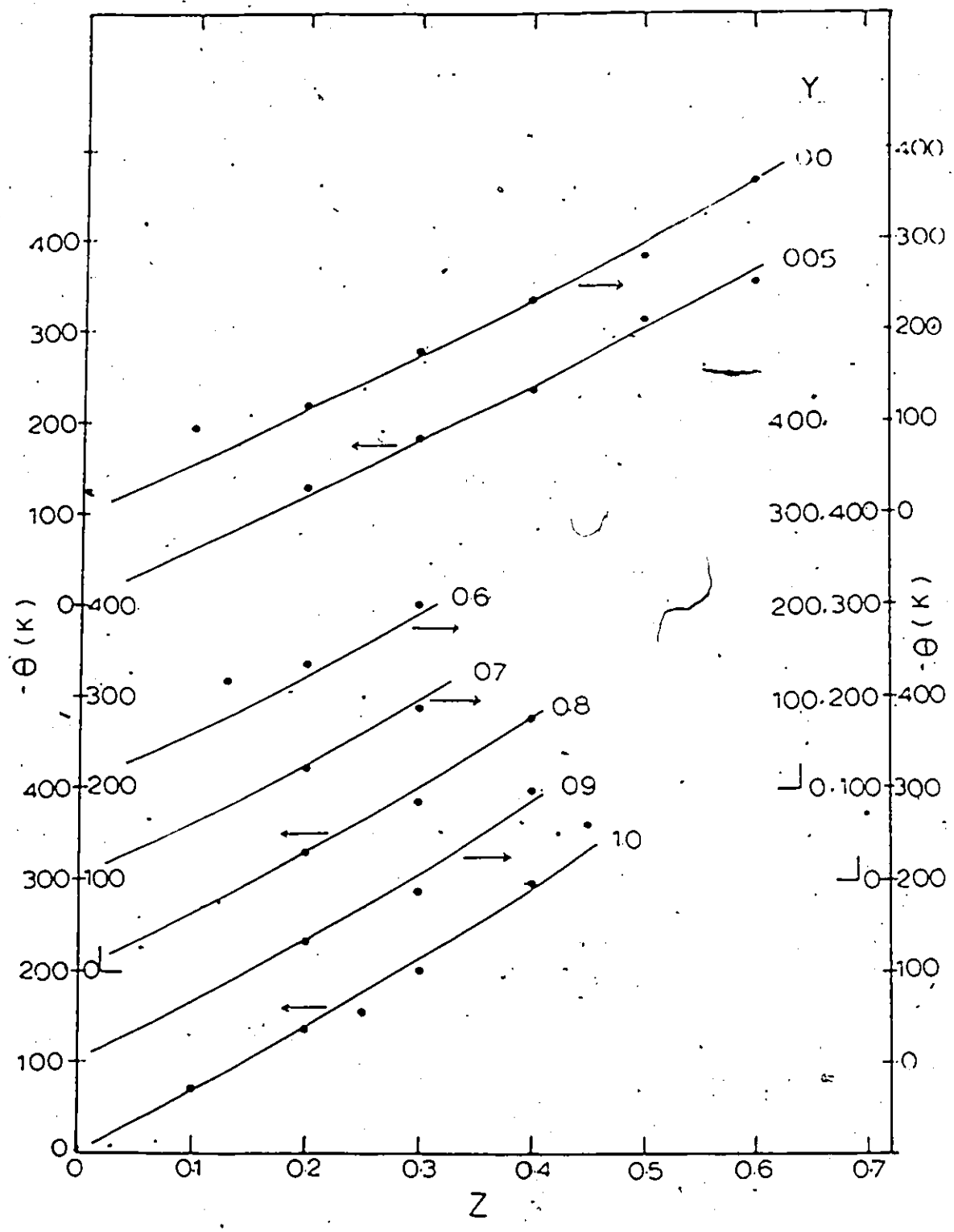

Fig. 3.12. Variation of Curie-Weiss θ with z for $Cd_{1-z}Mn_zTe_{1-y}Se_y$.
Values of y as indicated.
● experimental points ——— predicted curve.

is accounted for by the variation in lattice parameter with z, since this has effect in the $\sum_i$ term of equation 3.10.

Finally the remaining physical constant that can be determined from the magnetic susceptibility measurements is the Curie constant C. This was calculated from the slope of the linear part of the $1/\chi$ vs T curve for each alloy per mole of sample. Fig. 3.6 (c) shows that the variation of C with y at constant z is very small although the graphs indicate a slight increase in C as y is decreased. In Fig. 3.8 it is seen that within the limits of experimental error, C varies linearly with z and extrapolates to C = 0 at z = 0, following by that the equation

$$C_{\text{per mole}} = z \frac{N_A g^2 S(S+1) \mu_B^2}{3k_B}$$

Using g = 2, obtained from the ESR work (see chapter 4), and calculating the slope of the straight line in Fig. 3.8, one can then determine the value of S. This turned out to be equal 2.53 so that we can say that S = 5/2 as expected for Mn^{2+}. (Note that this result was used earlier in the calculation of I_o/k)

3.5 Conclusion

The magnetic susceptibility measurements and the results deduced from them have proved to be very useful in giving valuable information on the magnetic behaviour of the $(Cd_{1-z}Mn_z)(Te_{1-y}Se_y)$ alloys and hence of all the materials belonging to the same class. The spin-glass freezing temperature T_g and its dependence on composition were determined; more specifically T_g has shown a linear variation with the Mn concentration z, extrapolating to $T_g = 0$ at $z \sim 0.2$. This

result is in very good agreement with theoretically calculated percolation limit for nearest neighbour interaction [41-43]. However, values of T_g were obtained by Novak et al [44] for concentration down to $z = 0.05$ which could be explained on the basis of the next and next next etc nearest neighbour interaction having noticeable effect at this low Mn concentrations. Therefore, it was more suitable to study the dependence of T_g upon z using the relation developed by Escorne et al [46] according to which ℓnT_g should decrease in a linear fashion when the mean spacing between the Mn ions increases with decreasing z. Our data have shown this to be true even for $z < 0.2$. This fact has shed new light on the nature of the exchange mechanism taking place between the Mn spins. Accordingly this exchange causes an antiferromagnetic interaction between the Mn^{2+} ions, decreases exponentially with distance and for which the exponent is independent of composition. An exchange mechanism proposed by Geertsma et al [50] seems to satisfy these requirements. It involves virtual transitions between the valence band and a delocalized 3d state. An analysis of our results based on this theory, gave values for J_1/k and J_2/k which were in very good agreement with those determined from very different measurements. The ratio J_1/J_2 was found to be ~6 in the zinc blende and ~8 in the wurtzite structures. Consequently J_2 is smaller but not negligible with respect to J_1 contrary to the assumption made in previous models [38,39].

Values of the energy difference in the virtual transition ε were calculated for both the zinc blende and wurtzite structures. These values were useful to indicate whether the exchange is due to

interaction of the valence band with a 3d band or the conduction band. The valence band-3d transition would probably involve the transition of an electron from the top of the valence band to the $3d^5$ state converting it to $3d^6$ with a resultant energy increase of ϵ. As indicated earlier, ϵ should be reasonably independent of composition for a given structure with values obtained here of 0.35 ev for zinc blende and 0.61 ev for wurtzite samples. For all alloys considered here $E_g > 1.35$ ev (see chapter 5) and hence in all cases, the valence-conduction band spacing is too large for any appreciable interaction. However, in contrast to the present materials it is worth noting that in the case of $Hg_{1-z}Mn_zTe$, the results of Mycielski et al [59] show that when E_g is comparable with ϵ, virtual valence-conduction band transition play a significant role.

Values of the Curie-Weiss paramagnetic temperature θ were obtained for all the investigated alloys. These values were found to be negative conforming to an antiferromagnetic interaction between the Mn^{2+} spins and to decrease (or $|\theta|$ increases) with increasing z which indicates an increase in the antiferromagnetic interaction when we increase the Mn concentration. By using the mean field theory in conjunction with the proposed theory for the exchange parameter (equ. 3.7) we were able to predict values of θ for the alloys which again turned to be in very good agreement with the experimental ones without any adjustable parameter.

With regard to the values of the Curie constant C, they were determined, which enabled us to calculate the spin S of the Mn^{2+} ions in the alloys, S was found to be 5/2.

Finally, it is worth noting that the close agreement obtained between the experimental and calculated values for J_1/k, J_2/k and θ, seems to strongly indicate that the proposed exchange mechanism (eq. 3.7) is actually the one occuring between the Mn spins in the alloys; and consequently we feel a good step forward was made in the understanding of the magnetic behaviour of wide-gap semimagnetic semiconductors, which eventually can lead to a clearer picture of other physical properties which are exchange interaction dependent, namely magneto-optical properties.

References

1. Allan H. Morrish, "The physical Principal of Magnetism", Robert E. Krieger publishing company inc. 1980, ch. 2, 6, 7, and 8.
2. C. Kittel, "Introduction to solid state physics", 5th edition, published by John Wiley & sons, ch. 14, 15 and 17.
3. Peter J. Ford, Contemp. Phys., Vol 23, No. 2, 141 (1982).
4. J.A. Mydosh, J. Mag Mag. Mat. 7, 237-248 (1978); "Magnetism in Solids" some current topics, edited by A.P. Cracknell and R.A. Vawghan, Published by The Scottish Universities Summer School in Physics, ch. 4.
5. K.H. Fischer, Physica B86-88, 813 (1977)
6. A.P. Murani, J. Mag. Mag. Mat. 5, 95 (1977).
7. V. Cannella, and J.A. MyDosh, Phys. Rev. B6, 4220 (1972).
8. V. Cannella, and J.A. MyDosh, A.I.P. Conf. Proc. 10, 785 (1973).
9. C.N. Guy, J. Phys. F5, L242 (1975).
10. C.N. Guy, J. Phys. F7, 1505 (1977a).
11. C.N. Guy, Physica B 86-88, 877 (1977b).
12. C.N. Guy, J. Phys. F8, 1304 (1978).
13. H. Sato, S.A. Werner and R. Kikuchi, J. Physics (Paris) 35, C4-25 (1974).
14. A.P. Murani, Phys. Rev. Lett. 37, 450 (1976).
15. A.P. Murani, and J.L. Tholena, Solid State Commun 22, 25 (1977).
16. C.E. Violet, and R.J. Borg, Phys. Rev. 149, 540 (1966).
17. C.E. Violet, and R.J. Borg, Phys. Rev. 162, 608 (1967).
18. A.P. Murani, J. Physique C6, 1547 (1978a).

19. L.E. Wenger, and P.H. Keesom, Phys. Rev. B11, 3497 (1975).

20. L.E. Wenger, and P.H. Keesom, Phys. Rev. B13, 4053 (1976).

21. G. Toulouse, Comm. Phys. 2, 115 (1977).

22. G. Toulouse, "Modern Trend in the Theory of Condensed Matter" Lecture note in physics, 115 edited by A Pekalski and J. Przystawa p.195 (1980).

23. J. Ziman, "Principle of the Theory of Solids", Cambridge University press, ch. 10, (10.6).

24. L. Deseze, J. Phys. C10, L353 (1977).

25. J. Villain, Z. Phys. B33, 31 (1979).

26. C. Lewiner, J.A. Gaj and G. Bastard, J. Physique 41, C5-289 (1980).

27. J. Ginter, J. Kossut, and L. Swierkowski, Phys. Stat. Sol. (b) 96, 735 (1979).

28. N. Bloembergen and T.J. Rowland, Phys. Rev. 97, no.6, p.1679 (1958).

29. M. Cardonio and C. Messana, Rev. Sci. instrum, vol.48 no.3, p.300 (1977).

30. J.S. Philo and W.M. Fairbank, Rev. Sci. instrum. vol.48 no.12 p.1529 (1977).

31. E.J. Cukauskas, D.A. Vincent and B.S. Deaver Jr., Rev. Sci. instrum. vol.45 no.1, 1 (1974).

32. S.B. Oseroff, Phys. Rev. B25, 6584 (1984).

33. S. Nagata, P.H. Keesom and H.R. Harrison, Phys. Rev. B19 no.3, 1633 (1979).

34. L. Neel, Adv. Phys. 4, 191 (1956).

35. N.B. Brandt and V.V. Moshchalkov, Adv. Phys. 33 no.3, 193 (1984).

36. S. Oseroff, F. Acker, Solid State Commun 37, 19 (1980).

37. M. Escorne and A. Mauger, Phys. Rev. B25, no.7, 4674 (1982).

38. S. Nagata, R.R. Galazka, D.P. Mullin and J.K. Furdyna, Phys. Rev. B, 22, no.7, 3331 (1980).

39. S. Nagata, R.R. Galazka and P.H. Keesom, Phys. Rev. B22, no. 7 3344 (1980).

40. L. Tholence and R. Tournier, J. Phys. (Paris) 35, C4-229 (1974).

41. C. Domb and N.W. Dalton, Proc. Phys. Soc. London 89, 889 (1966).

42. G.S. Grest and E.G. Gable, Phys. Rev. Lett. 43, 1182 (1979).

43. H.L. Frisch, E. Sonnemblick, V.A. Vyssotsky and J.M. Hammersley, Phys. Rev. 124, 1021 (1961).

44. M.A. Novak, S.B. Oseroff and O.B. Symko, Physica 107B, 313 (1981). J. Appl. Phys. 57, 3418 (1985).

45. M.A. Novak, O.B. Symko, D.J. Sheng and S. Oseroff, Physica 126B, 469 (1984).

46. M. Escorne, A. Mauger, R. Triboulet and J.L. Tholence, Physica 107B, 309 (1981).

47. T. Donofrio, G. Lamarche and J.C. Woolley, J. Appl. Phys. 57, 1937 (1985).

48. M. Escorne and A. Mauger, Phys. Rev. B, 25, 4674 (1982).

49. B.E. Larsoon, K.C. Hass, H. Ehrenreich and A.E. Carlsson, Solid State Comm. 56, 347 (1985).

50. W. Geertsma, C. Hass, G.A. Sawatzky and Vertogen, Physica 86-88B, 1039 (1977).

51. G.E.T. Gonzalves da Silva and L.M. Falicov, J. Phys. C5, 63 (1972).

52. S. Manhas, A. Manoogian, G. Lamarche and J.C. Woolley (in the press).

53. P.W. Anderson, Solid State Physics 14, p.142 (1963).

54. R.L. Aggarwal, S.N. Jasperson. Y. Shapira and A. Wold, Proc. 17th Int. Conf. Phys. Semicond. San Francisco p.1419 (1984).

55. Y. Shapira, S. Foner, D.H. Ridgley, K. Dwight and A. Wold, Phys. Rev. B30, 4021 (1984).

56. W.Y. Ching and D.L. Huber, Phys. Rev. B26, 6164 (1982).

57. K. Zanio, Semiconductors and semimetals 13, 91 (1978).

58. J.S. Smart, Magnetism vol.III (ed. G.T. Rado and H. Shull - Academic press N.Y.) p.63 (1963).

59. A. Mycielski, G. Rigaux, M. Menant, T. Dietland, M. Otto, Solid State Commun. 50, 257 (1984).

60. H.H. Heikens, R.S. Kuindersma, C.F. Van Bruggen and C. Hass, J. Mag. Mag. Mat. 8, 130 (1978).

Chapter 4

Electron Spin Resonance Measurements

4.1 Introduction

Consider an ion with a permanent magnetic moment. If the ion is free and has a resultant angular momentum quantum number J, the application of a static magnetic field H will produce Zeeman splitting of the 2J + 1 states into levels with energies of $M_J g\mu_B H$; M_J is the magnetic quantum number and g is the Lande splitting factor. If the ion forms a part of a crystalline solid and is not free, its angular momentum may be described by a spin quantum number S. In a field H, the energies of the split 2S + 1 levels can again be written as $M_S g\mu_B H$, except that here g is a splitting factor that makes the energy difference between levels, $g\mu_B H$, come out correctly. In general, g is not equal to Lande value, and its deviation from the latter is due to the crystalline field effect on the orbital angular momentum of the ion. According to quantum mechanics, a selection rule operates so that for magnetic dipole radiation only the transitions between adjacent levels for which $\Delta M_S = \pm 1$ is possible. Transitions between levels can be induced by the application of an oscillating magnetic field whose frequency is $\hbar\omega = -g\mu_B H$ or

$$\omega = \frac{-ge}{2mc} H \qquad (1.4)$$

This is just the classical Larmor frequency [1] modified to include the effect of the spin by the inclusion of the factor g. For a system of ions in thermal equilibrium the lowest energy levels will have the

greatest population. Consequently, even though individual transitions for emission or absorption have equal probability, there is a net absorption of energy from the radiation field that can be observed experimentally. Since the absorption occurs only for frequencies at or near the Larmor frequency, the phenomenon is called "Paramagnetic Resonance "or" Electron Spin Resonance".

The Electron Spin Resonance has been found to be an effective technique which can be used in the investigation of the dynamic of the spin system, spin-spin interaction and related relaxation processes, as well as internal magnetic fields experienced by the spins in the solid. These kinds of information are usually revealed by the position and width of the resonance line, as well as by the changes that might occur in any one of these two, when the temperature is changed. These kinds of information obtained from ESR measurements carried out on all single-phase samples of our alloy system, are expected to be very useful in substantially improving our understanding of the magnetic behaviour of these and similar materials.

In our system $(Cd_{1-z}Mn_z)(Te_{1-y}Se_y)$, the manganese ion, Mn^{2+} has a permanent magnetic moment; and this is a consequence of the $3d^5$ electronic configuration of the ion. The ground state spectroscopic term, according to Hund's rules, will be $^6S_{5/2}$, with a degeneracy of $(2S + 1)(2L + 1) = 6 \times 1 = 6$. Such a spherically symmetric ground state cannot be directly affected by a crystalline electric field. However, it has been known that a field splitting of this state does occur. This splitting is assumed to be due to an admixture of higher lying levels into the ground state. Physical mechanism that can

account for such admixing involve high order process consisting of a combination of the effects of crystalline field, spin-orbit coupling and spin-spin interaction [2-5].

Consequently, a cubic or a nearly cubic crystal field (a tetrahedral crystal field in our case) splits the free-ion ground-state sextet into two levels, the upper fourfold degenerate at +a, the lower two fold degenerate at -2a; a is the cubic crystal field splitting parameter. In the presence of a magnetic field, the Zeeman interaction lifts the degeneracy of the quartet and doublet and splits them into a total of six spin states [4,5]. The fine structure splitting in a cubic crystal field plus an external magnetic field applied along a fourfold symmetry axis, is illustrated in Fig. 4.1.

Nearly all (~ 100%) of the Mn^{2+} isotopes have nuclear spin I = 5/2. As a result, each fine structure line is split into 2I + 1 = 6 hyperfine lines. The splitting of the M_S = 1/2 + -1/2 fine structure line, for example, is illustrated in Fig. 4.2.

According to the theory [2,4,5], the deviation of the Mn^{2+} ion g-value from the free spin value of 2.0023 is expected to be very small ($\Delta g \sim 0.0004$). This was confirmed by the experiment [5,7] and the g-value of Mn^{2+} in any compound possessing a cubic or near cubic crystal field was found to be, to a good approximation, the same as that of the free ion.

The two non-magnetic compounds that our alloy system involves are CdTe and CdSe. The former has the zinc blende structure and the latter has the wurtzite structure. Both structures have tetrahedral symmetry i.e. four-fold coordination; hence every cation is surrounded

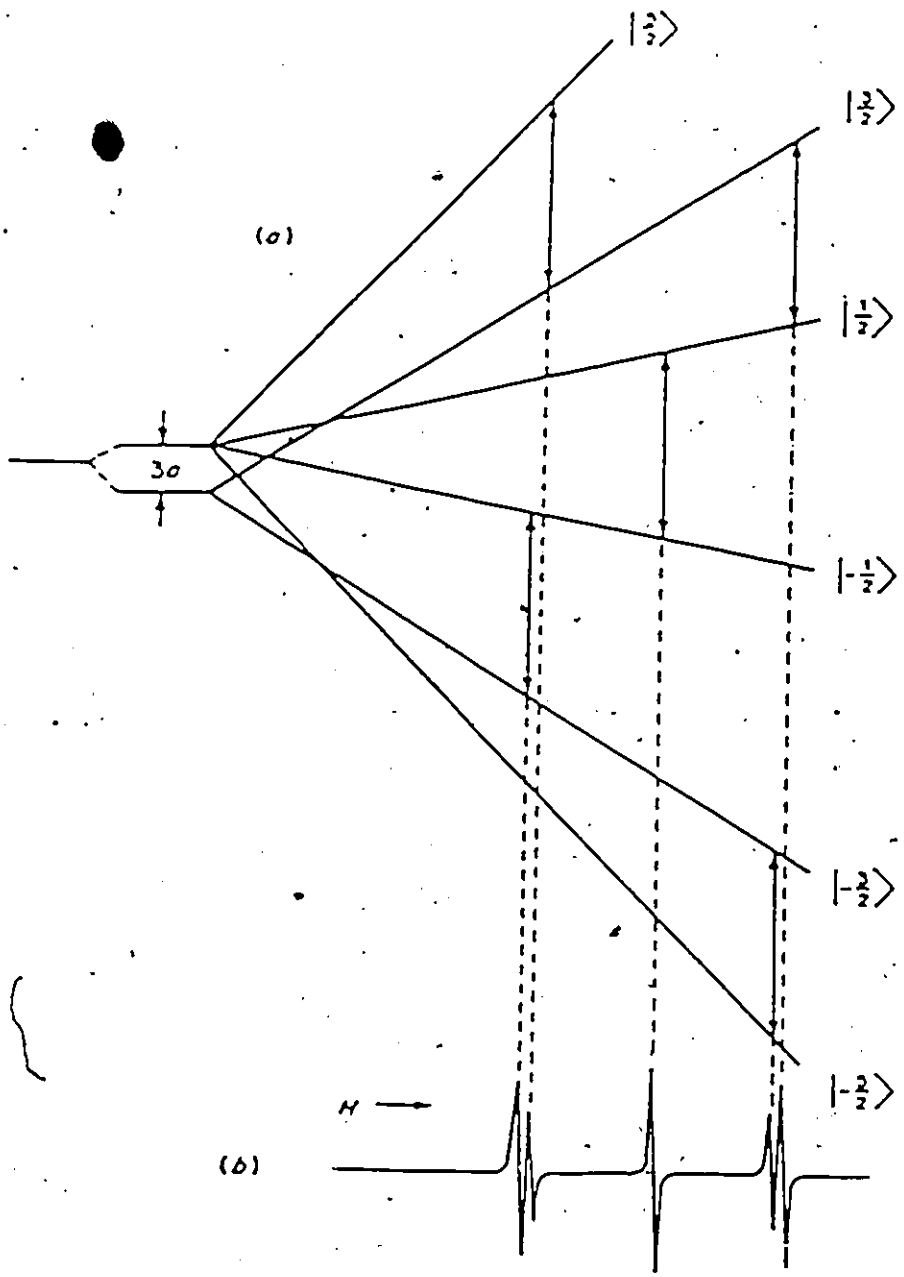

Fig. 4.1. (a) Energy level diagram for a $3d^5$ ion in cubic crystal field. (b) The allowed ESR spectrum is shown for $h\nu >> 3a$.

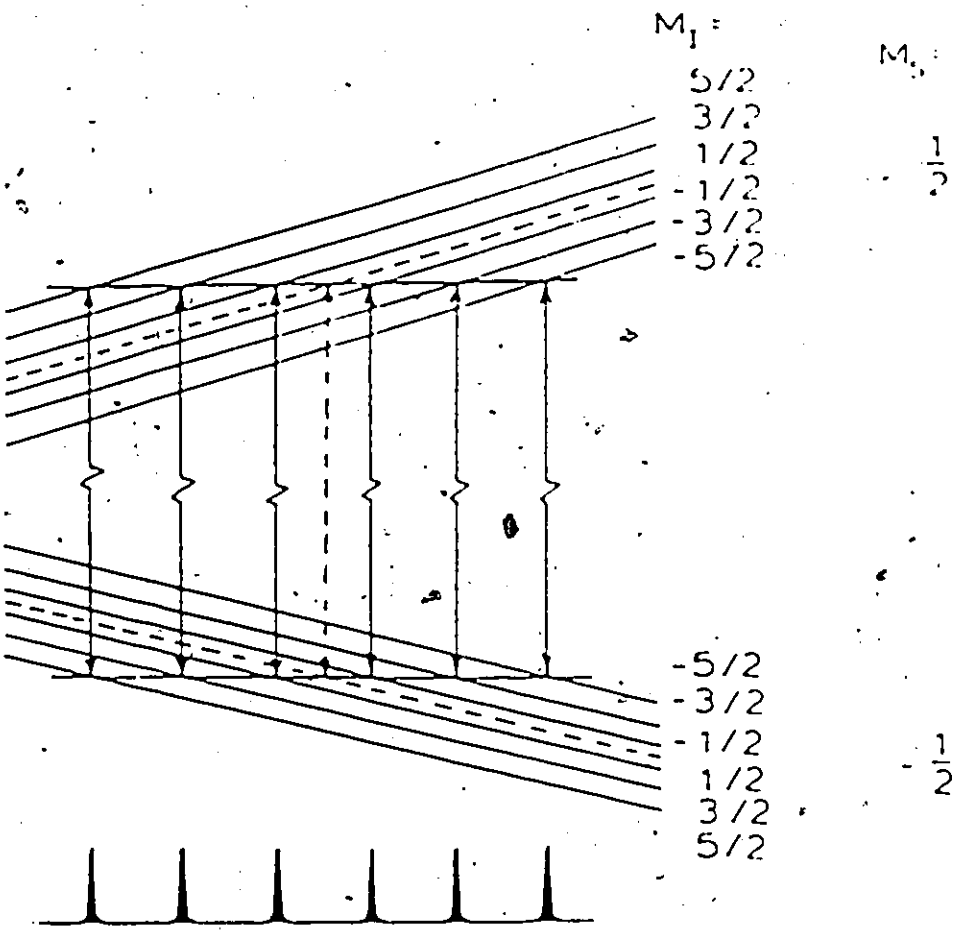

Fig. 4.2. Hyperfine splitting of the $M_s = 1/2 \rightarrow -1/2$ fine structure ESR line of Mn^{2+}.

by four anions occupying the corners of a regular tetrahedron (and vice versa). Consequently when a Mn^{2+} ion replaces a Cd^{2+} ion in any of these two compounds, it will be subject to a tetrahedral crystal field.

ESR experiments were carried out on CdTe crystals containing manganese (~ 0.01%) by Kikuchi et al [8]. A well resolved hyperfine structure was observed at 4.2 K, with the sextet of the principal lines corresponding to the $M_S = -1/2 \rightarrow 1/2$ transition having the largest intensity. The g value obtained was of 2.010 which is very close to the free spin g-value. Similarly, Mn in CdSe showed the same kind of results with a g-value of 2.003 [9].

More recently, the ESR spectra of single crystals $Cd_{1-z}Mn_zTe$ ($0.001 < z < 0.60$) and $Cd_{1-z}Mn_zSe$ ($0.001 < z < 0.45$) have been studied by Oseroff [10-13]. According to him, at room temperature the spectrum was almost independent of frequency for both system. For $z < 0.005$ a well-resolved hyperfine structure was observed. For $z > 0.005$ the hyperfine lines initially broaden due to dipole-dipole interaction, eventually becoming a single broad line for $z \sim 0.015$. The linewidth narrows as z increases up to $z \sim 0.03$ due to exchange narrowing. For $z > 0.03$ the linewidth broadens monotically with increasing concentration at all temperature measured. Oseroff has also measured the angular dependence of the ESR line and found that there is a very small variation of linewidth = 3% independent of concentration. Consequently, there should be no significant difference between ESR line obtained from a single crystal and that from a polycrystalline in these materials.

4.2 Experimental procedures

The ESR measurements were carried out in Dr. Armen Manoogian laboratory under his supervision and with the technical assistance of the technicien specialist B.W. Chan.

A schematic diagram of the spectrometer system used in this work is represented in Fig. 4.3. It consists of a Klystron producing microwave power at X-band microwave frequency (~ 9.2 GHz). The produced microwave power can propagate in a microwave bridge, known as the "magic" T, which consisted of four-armed wave guide structure allowing the microwave power to feed into the sample cavity through one arm, and the power that is reflected back from the cavity to leave by a separate arm to the detection system. Moreover, the arm opposite the sample cavity can be used to control the amount of power entering the detection system. The slide-screw tuner contains a pin which can be inserted into the path of the microwave, and can also be moved along the length of the waveguide comprising the slide-screw tuner. The attenuator consists of a mica card covered with carbon that can absorb nearly all the microwave power that is not reflected back by the pin and hence that reaches the attenuator. As a result the pin depth of the slide-screw tuner changes the amplitude of the microwave, while the position of the pin along the tuner changes the microwave phase. The crystal detector consists of a silicon rectifier mounted in the wave guide. The rectifier detects the high frequency microwave power and changes it to a direct current (d.c.) voltage. Lower frequencies however, even up to several tens of megacycles, are able to pass through without being changed to d.c. The microwave resonant sample

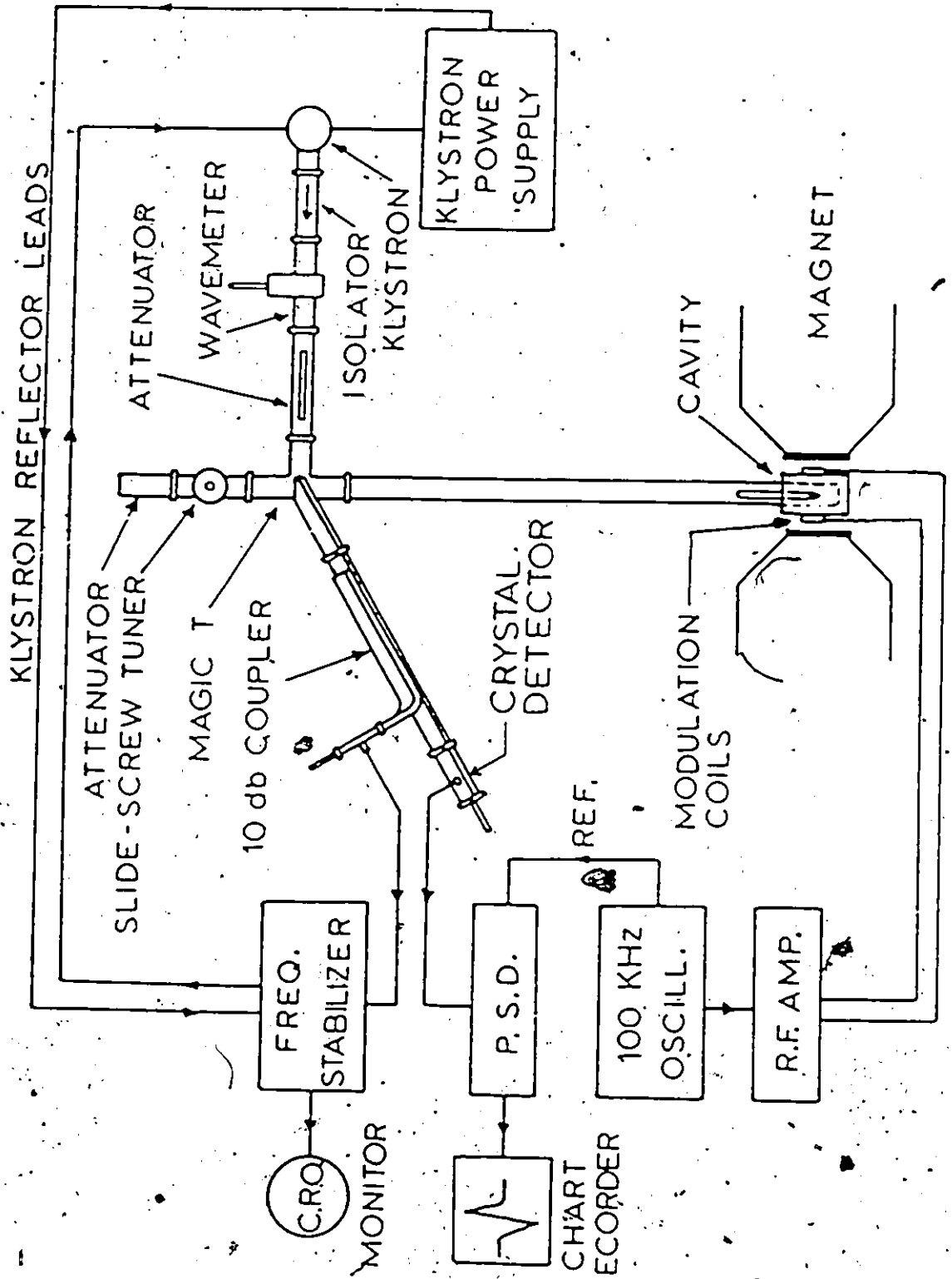

Fig. 4.3. Electron Spin Resonance spectrometer system.

cavity is a piece of a waveguide with copper plates soldered on each end, one end of which has a hole of 1/4 inch in the center to allow the microwave to enter the cavity. The length of the cavity is one wavelength.

A frequency stabilizer keeps the microwave frequency stabilized against the resonance frequency of the sample cavity. A phase sensitive detector (PSD) is employed when recording signals on a chart recorder. While it is being swept, the magnetic field is modulated at 100 KHz by means of a pair of Helmotz coils mounted on the cavity two opposite walls which face the two poles of the magnet. The derivative of the ESR absorption lines is then produced on the chart recorder, and the peak to peak linewidth ΔH is measured with an NMR gaussmeter; also the resonance field H_R is defined from the zero of the derivative curve (see Fig. 4.4).

The temperature of the sample can be controlled in the range between 10 K and 500 K. Circulating nitrogen gas around the sample cavity is used for the temperature control between 500 K and 90 K; whereas helium gas is used for the same purpose, between 90 K and 10 K. The temperature of the sample is measured by means of a thermocouple which can be in direct contact with the sample. A gold-chromel thermocouple is used for temperature below 300 K, and a copper-constantan thermocouple for temperatures above 300 K. Thus ESR measurements can be carried out at various temperatures.

4.3 Results

The ESR measurements were carried out on all the samples in

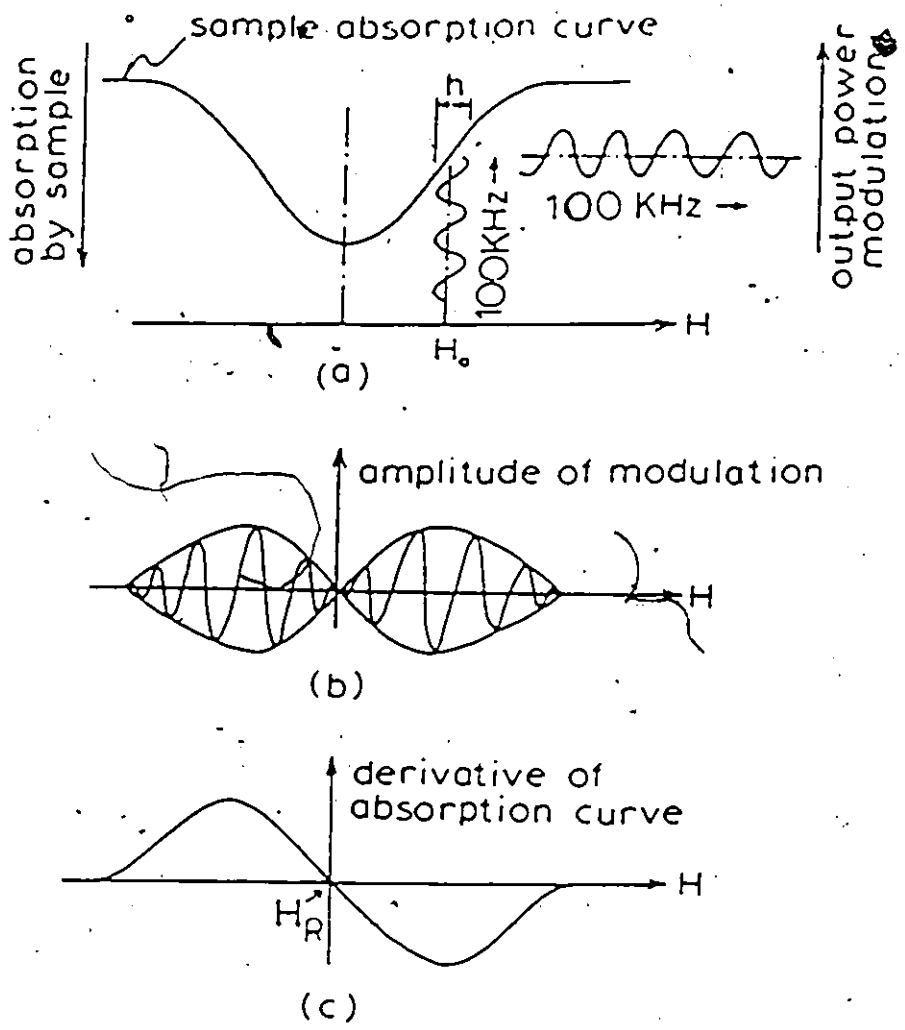

Fig. 4.4. Effect of the modulation on ESR absorption line. (a) shows that the 100 KHz modulation field causes the microwave power in the cavity to be modulated at the same frequency when the sample absorbs power at resonance. As the steady field H_o is slowly swept through the absorption curve the amplitude of the modulation of the microwave power changes in proportion to the absorption curve as shown in (b). The modulated microwave power travels from the cavity to the crystal detector where it is demodulated and the 100 KHz signal passes to PSD (Phase Sensitive Detector). The output signal from the PSD gives the first derivative pattern of the ESR line on the chart recorder as shown in (c).

the two single-phase fields: zinc blende and wurtzite. At room temperature all samples produced a single symmetric and broad ESR line due to manganese with the broadening being proportional to the manganese concentration; and the resonance field H_R was observed to be consistent with a g value of 2.0.

The resonance linewidth ΔH was measured as a function of temperature within the interval 10 to 500 K. In all cases the line width increased with decreasing temperature, remaining symmetrical in the higher temperature range. However at lower temperatures, where ΔH began to increase appreciably, the lineshape was observed to broaden asymmetrically and finally to split into two parts, with the amount of splitting increasing with further lowering of the temperature. At this point the line intensities decreased and quickly fell to almost zero with further cooling of the sample. This effect was most easily seen for samples with $z > 0.2$ since in those cases this low temperature behaviour was above the 10 K lower temperature limit of the equipment used. Fig. 4.5 shows the lineshape at selected temperatures for the sample with $z = 0.3$, $y = 1.0$, which is typical results. When the line becomes asymmetrically broadened, the low field part of the line remains essentially unchanged in shape but the high field part becomes greatly broadened and flattened out. It is worth noting that Sayad and Bahagat, in their ESR work on $Cd_{1-z}Mn_zTe$ [14] have reported that ESR lineshape for each of these alloys remains Lorentzian down to a certain temperature below which the line becomes asymmetric.

Typical sets of ΔH vs T curves are shown in Figs. 4.6-4.8. Fig. 4.6 shows these for the alloys with $y = 0.05$ in the zinc blende

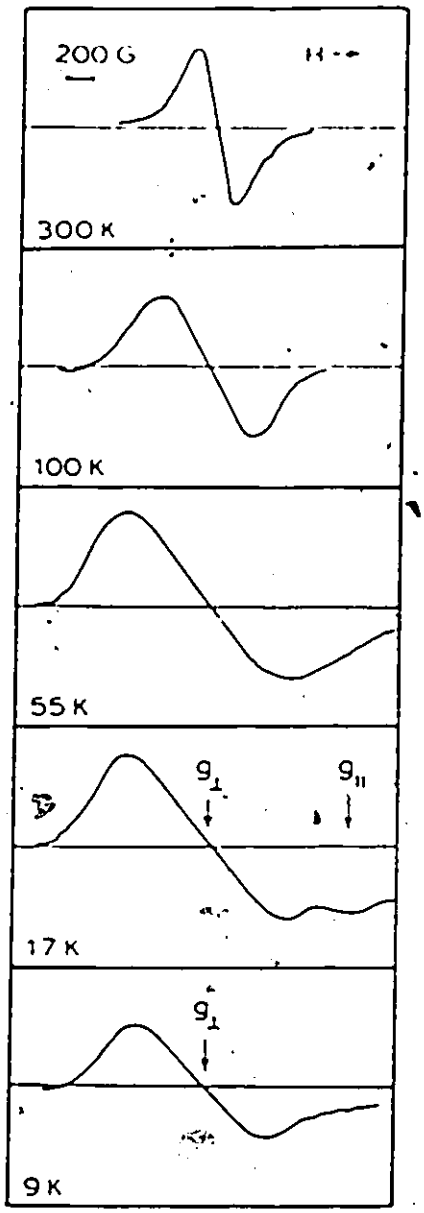

Fig. 4.5. Mn ESR lineshape at several temperatures for the sample with z = 0.3, y = 1.0.

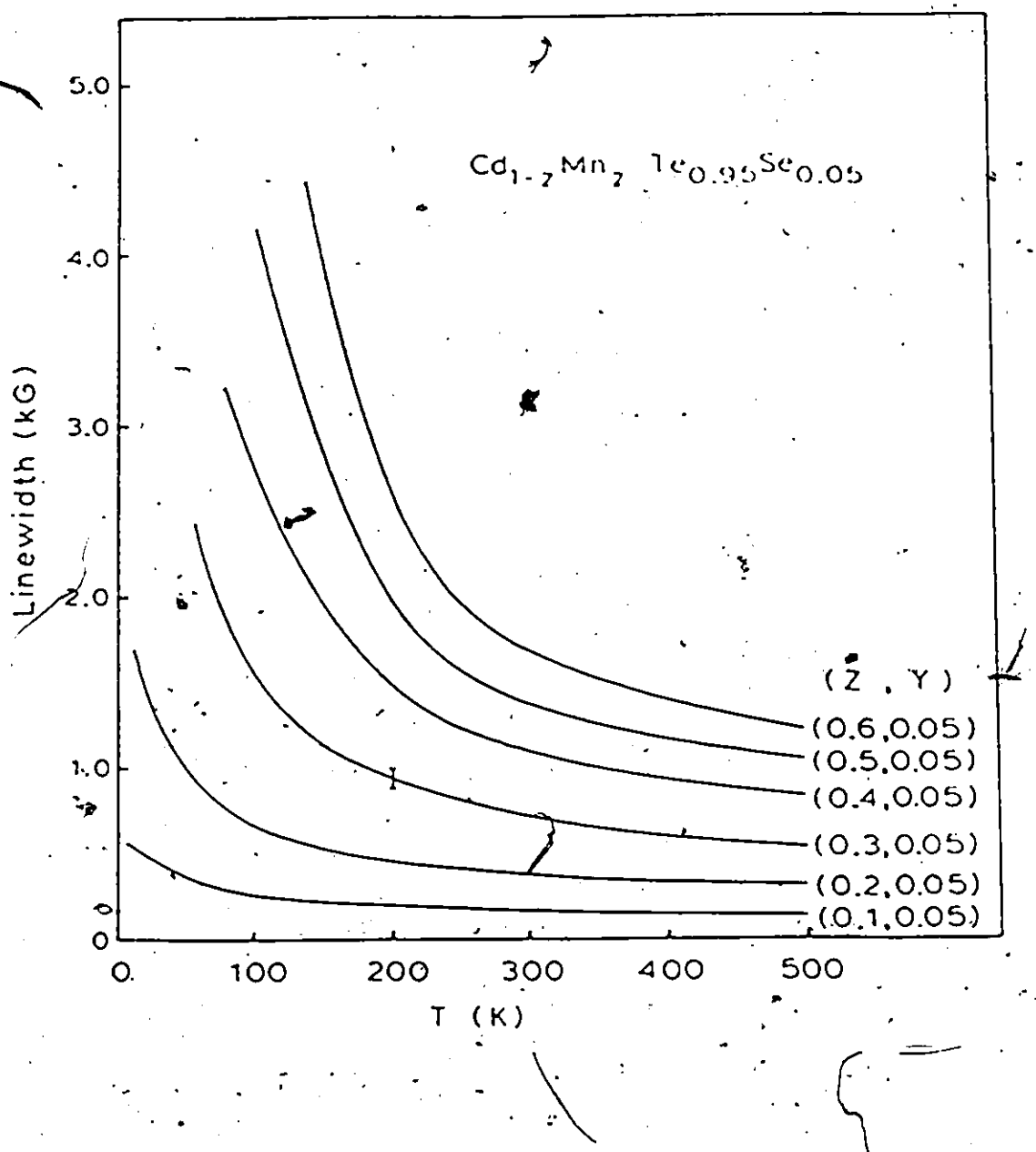

Fig. 4.6. Mn ESR linewidth versus temperature for the alloys with y = 0.05 in the cubic a field. A typical error bar for the experimental results is shown on one of the curves.

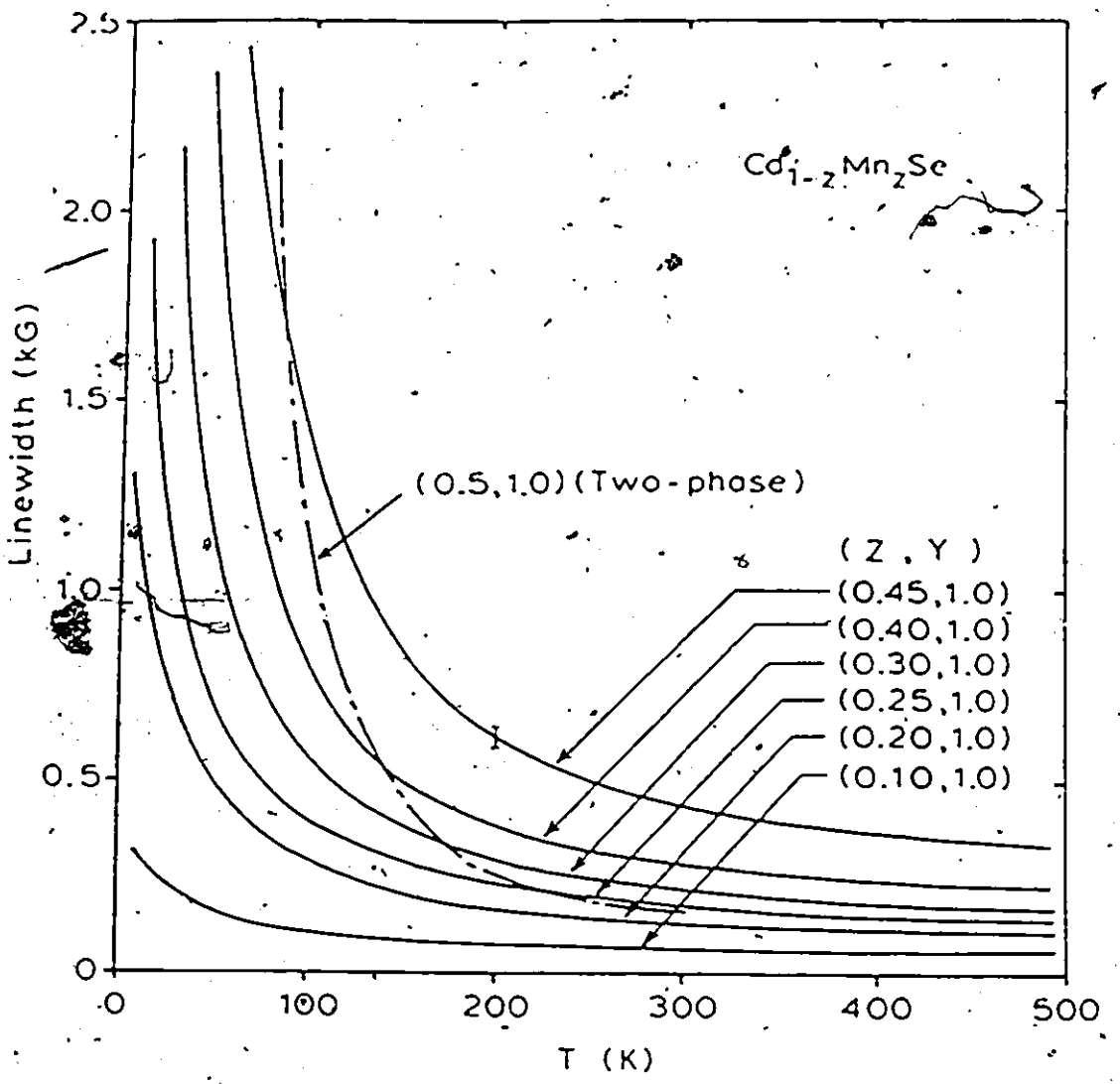

Fig. 4.7. Mn ESR linewidth versus temperature for the alloys with y = 1.0 in the hexagonal β field. A typical error bar for the experimental results is shown on one of the curves.

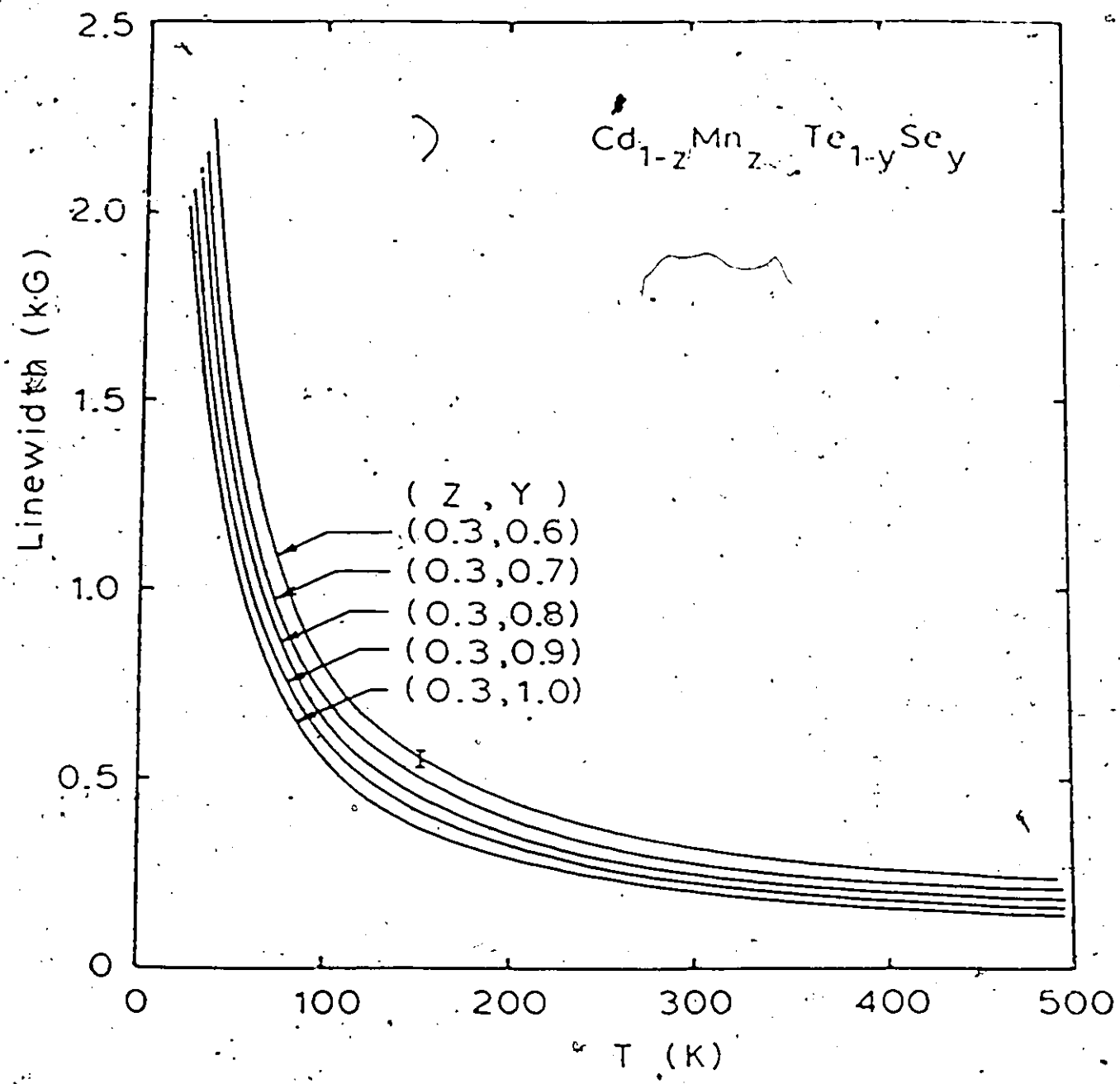

Fig. 4.8. Mn ESR linewidth versus temperature for the alloys with $x = 0.1$ in the hexagonal B field. A typical error bar for the experimental results is shown on one of the curves.

field. Fig. 4.7 shows ΔH vs T curves for the alloys with y = 1.0 in the wurtzite field; here the curve for the sample with z = 0.5, y = 1.0 is seen to be out of the step with the rest of the curves in the sequence indicating that this sample is not single phase, in agreement with the x-ray diffraction results (see chapter 2). Finally Fig. 4.8 shows ΔH vs T curves for the alloys with z = 0.3 in the wurtzite field. In each of these figures (4.6-4.8) a typical error bare for the experimental results is shown on one of the curves.

4.4 Analysis and discussion

As we mentioned above, Fig. 4.5 represents a typical example of the evolution of the ESR line with respect to the temperature; the shape that our ESR line takes when it becomes asymmetric (with its low-field half remaining essentially unchanged in shape and its high-field half becoming greatly broadened and flattened out) is very similar to the calculated ESR line shapes by Searl et al [16-18] for a random polycrystalline assembly of uniaxial crystals having uniaxial g-value anisotropy. According to Searl's work the asymmetric line shapes in such substances could be explained on the basis of the uniaxially anisotropic g-value with $g_\perp > g_\parallel$. ($g_\perp$ is the g-value when the magnetic field is perpendicular to the symmetry axis, and $g_\parallel$ is that when the magnetic field is parallel to the symmetry axis). Also, Searl maintains that his calculations would hold equally well for a random arrangement of free radicals showing uniaxial symmetry in a magnetic field. Consequently, we suggest that the Mn clusters, in our case, can play the same role as those uniaxial crystallites of a

polycrystalline substance or these free radicals in a magnetic field. As we indicated previously, we are dealing with random substitutional solid solution alloys in which the statistical fluctuations in concentration give rise to microscopic regions more concentrated in solute (manganese) atoms than other regions. The spins within such regions become more and more antiferromagnetically correlated, when lowering the temperature, forming what is known as manganese magnetic clusters. It is the antiferromagnetic interaction inside each of these clusters, which gives rise to an uniaxial anisotropy field and hence to the Mn clusters magnetic uniaxial symmetry which is assumed to be randomly distributed over all directions. Consequently, in the lower temperatures region, the g-value of the manganese magnetic complexes becomes axially symmetric with $g_{\perp} > g_{\parallel}$ which causes the asymmetry of the ESR line when $g_{\perp}$ is slightly larger than $g_{\parallel}$, and then the split of the line into two parts when the difference $(g_{\perp}-g_{\parallel})$ becomes more significant. This is illustrated in Fig. 4.5.

Turning now to the variation of the linewidth with temperature (Figs. 4.6-4.8), we were faced by a number of difficulties in our attempts to fit the experimental data of ΔH vs T to an expression which has a physical significance; and that is because there has not been any theory developed yet for the interpretation of the dependance of the ESR linewidth on temperature for this class of materials (SMSC's).

At first we tried to follow the steps of Oseroff in his ESR work on $Cd_{1-z}MnTe$ [11], where he analysed the ESR linewidth values in terms of Huber's expression [19] which was developed for antiferromagnets above the Neel temperature:

$$\Delta H = A\left(\frac{T_c}{T-T_c}\right)^{-\alpha} + B \qquad (2.4)$$

where B is the high temperature linewidth, T_c is the "transition temperature", α is a "critical exponent" and A is an empirical parameter. This is the standard form used to analyse critical phenomenon results. This analysis attributes the increasing linewidth to a rising relaxation rate as the transition temperature was approached from above. Oseroff obtained the values of all four parameters T_c, B and A from the best-fit condition. The results obtained for A and α suffered from an inconsistent variation with composition, moreover the values of the "critical exponent" α varied as much as an order of magnitude. What we did instead, is to analyse the data by employing a log-log plot such as

$$\log(\Delta H - B) = \alpha \log\left[T_c/(T - T_c)\right] + \log A \qquad (3.4)$$

It was observed that a straight line could be drawn through the calculated points only for the case of B = 0 with values of α were found to fall within the range of $\alpha = 0.33 \pm 0.08$.

The values of T_c which fit this analysis, were chosen as the temperatures at which the Mn resonance lines became very broad and showed asymmetry and appreciable decrease in intensity. However these values were considerably higher than the T_g values obtained from the magnetic susceptibility, furthermore the fact that B should be zero is not physically meaningful, because is not possible to have a zero line width at very high temperature ($T \to \infty$) in the paramagnetic region, which was implied by this analysis, also it is not possible that the very existence of the linewidth and its broadening at all temperatures is a result only of the critical effects represented by the term

$A(\frac{T_c}{T-T_c})^{\alpha}$. Consequently equation (2.4) had to be discarded as a good expression representing ΔH vs T in our case.

In subsequent work [10,12,13], Oseroff used a modified Huber expression to fit the data of ΔH vs T for $Cd_{1-z}Mn_zTe$ and $Cd_{1-z}Mn_zSe$;

$$\Delta H = A(\frac{T_c}{T-T_c})^{\alpha} + B(1 - \frac{\theta}{T}) \qquad (4.4)$$

equation (4.4) is little more complicated than equation (2.4) because the parameter B is replaced by the term $B(1 - \frac{\theta}{T})$ giving a $\frac{1}{T}$ variation for the high temperature linewidth. Here θ is the "paramagnetic Curie Weiss temperature" which is negative in these materials. This newly introduced term was developed for antiferromagnets, by Jaccarino et al [20], to account for the non-critical high-temperature dependence of the ESR linewidth i.e. when $T >> T_N$. Oseroff also used the best-fit condition in his analysis to obtain values of all the parameters in expression (4.4). Once again his values of the "critical exponent" α varied between 0.2 and 2.0 for $Cd_{1-z}Mn_zSe$ and between 0.3 and 1.5 for $Cd_{1-z}Mn_zTe$ with Mn concentration. This is a very big variation for a critical exponent which is theoretically supposed to be constant for a same critical phenomenon taking place.

We also tried to analyse our experimental data of ΔH vs T, in term of expression (4.4). The first step we made was to plot the experimental values of $T\Delta H$ as a function of T and that to verify the validity of the second term of Equ. (4.4), $B(1-\frac{\theta}{T})$. In the high temperatures region, if ΔH is due mainly to the paramagnetic contribution ΔH_p represented by $\Delta H_p = B(1-\frac{\theta}{T})$, the plot of $T\Delta H$ against T should then be linear in this temperatures region. In Fig. (4.9) which shows examples of such plots for the edge with y = 1, it is observed

that for each plot a linear behaviour is obtained down to a certain temperature below which there is a deviation from linearity. Values of the parameters B and θ could be obtained from the slope and the intercept of the linear part respectively. The values obtained for θ in this way for all the samples were in good agreement with those obtained from the magnetic susceptibility measurements (see ch. 3); also the values for B varied systematically with composition. All these were positive arguments in favour of the validity of the $B(1 - \frac{\theta}{T})$ term in describing the ESR linewidth dependance on temperature in the purely paramagnetic high temperatures region.

The second step was to verify the validity of the contribution of the second term $\Delta H_c = A(\frac{T_c}{T-T_c})^{\alpha}$ to ΔH in the lower temperatures region. What we did was to calculate the paramagnetic contribution $\Delta H_p = B(1-\frac{\theta}{T})$ using the values of θ and B obtained from the graph of TΔH vs T, and that down to the lowest measurement temperature; then the difference $(\Delta H - \Delta H_p) = \Delta H_c$ represents the contribution due to the critical term $A(\frac{T_c}{T-T_c})^{\alpha}$. Afterwords, the thing to do would be to plot log ΔH_c against log $(\frac{T_c}{T-T_c})$. These plots should have a linear variation, with α as slope and log A as intercept. In fact, these plots were linear, but in a short range of temperatures in the vicinity of T_c, with a value of α obtained, in every case, falling close to 0.5 which is the value that the mean field theory [21] would give for the magnetization exponent α. However, in a recent ESR work carried out by Furdyna on $Cd_{1-z}Mn_zTe$ using the Faraday rotation technique [22] (which is an indirect technique for measuring ESR), Furdyna observed a

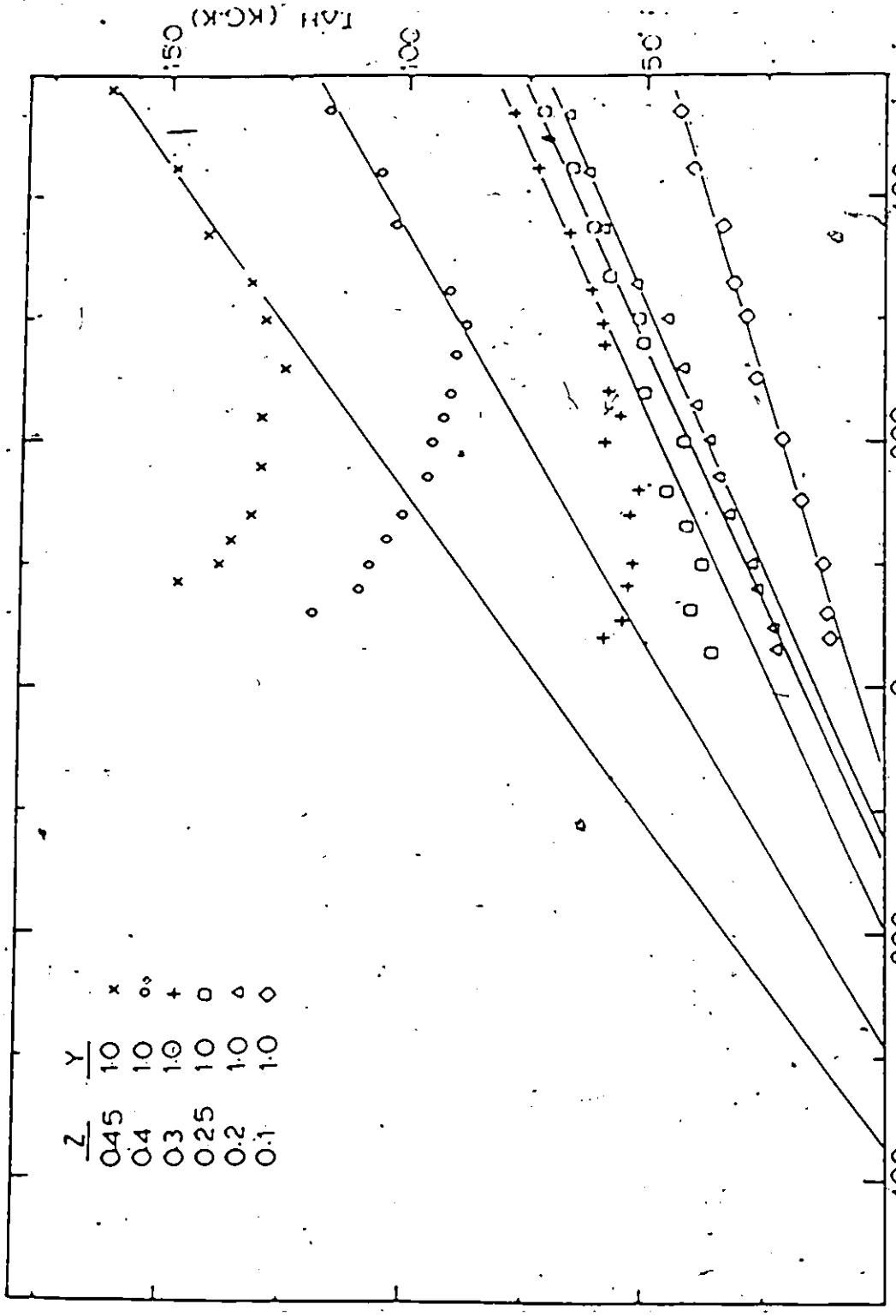

Fig. 4.9. Variation of the values of TΔH with temperature for the alloys with y = 1.

continuous increase in the linewidth with lowered temperatures and that even below our T_c values. Consequently no critical phenomenon was observed at T_c. As results of Furdyna's observations and the poor fit obtained from the analysis using the critical term $A(\frac{T_c}{T-T_c})^{\alpha}$, the latter term had to be discarded as being the right term accounting for the increase of ΔH in the lower temperatures region.

Therefore, the expression of ΔH had to be rewritten as $\Delta H = F(T) + B(1-\frac{\theta}{T})$, where $F(T)$ is an unknown function of temperature the form of which had to be found.

It has been recently suggested by Bhagat and co-workers [15] that the variation of ΔH with temperature is due to the resonance line being inhomogeneously broadened because of the random distribution of the Mn^{2+} ions. They showed that the variation of ΔH due to this effect can be represented by an empirical expression of the form:

$$\Delta H = \Gamma \exp(-\frac{T}{T_o}) + \Gamma_o$$

where Γ_o is the high temperature linewidth and and T_o are empirical parameters associated with the freezing of the spins. They plotted $\ln(\Delta H - \Gamma_o)$ against T for data of $Cd_xZn_yMn_zTe$, and obtained a straight line, in every case, from the slope and intercept of which they deduced the parameters T_o and Γ respectively. This expression seemed to work quite will over a wide range of T more specifically in the lower temperature region. However it was not clear how the high temperature linewidth Γ_o value was chosen in every case. Apparently, in most of the cases Γ_o was chosen as the value of ΔH at T = 300 K, the highest temperature at which the ESR measurements were taken. Therefore the values of the parameter T_o obtained did not show a smooth and

consistent variation with respect to composition. In our ESR work, the measurements were extended up to T = 500 K, and ΔH showed a noticeable variation between 300 K and 500 K. Consequently, if one was to plot $\ln(\Delta H - \Gamma_o)$ vs T taking Γ_o as the value of ΔH at T = 500 K, in this case, one would obtain a linear variation in a certain range of temperatures, however the values of the parameters T_o and Γ obtained in this case would be totally different from those obtained with Γ_o = ΔH at T = 300 K. Knowing that for a given composition the values of these parameters (T_o and Γ) should be constant independent of the high temperature linewidth, convinced us further that our high temperature linewidth term $B(1 - \frac{\theta}{T})$ is the one to be used. Taking $F(T) = \Gamma \exp(-\frac{T}{T_o})$, the ΔH expression becomes:

$$\Delta H = \Gamma \exp(-\frac{T}{T_o}) + B(1 - \frac{\theta}{T}) \qquad (4.5)$$

As we mentioned before, by plotting the values of $T\Delta H$ vs T in the high temperature regions, the values of B and θ can be determined. Knowing the values of these parameters allowed us to calculate the paramagnetic contribution to the linewidth for the whole range of temperatures. However, it was found that at lower temperatures the $B(1 - \frac{\theta}{T})$ term appeared to overestimate the paramagnetic contribution so that in some cases the rapid increase in ΔH appeared to be dominated by the paramagnetic term rather than that due to the inhomogeneity effect. This can be attributed to the fact that the paramagnetic contribution is due to free Mn^{2+} spins all of which can be assumed to contribute at high temperatures. However, at lower temperatures where exchange effects become important, the increased correlation between the spins means that the effective number of free spins is reduced. To allow for

this, the B coefficient in the paramagnetic relation needs to be modified and so, has been written as $B\{1-\exp(-T/T_o)\}$. Hence this term is made to decrease at a rate compatible with the increase of the inhomogeneity effect which is caused by the increase in the exchange effect. Consequently the experimental values of ΔH vs T were fitted to the equation:

$$\Delta H = \Gamma \exp(\pm \frac{T}{T_o}) + B(1- \frac{\theta}{T}) / \{1 - \exp(- \frac{T}{T_o})\} \qquad (4.6)$$

Values of θ were taken from the magnetic susceptibility measurements and Γ, T_o and B were determined by a least squares fit to the values of ΔH from the maximum temperature used down to that at which the ESR line showed appreciable asymmetry. Below the temperature of asymmetry a value of ΔH to be used could not be clearly determined. The least squares calculations were carried out using an Apple II microcomputer programme written by Tom Donofrio, member of our research group. Fitting for all three parameters (T_o, Γ and B) would give a large uncertainty; to go around it, we fit over a large range of T_o values and fit for the two other parameters (B and Γ) and used the criterion of minimum standard deviation. This way seemed to give more consistent variation of the parameters as seen from Figs. 4.10 - 4.13.

In all cases, the fit to the experimental points was very good with a standard deviation of the order of 0.01 KG. Also, the values of B obtained with this method, were in good agreement with those obtained graphically (see above).

The variation of the parameters B, Γ and T_o with different composition variables for representative sections of the alloy phase diagram are shown in Figs. 4.10-4.13. It is seen that while the

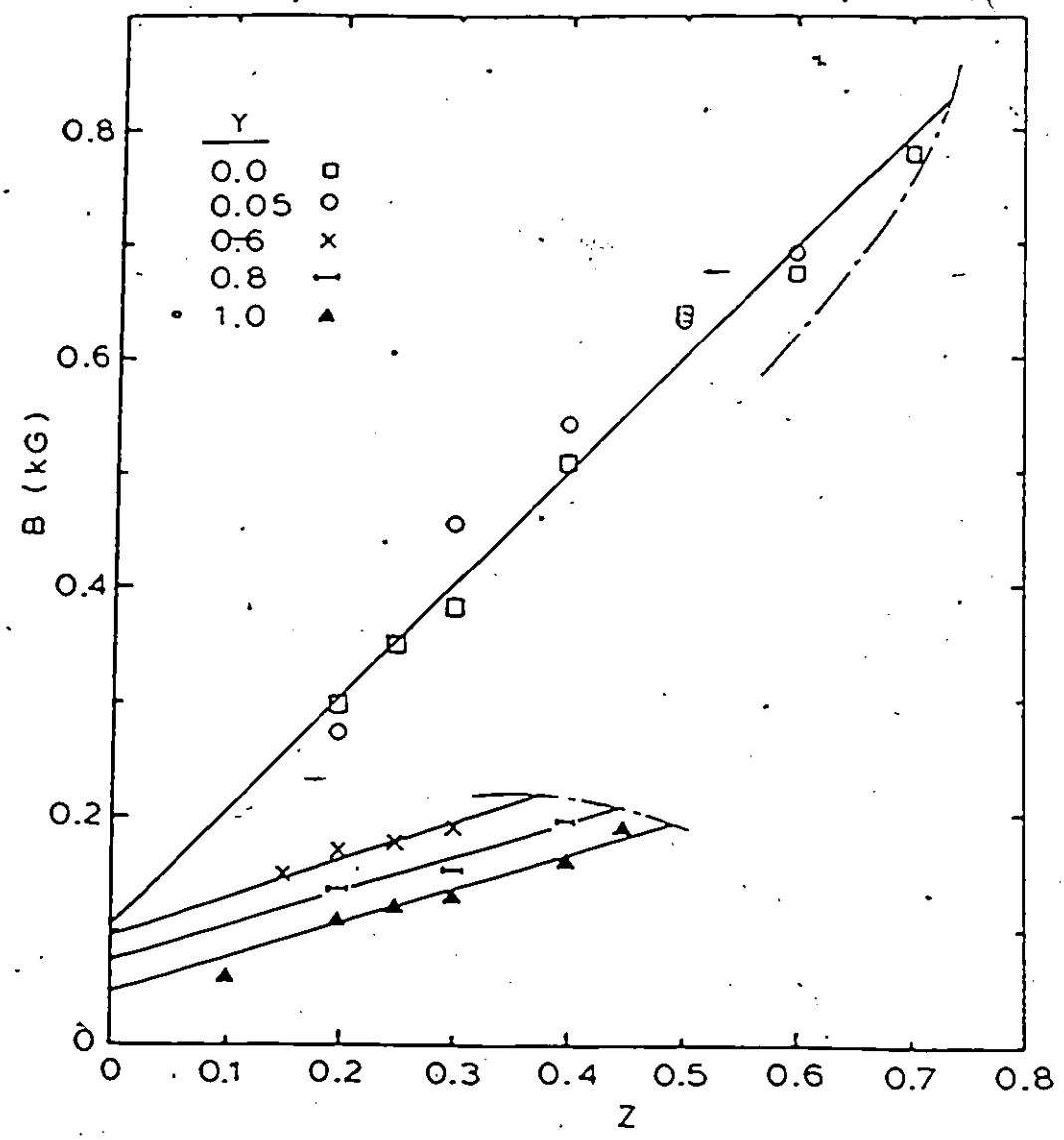

Fig. 4.10. Variation of the parameter B in equation 4.6 versus the Mn concentration z determined by fitting equation 4.6 to the ΔH vs. T curves for the indicated values of y. The dot-dashed lines indicate the boundaries of the single phase field.

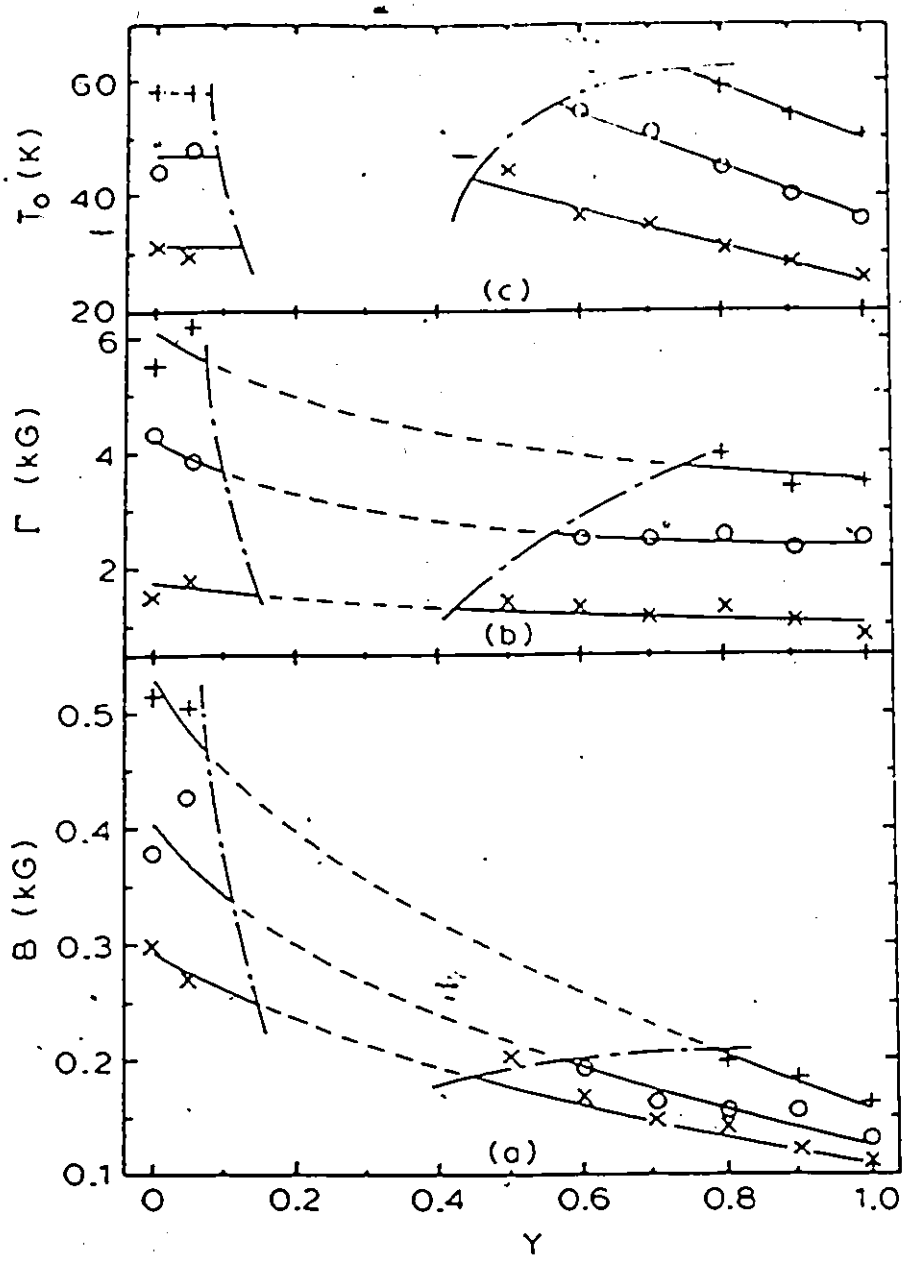

Fig. 4.11. Plots of the parameters B, Γ and T_o determined by fitting equation 4.6 to the ΔH vs. T curves for various Mn concentrations z as a function of alloy composition y. The dot-dashed lines indicate the boundaries of the single phase fields. (x) - 0.2 (O) - 0.3 and (+) - 0.4.

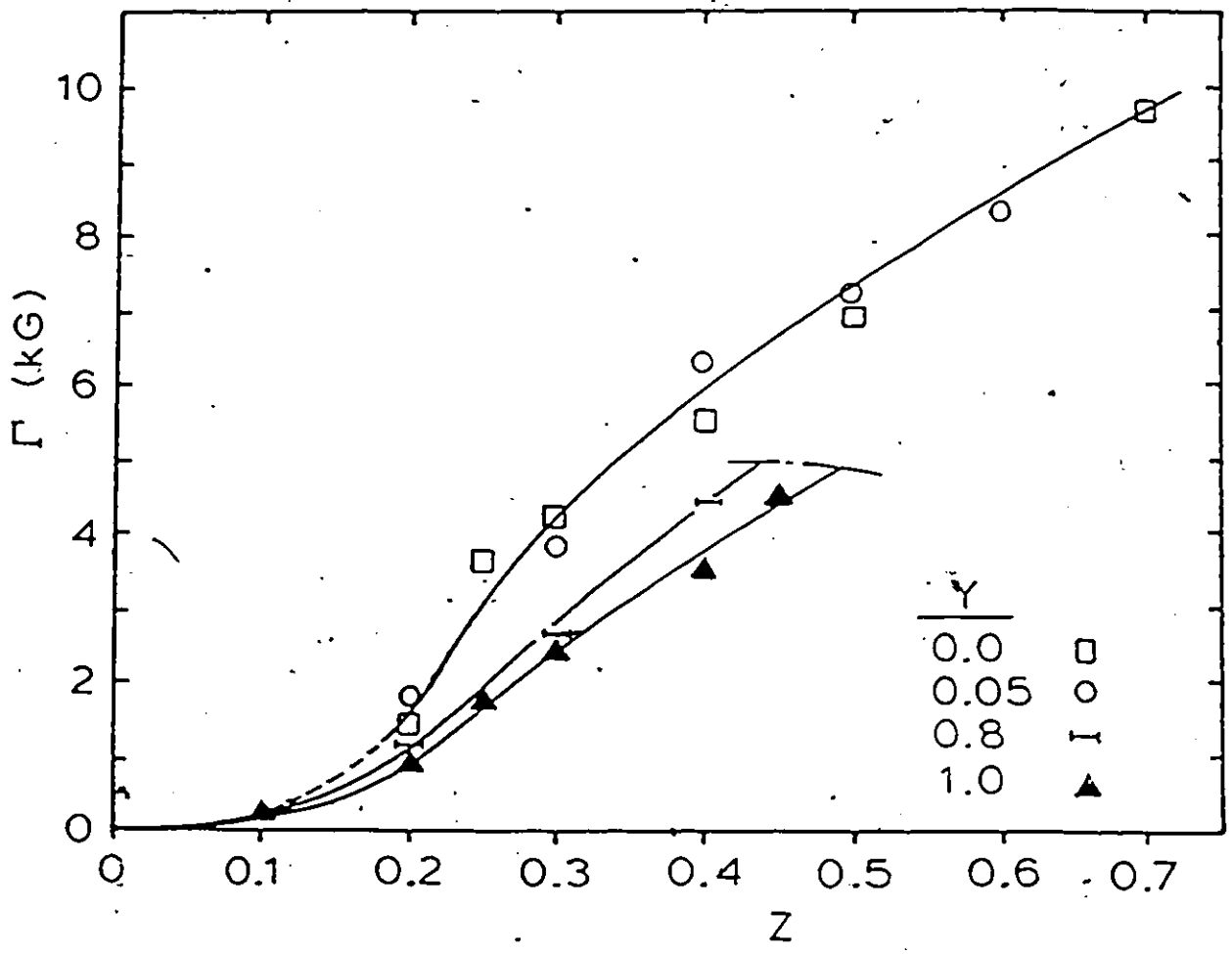

Fig. 4.12. Plot of the parameter Γ in equation 4.6 as a function of the manganese concentration z for various alloy compositions y determined by fitting equation 4.6 to the ΔH vs. T curves. The dot-dashed curve indicates a single phase field boundary.

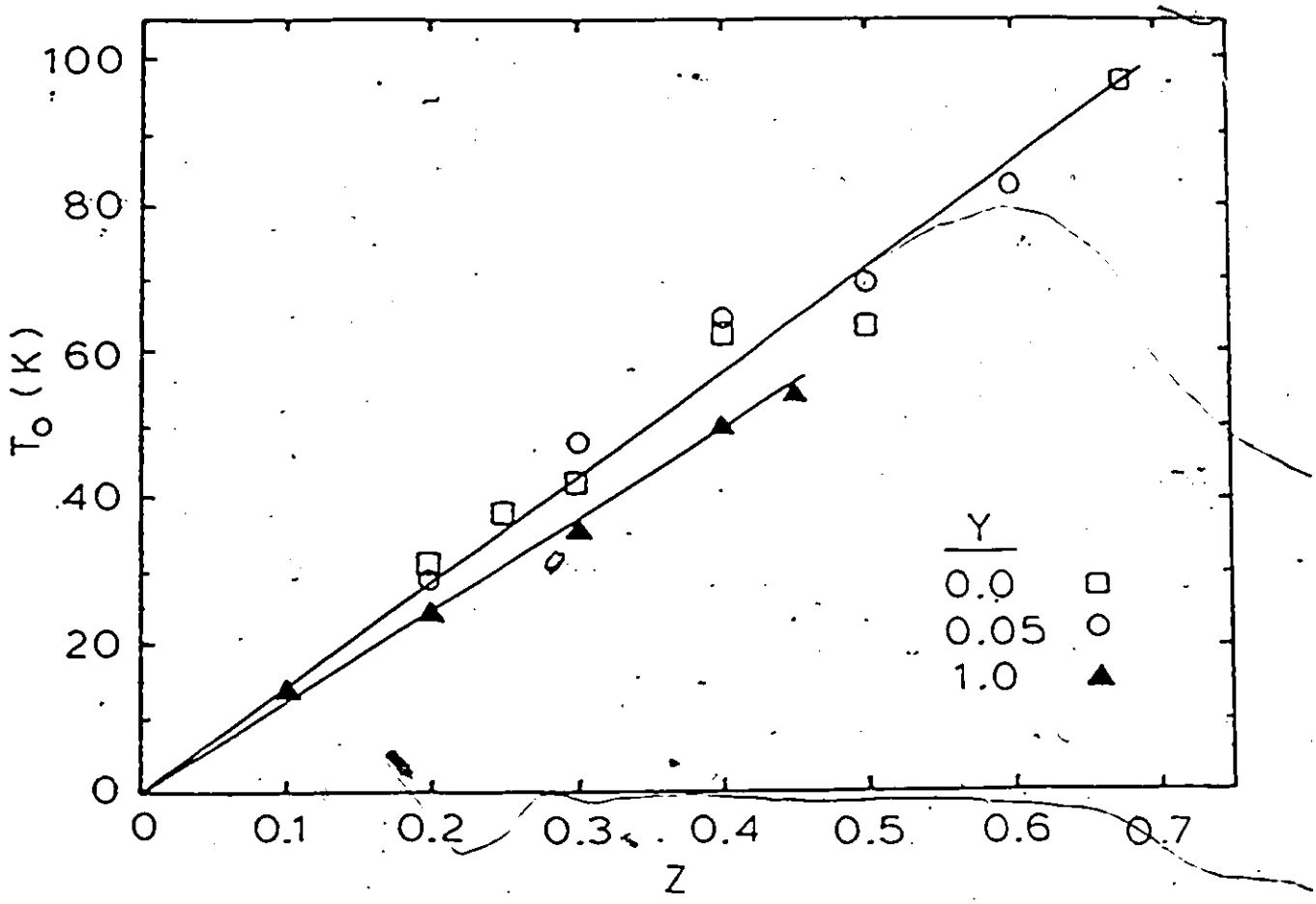

Fig. 4.13. Plot of the parameter T_o in equation 4.6 as a function of the manganese concentration z for various alloy compositions y determined by fitting equation 4.6 to the ΔH vs. T curves.

variations due to changes in y are smaller than those due to z, they are appreciably larger than the changes in the susceptibility parameters (see previous chapter). As is seen in Fig. 4.10, the paramagnetic parameter B shows a linear variation with z at constant y, a not unexpected result since the paramagnetic effect is the sum of the individual spin contributions. Extrapolation through the miscibility gap (Fig. 4.11(a)) appears to indicate a smooth but non-linear variation of B with y at constant z with no indication of any effect of crystal structure. For y = 1.0 the B vs z line extrapolates to a value of B = 40 gauss, while for y = 0 and 0.05 the corresponding value is about 115 gauss. For the quaternary alloys there again appears to be a smooth variation with y. These values are considerably smaller than linewidth for isolated Mn^{2+} impurities (~250 gauss [8,9]) and this indicates that there must be appreciable exchange narrowing of the ESR line at high temperatures and for the concentrations of manganese investigated here. The results in Fig. 4.11(a) indicates that this effect is greater for the selenide than for the telluride and varies smoothly as tellerium is substituted for selenium, again independent of crystal structure. It is tempting to interpret the greater effect of the exchange narrowing in the selenide than in the telluride, on the basis that in the selenide the spacing between two adjacent Mn^{2+} ions (i and j) is smaller than that in the telluride (and that from lattice parameter considerations), consequently the exchange parameter $|J(r_{ij})|$ and hence the exchange narrowing effect are expected to be greater in the selenide than in the telluride (note that in ch. 3 we calculated the nearest neighbor exchange parameter J_1/k for z = 0.05 in both cases

$Cd_{1-z}Mn_zSe$ and $Cd_{1-z}Mn_zTe$: $|J_1^{Se}/k| = 8.7$ K $> |J_1^{Te}/k| = 6.8$ K).

Fig. 4.12 shows the variation of with z for various values of y. These graphs show that for $z > 0.2$ the various lines tends to extrapolate to zero Γ at a value of z in the range 0.15 – 0.2. However, as in the case of T_g values (see chap. 3), for $z < 0.2$ non zero values of Γ are obcained and the curves appear to change slope in the vicinity of $z \sim 0.2$ and to extrapolate to zero at $z = 0$. The parameter Γ used here has similar form to the quantities Γ_{pp} of Webb et al [15] and $\Delta_2 + \Delta_1$ of Sayad er al [14] in their analysis of the results for $Cd_{1-z}Mn_zTe$ alloys. In those works the authors suggest that the variation with z falls into two separate parts, one with $z > 0.2$ and the other with $z < 0.2$. Again in Fig. 4.11(b), the variation of with y at constant z can be interpreted as a smooth curve showing no structure dependence.

The variation of the parameter T_o is shown in Figs. 4.11(c) and 4.13, Fig. 4.11(c) showing the variation of T_o with y for various values of z. It is of interest to note that while T_o shows a linear, and appreciable variation with y in the wurtzite β field, in this case these values do not extrapolate to the values obtained in the zinc blende α field. It appears that for T_o although there is a smooth variation of its value with y in a given structure, in this case the value of T_o is affected by the crystal structure also. In Fig. 4.13 the variation of T_o with z is shown, and for the sake of clarity only the case of $y = 0$, 0.05 and 1.0 are presented. It is seen that within the limits of experimental error, in each case the variation of T_o with z can be taken as linear and extrapolates to $T_o = 0$ at $z = 0$. T_o

represents the temperature at which appreciable clustering occurs in the materials. It is worth noting that with reference to the line shape, if T_A is the temperature at which significant asymmetry could be observed, it was found that to a good approximation $T_A \sim 1.5\ T_o$ for the hexagonal β phase and $T_A \sim 2.5\ T_o$ for the cubic phase.

With regard to the physical significance of these ESR parameters Sayad and Bhagat [14] have suggested that T_o is a measure of the potential barrier separating two neighbouring ground states of a disordered spin system, while Γ is determined by the variation in the magnetic environment of a Mn ion in the lattice. Γ essentially measures the width of the distribution of the local fields seen by the Mn ions, which is a measure of the degree of random behaviour in the alloy.

As a result, the variation of T_o with z shown in Fig. 4.13 indicates that the potential barrier between ground state increases linearly with Mn concentration z, and as might be expected, extrapolates to zero for z = 0. The variation of T_o with y for constant z (shown in Fig. 4.11(c)) shows that the barrier height increases as selenium is replaced by tellerium in the wurtzite phase field. This is consistent with the observations of Kremer and Furdyna [23]. Those authors have pointed out that at a constant temperature and a given value of z, for a given group II element, non-magnetic cation, the ESR linewidth becomes greater as the atomic number of the group VI element, anion, increases; but for a given anion, the line width decrease as the atomic number of the non-magnetic cation increases. A similar analysis of the results for $Cd_xZn_yMn_zTe$ and

$Cd_xZn_yMn_zSe$ carried out by T. Donofrio and S. Manhas (members of our research team) [24] shows in both cases that, at a constant z, T_o increases as cadmium is replaced by zinc, in the former case for zinc blende structure and in the latter case for wurtzite structure.

In recent work, Ching and Huber [25] have calculated the distribution of local fields as a function of occupied sites z. They show that the distribution width initially increases with z, but at a decreasing rate as z increases, then it is practically constant for $0.6 < z < 0.8$, and then falls for larger z and becomes zero when $z = 1$. One might therefore expect a similar behaviour for Γ. In the present work, Γ can be determined only for $z < 0.7$ in the cubic case and $z < 0.5$ in the hexagonal case. However the curvature of the Γ vs z lines in Fig. 4.12 is consistent with the form of variation predicted by Ching and Huber. If Γ is directly related to the random distribution of the Mn ions, then it should have a similar behaviour to the function $f(z) = z(1-z)$ which is the standard statical function for a random distribution. f(z) has its maximum at $z = 0.5$. However, since only the Mn^{2+} ions contribute to the effect, an extra factor z should be included i.e. $F(z) = z^2(1-z)$. This can also be concluded from the work of Huber and Ching, where the breadth of the calculated distributions of local fields for various values of z does not have its maximum at $z = 0.5$, but the maximum is rather somewhere between $z = 0.6$ and 0.8, which was found to be more consistent with the function $F(z) = z^2(1-z)$ than with f(z). In other words, f(z) has to be multiplied by z in order to meet the demand of the variation of local fields distribution width. This is not unreasonable, since the width

of the distribution, along with its height increases when the Mn concentration is increased.

In Fig. 4.14 we compare the data of Γ vs z for y = 0, 0.05 and y = 1, with the function $F'(z) = Cz^2(1-z)$. A value of 59 was found for C in case of y = 0 and 0.05 and of 39 in the case of y = 1. These values of C were obtained from a least squares fit of the experimental points which are seen to a good approximation to follow the variation of F'(z).

4.5 Conclusion

In this chapter we have presented a detailed investigation of the Electron Spin Resonance of the alloy system $(Cd_{1-z}Mn_z)(Te_{1-z}Se_z)$, in the two single-phase fields: zinc blende and wurtzite. The results obtained in this work, were found to be very useful in giving more insight into the magnetic behaviour of these SMSC's alloys, more specifically into their spins dynamic.

The evolution of the ESR line with the temperature was carefully investigated. In all cases the linewidth continuously increased while lowering the temperature, and the lineshape remained symmetric down to a certain temperature below which the line became asymmetrically broadened and then split into two parts in the low temperatures region. This was interpreted on the basis of a unaxial anisotropy of the g-value with $g_\perp > g_\parallel$. The linewidth variation with temperature was fitted to a phenomenological equation (4.6) based on the fact that the broadening of the ESR line beyond the paramagnetic region, is due to inhomogeneity effects arising from the random

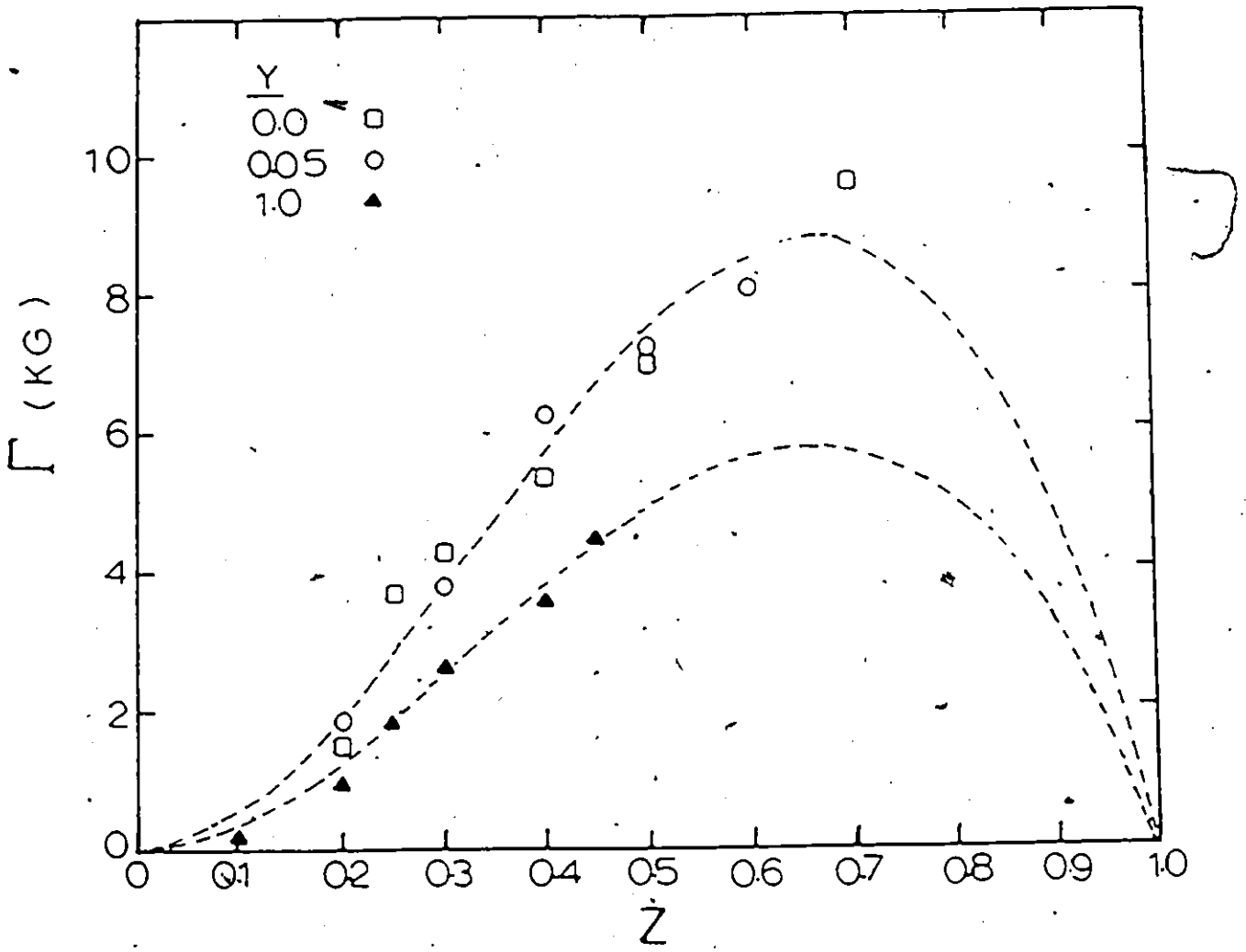

Fig. 4.14. Comparison of the experimental data of Γ vs z with the function $F'(z)=Cz^2(1-z)$. The latter is represented by the dashed lines ---- .

distribution of Mn ions. The values of the parameter B, T_o and Γ obtained from the fit showed consistent dependence on composition, with a rate of variation with z much greater than that with y. Consequently these values seem to be mainly determined by the Mn^{2+} concentration.

The parameter B represents the linewidth at the highest possible temperature. T_o represents the temperature at which appreciable correlation in the Mn clusters occurs, and hence is a measure of a potential barrier separating two neighbouring ground state of the disordered spin system. On the other hand Γ is determined by the variation in the magnetic environment of a Mn ion in the lattice, consequently it measures the width of the local fields distribution seen by the Mn ions, and hence is directly related to the degree of random behaviour in the alloy. The way these parameters vary with composition seems to agree fairly well with their physical interpretations

Finally, one can say that the results given above are consistent with the behaviour of a cluster-glass material. At high temperatures the Mn^{2+} spins interact weakly in a normal paramagnetic fashion giving the paramagnetic contribution to the ESR linewidth. As the temperature is lowered the spins begin to show greater correlation in clusters, causing the inhomogeneous broadening in the linewidth, represented by the exponential term in equation 4.6. As the temperature is further reduced, the correlation effect increases and extends giving rise to larger clusters of correlated spins, but the intensity of the ESR line becomes so small that it can no longer be observed, which limits any further investigations of the ESR line.

REFERENCES

1. A.H. Morrish, "The physical principal of magnetism", Robert E. Krieger publishing company. p. 28.
2. H. watanabe, Progress of Theoretical Physics, vol. 18, no. 4, p. 405 (1957).
3. J.R. Gabriel, d.F. Johnston and M.J.D. Powell, Proc. Royal Soc. London, 264 A, p. 503 (1961).
4. J.E. Wertzand and J.R. Bolton, "Electron Spin Resonance, Elementary Theory and practical applications", McGraw-Hill, p. 303-308 (1972).
5. Abragam and Bleany, "Electron Paramagnetic Resonance of Transition Ions", Clarendon Press-Oxford, p. 142-148, 438-442, 467-470 (1970).
6. J. Schneider, S.R. Sircar and A. Rauber, Z. Naturforsch. 18A, 980 (1963).
7. O. Matumura, J. Phys. Soc. Japan vol 14, p. 108 (1959).
8. C. Kikuchi and J. Lambe, Phys. Rev. 119, 1256 (1960).
9. R.S. Title, Phys. Rev. 130, 17 (1963).
10. S.B. Oseroff, Phys. Rev. 25B, 6584 (1982).
11. S. Oseroff, R. Calvo and W. Giriat, J. Appl. Phys. vol. 50, 7738 (1979).
12. S. Oseroff, R. Calvo and W. Giriat and Z. Fisk, Solid State Comm., vol. 35, p. 539 (1980).
13. S.B. Oseroff, and R. Calvo, Z. Fisk and F. Acker, Phys. Lett. vol. 80A, p. 311 (1980).

14. H.A. Sayad and S.M. Bhagat, Phys. Rev. 31B, 591 (1985).

15. D.J. Webb and S.M. Bhagat, J.K. Furdyna, J. Appl. Phys. 55, 2310 (1984).

16. J.W. Searl, R.C. Smith and S.J. Wyard, Proc. Phys. Soc. (GB), vol. 78, Pt 6 (i), 1174-6 (1961).

17. J.W. Searl, K.C. Smith and S.J. Wyard, Bulletin Ampères Fasc. special, 9th year, 236 (1960).

18. J.W. Searl, R.C. Smith and S.J. Wyard, Proc. Phys. Soc., 74, 491 (1959).

19. D.L. Huber, Phys. Rev. B6, 3180 (1972).

20. V. Jaccarino and E. Dormann, Phys. Lett. 48A, 81 (1974).

21. H.E. Stanley, "Introduction to Phase Transition and Critical Phenomena" (Clarendon Press, Oxford) p. 85 (1971).

22. J.F.K. Furdyna and R.E. Kremer, J. Mag. Mag. Mat. 40, 185 (1983).

23. R.E. Kremer and J.K. Furdyna, Phys. Rev. B31, 1 (1985).

24. To be published.

25. W.Y. Ching and D.L. Huber, Phys. Rev. B26, 6164 (1982).

Chapter 5

Optical Energy Gap Measurements

5.1 Introduction

One of the most important physical constants which characterize a semiconductor is its energy gap, Eg, also called the band gap. Eg represents the difference in energy between the lowest point of the conduction band and the highest point of the valence band. The determination of the energy gap is fundamental in investigating the semiconducting properties of any semiconductor material.

As indicated earlier, our alloy system $[Cd_{1-z}Mn_z][Te_{1-y}Se_y]$ belongs to the new group of semiconducting materials known as semimagnetic semiconductors (SMSC's), the major interest in which started with the observation of the giant enhancement of magneto-optical effects that these materials (SMSC's) exhibit [1,2]. We note that in zero external magnetic field (H = 0) typical SMSC's such as $Hg_{1-z}Mn_zTe$, $Cd_{1-z}Mn_zTe$ etc. behave in a similar fashion to their normal (non-magnetic) counterparts such as $Hg_{1-z}Cd_zTe$, $Cd_{1-z}Zn_zTe$ etc. in which the magnetic element (Mn) is replaced by a nonmagnetic one (Cd or Zn). In both cases (SMSC's and their normal counterparts), the conduction and valence band structure depend on the composition z; consequently by changing z the band structure can be modified i.e. forbidden energy gap E_g, effective masses etc. [1,2].

In this work, energy gap measurements were carried out on samples in the zinc blende and wurtzite single-phase fields of our

diagram (see fig. 2.6). The energy bands structures of the crystals with both the zinc blende (such as CdTe) and wurtzite (such as CdSe) symmetry are fairly well known throughout the Brouillon zone [3]. In both structures, the minimum of the conduction band and the maximum of the valence band are believed to occur at the Γ-point, the center of the Brouillon zone ($\vec{K} = 0$). On the basis of a theoretical analysis carried out by Birman [4], the band structure of a wurtzite crystal at any point in K-space along the hexagonal c-axis (and in particular at the Γ-point, $\vec{K} = 0$) can be regarded as obtained from a zinc blende crystal with a slight perturbing uniaxial crystal-field V' applied along the [111] direction. The perturbation V' can be written as $V' = V_{Wur} - V_{ZB}$; its magnitude depends on (a) difference in bond type (e.g. effective charge) in the two structures, and (b) departure of the wurtzite structure from ideality (the ideal wurtzite has $\frac{c}{a} = \sqrt{8/3}$). Fig. 5.1 shows the band structure and selection rules for zinc blende and wurtzite structures at the Γ-point ($\vec{K} = 0$) [5.7]. This applies for the two compounds CdTe (ZB) and CdSe (Wur). In both cases the top of the valence band at the Γ-point is a three-fold p-type state, the bottom of the conduction band also at the Γ-point, is an s-type state.

As it is seen in Fig. 5.1 in the zinc blende case, the spin-orbit interaction splits the Γ_4' three fold degenerate level of the valence band into the two-fold degenerate level Γ_8 and the one fold Γ_7, usually known as the spin-orbit split-off. (Note that the spin double degeneracy of each state is not taken into account). The Γ_1 state of the conduction band becomes Γ_6. In the case of the wurtzite, the crystal-field V' splits Γ_4' into a two-fold degenerate Γ_5 level and a

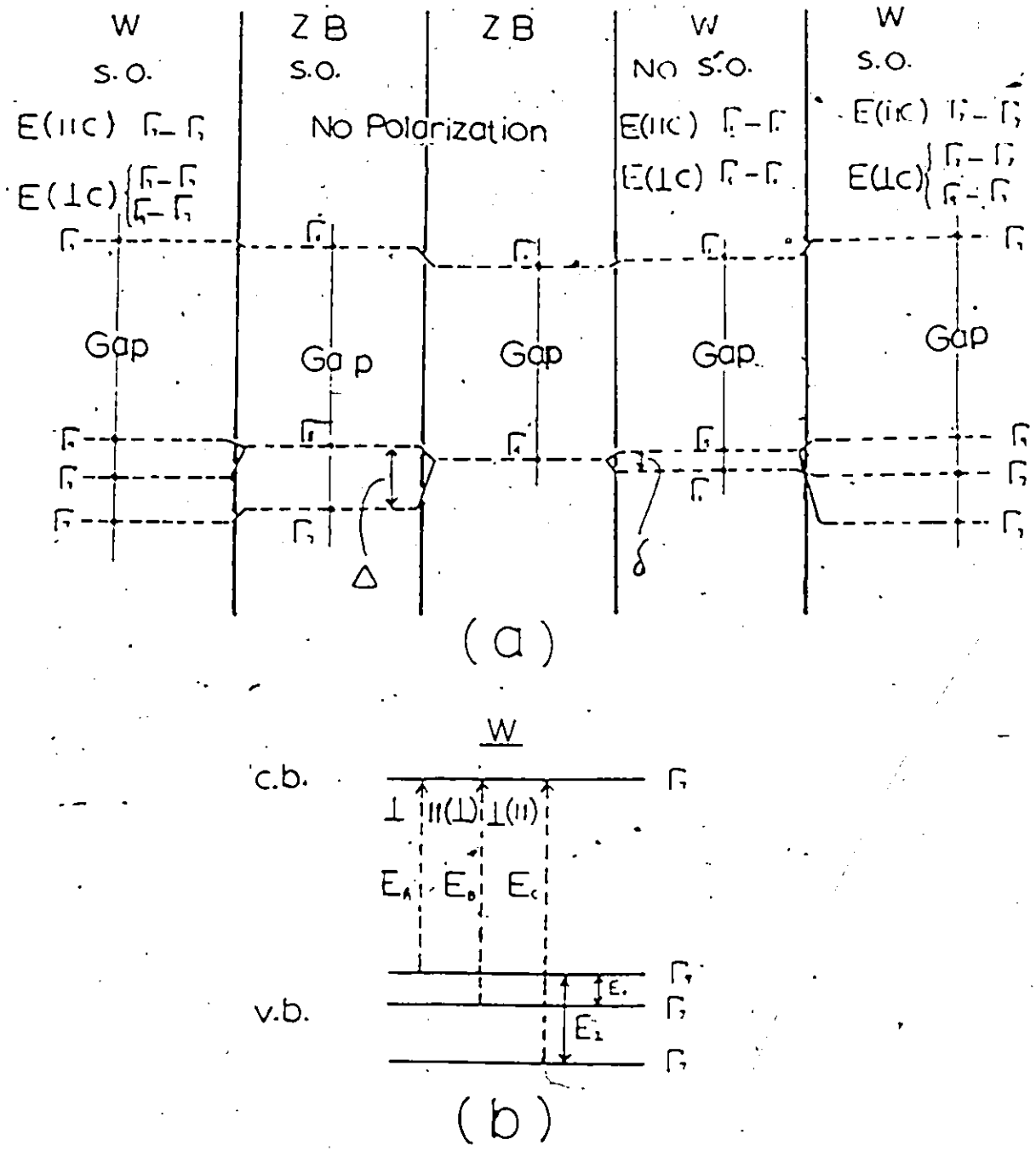

Fig. 5.1. Band structure and selection rules at K = (000) for zinc blende (ZB) and wurtzite structures (W). Crystal field splitting (δ) and spin-orbit splitting (Δ) are indicated schematically. Transitions which are allowed for various polarizations of photon electric vector with respect to cystal "c" axis are indicated.

one-fold Γ_1; then the spin-orbit splits Γ_5 into two one-fold degenerate states Γ_9 and Γ_7, also the Γ_1 of the valence band, as well as that of the conduction band, both become Γ_7.

The simplest method of measuring the band gap of a sample is to measure its absorption spectrum. Limitations in this technique usually arise from the inability of some materials to transmit enough light to be measurable at energies below the band gap, because of background absorption even when the sample is polished down to an extremely small thickness. This is not a problem in the present case, because our material shows small absorption to light with energy below the gap even with samples up to one millimeter in thickness. However, the usefulness of absorption is severely limited by another factor, when this energy gap becomes larger than ~2 eV, its observation becomes masked by some kind of internal manganese transition, the exact nature of which is not yet fully known [8,9]. This effect has already been observed in the $Cd_{1-z}Mn_zTe$ system [9]. Since quite a few samples of our system were expected to have energy gap > 2 eV, a different technique was needed. We used the wave length modulated reflectance technique to determine the gaps.

5.2 Wavelength Modulated Reflectance

The dielectric function $\varepsilon(\omega,\vec{K})$ depends sensitively on the electronic band structure of a crystal, therefore, it describes the response of the crystal to an electromagnetic field. Since both the absorption and reflection spectra are related to ε [10,11], then they may be used as tools for band structure determination.

The condition for absorption of photon $\hbar\omega$ in a

semiconductor:

$$E_c(\vec{K}) - E_v(\vec{K}) > \hbar\omega \qquad (5.1)$$

where E_c and E_v are the energies of the empty conduction band and filled valence band respectively. At the threshold of absorption where only the equality holds, the reflectance peaks. In fact, the reflectance peaks at all points in the Brouillon zone for which the conduction band and the valence band are parallel; that is where

$$\nabla_k[E_c(\vec{K}) - E_v(\vec{K})] = 0 \qquad (5.2)$$

and $$E_c(\vec{K}) - E_v(\vec{K}) = \hbar\omega$$

(for more details see Ref. 11)

In order to determine experimentally the reflectance R of a sample as a function of the incident photon energy, the intensity of the reflected light I is measured. These two quantities are related by the following: $I = RI_o$, where I_o is the intensity of the incident light. However, the peaks of the reflectance spectra are not very strong in most cases, which may make an accurate determination of the transitions energies difficult. One way to go around this difficulty is to measure the derivative of the reflectance with respect to wavelength. This make the transition signal much more distinct.

In wavelength modulation spectroscopy, the derivative of I with respect at λ is measured. Taking the derivative of the equation $I = RI_o$; we will obtain:

$$\frac{dI}{d\lambda} = R\frac{dI_o}{d\lambda} + I_o\frac{dR}{d\lambda} \qquad (5.3)$$

the quantity to be investigated is $\frac{dR}{d\lambda}$. The quantity which can be measured, however, is $\frac{dI}{d\lambda}$. This can present a problem in that the term $\frac{dI_o}{d\lambda}$ may be much stronger than the $\frac{dR}{d\lambda}$ term. In addition, the two terms

are also multiplied by R and I_o respectively. However these two quantities (R and I_o) can, in most cases, be assumed to be constant in comparison to their derivative over a limited wavelength range. $\frac{dI_o}{d\lambda}$ depends on the exact nature of the incident light. Ideally, I_o should be flat in term of its response to the wavelength change; but in practice, this is not quite the case. I_o depends on the characteristics of the light source and the diffraction grating used in the monochromator, as well as (to a lesser degree) any mirrors used to focus the light in various parts of the system. In fact, any significant change in the response of these elements can gives enormous derivative curves that may virtually wipe out any trace of the wanted signal in that particular region of the spectrum.

The usual way to get around this is to split the incident light into two; one of the beams will be reflected off the sample as usual, while the other is measured directly. The latter signal should contain only the $\frac{dI_o}{d\lambda}$ term, while the former would contain both. The two signals are then subtracted using some kind feedback arrangement in order to keep the two $\frac{dI_o}{d\lambda}$ terms at the same amplitudes. However, in order to be able to accomplish this, the two detectors used must have identical responses; otherwise, the two $\frac{dI_o}{d\lambda}$ terms will not cancel out after the subtraction.

In the case of $(Cd_{1-z}Mn_z)(Te_{1-y}Se_y)$, the transition signal was strong enough to be seen in most regions of the spectrum without any subtraction, except in and around the giant peaks mentioned earlier. For these cases, a manual subtraction routine was often successful in extracting the energy gap signal. This routine consisted

of replacing the sample with a mirror in order to measure $\frac{dI_o}{d\lambda}$ independently of $\frac{dR}{d\lambda}$. Then the relative amplitude of the sample and mirror signals were adjusted so that at wavelengths well away from the peak the $\frac{dR}{d\lambda}$ signal was zero.

5.3 Apparatus Used and Experimental Procedures

5.3.1 Wavelength Modulated Reflectance

A schematic diagram of the experimental set up is shown in Fig. 5.2. The light from the source, which can be a tungstun filament bulb or a quartz iodin lamp, is focused on a slit with an aperture set at 1.0 mm. From there, the light is reflected onto a grating and then directed onto a mirror which can be contineously oscillated through a small angle. This where the wavelength modulation takes place.

A small motor controls the oscillation frequency of the mirror. With the frequency of oscillation set to zero, the light reflecting off the oscillating mirror is directed onto the the exit slit. Since the light has been split into its different components by the grating, there is a spatial distribution in wavelength along the wall around the exit slit. So only the wavelength that happens to be directly incident on the slit is permitted through. The angle of the diffraction grating determines what this wavelength is. With the oscillating motor on, the mirror vibrates back and forth, which in turn shifts the wavelength of the admitted light by a small amount $\Delta\lambda$, back and forth. The frequency of the oscillator was set to be between 22 and 28 Hz, to avoid any interference from subharmonics of sixty cycle line noise.

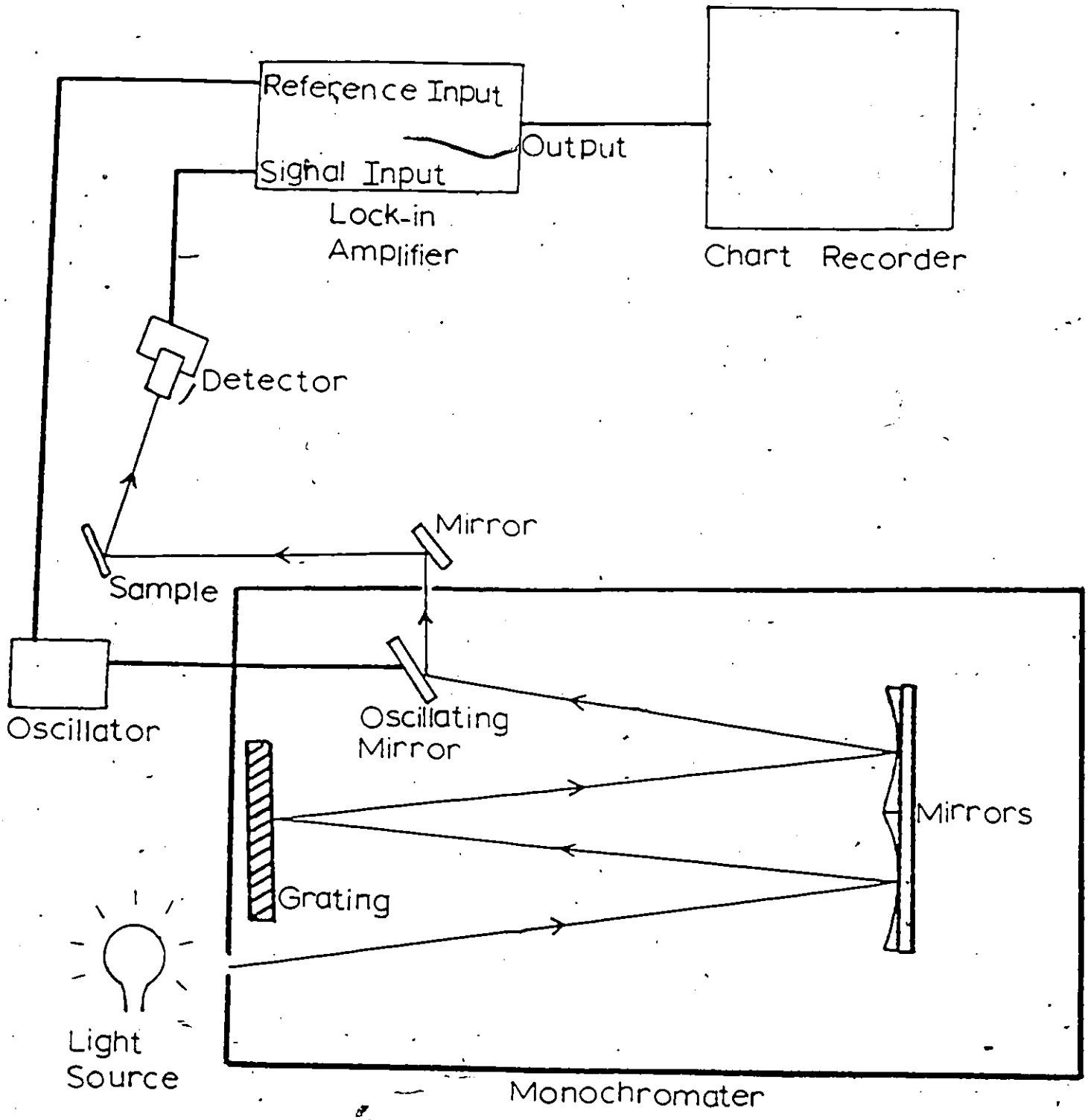

Fig. 5.2. Wavelength Modulated Reflectance Apparatus.

The width of the exit slit was set at 1.0 mm just as the entrance slit was, although it was found that small deviations from these values did not affect the result to any great extent. The modulated "monochromatic" light is then focused onto the sample with the reflected light measured by a photomultiplier (Fairchild 6911).

The photomultiplier signal was fed into a lock-in amplifier which was locked on to the oscillation frequency of the mirror. In this way, only the modulated signal was read by the lock-in. The output signal was in turn fed into an X-Y recorder or, a signal analyser which essentially served the same purpose as the chart recorder. For all the measurements carried out at room temperature, the energy gap signal could be observed, but it would have been difficult to determine the energy gap directly from this. The procedure used to do so, starts with measuring the sample signal over a certain wavelength range and storing it on the signal analyser. The sample in the monochromator is then replaced by a mirror. The amplitude of the new signal is then adjusted so that the levels of the two signals (the sample signal and the mirror signal) are as similar as possible at a wavelength far away from any transition. Since the reflectance of the mirror is not very dependent on the wavelength, this procedure is effectively measuring a signal which is proportional to the derivative of the incident light $dI_o/d\lambda$; so this signal is measured over the same range as the sample signal and simultaneously subtracted from it, using the signal analyser. This way most of the $\frac{dI_o}{d\lambda}$ term is eliminated and the resultant signal mostly contains the $\frac{dR}{d\lambda}$ term.

5.3.2 Cryogenic Apparatus

For measurements below room temperature, a CTI-CRYOGENICS model 21SC CRYODYNE CRYOCOOLER was used. A schematic diagram of the entire system is presented in Fig. 5.3. The system employs Joule-Thompson expansion of He gas to cool down to just below 10 K. The compressor is connected to the cold head by He supply and return lines. Together, they compress and expand the gas and so provide cooling for the cold station below the cold head. The cold station (Fig. 5.4a) is divided into two stations where two different temperatures can be maintained. For the present set of measurements, the second stage cold station was used in order to reach the lowest possible temperature.

The temperature was controlled using a LAKE SHORE CRYOTRONICS model drc-80c digital cryogenic thermometer controller. This includes a 0-10 watt and 0-25 watt heater and a calibrated DT-8500 series silicon thermometer. The accuracy of the sensor is stated to be within 0.5 K at 4 K and 77 K, and 1.0 K at 273 K. The latter was mounted on the second stage cold station.

The sample holder (Fig. 5.4b) was firmly attached to the bottom of the second stage. It was made of copper and consisted of two pieces. The main part had a large surface contact with the cold station. The samples was mounted on a removable copper plate which is attached to the main part of the holder by three brass screws. These screws, being made of a different material, had to be tightened strongly in order to prevent any loosening of the plate at low temperature. In order to facilitate mounting and removing samples, a

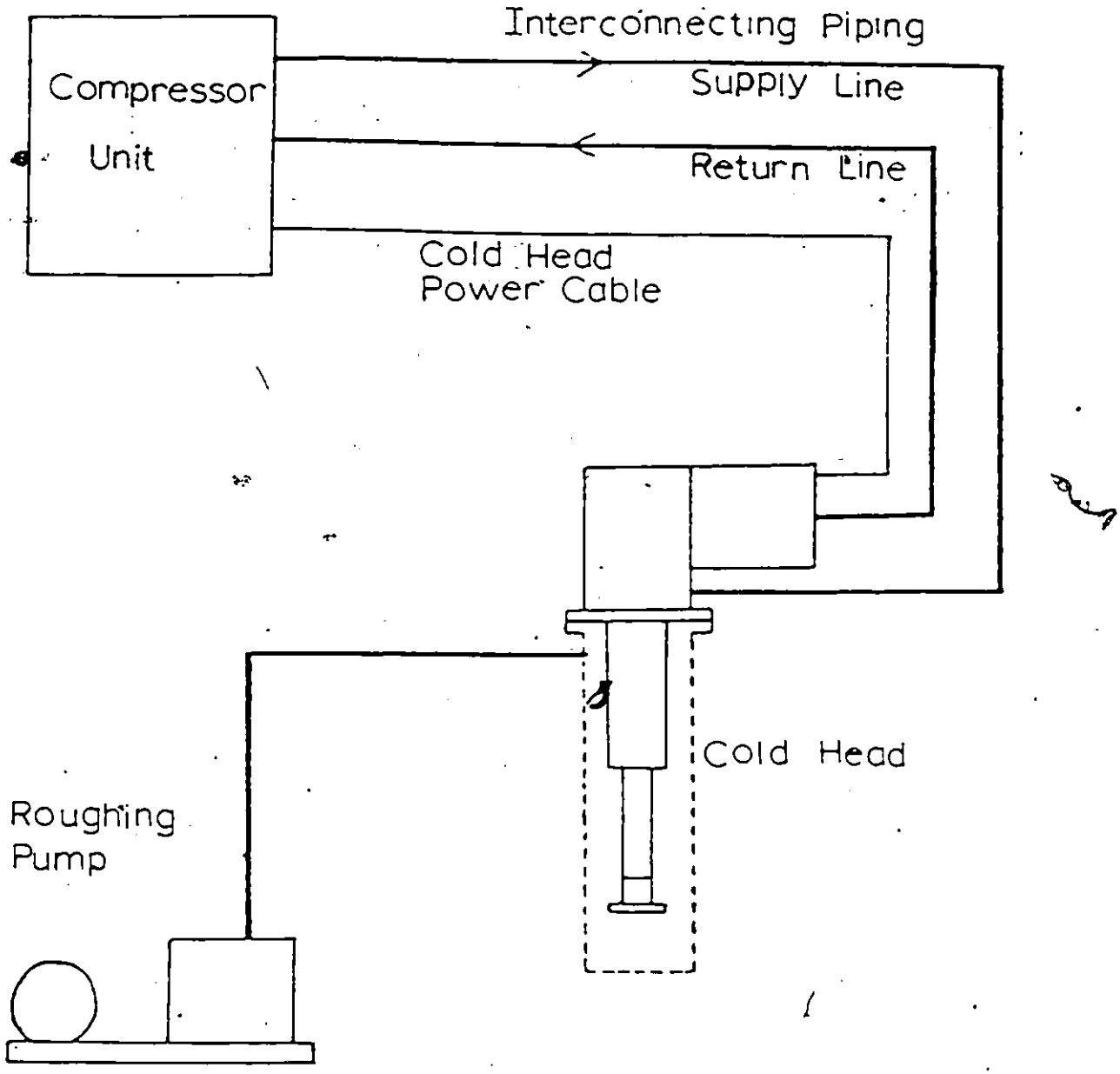

Fig. 5.3. Schematic of the cryogenic apparatus for measuring the energy gap at low temperatures.

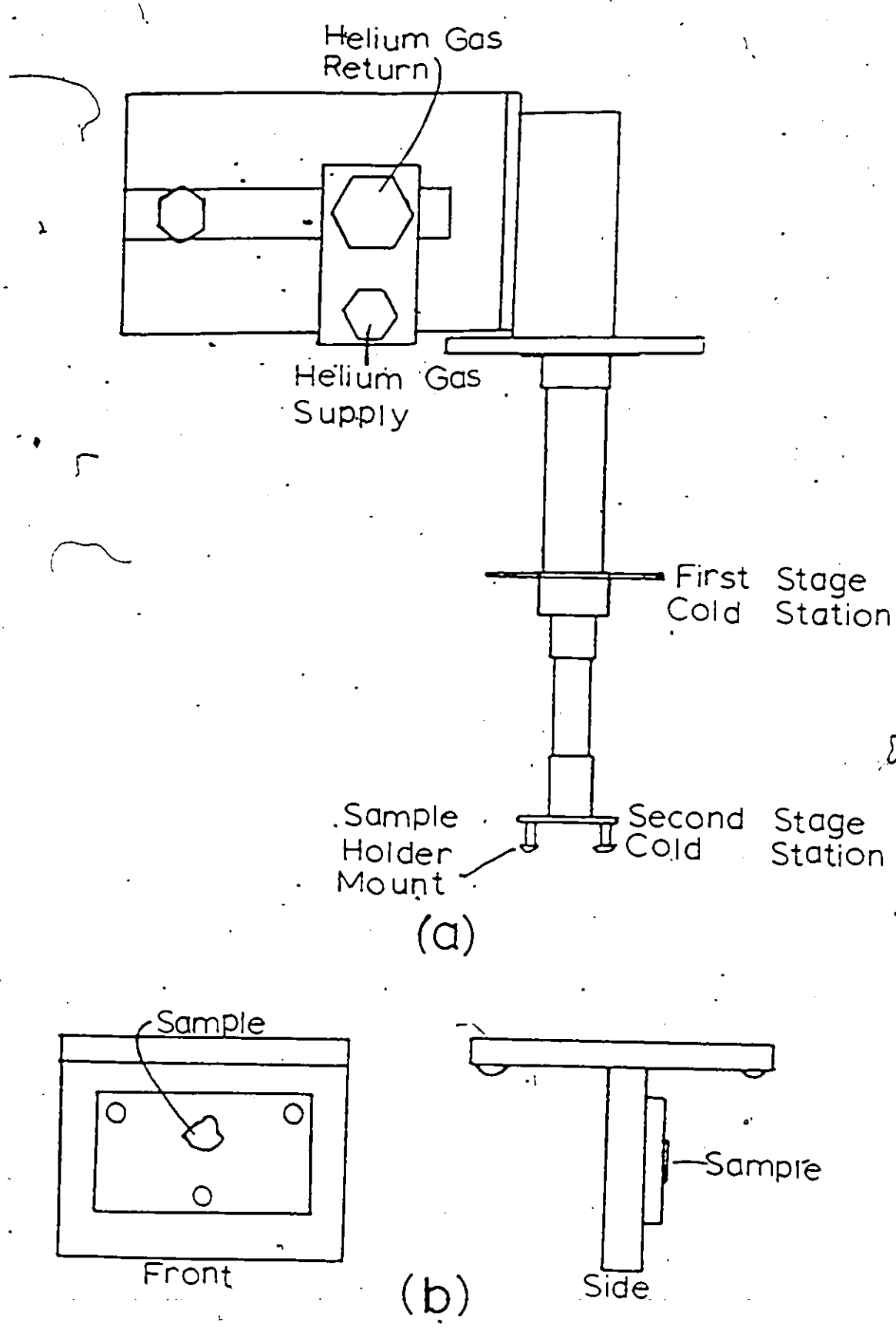

Fig. 5.4. (a) Cold station of the cryostat. (b) Sample holder.

heat sink grease, which has a high thermal conductivity, was used to attach the sample to the copper plate.

The entire cold station was enclosed in a vacuum chamber that was pumped out and maintained at a pressure of 10^{-4} mm of Hg during operation to provide thermal isolation. The chamber possessed four windows for optical measurements of the enclosed sample.

5.3.3 Sample Preparation

The optical measurements were performed on suitable pieces of each sample. These pieces were obtained by slicing off a portion between two and three millimeter in thickness. One face of the piece was hand polished using 1.0 micron alumina powder, in order to remove any shallow damage in the crystal as well as to make the face as flat as possible. The next step was to etch the polished face in a 3% solution of bromine in 99% pure methanol. The etching process involved gently rubbing the face of the sample over the surface of an absorbant paper saturated with the solution. Two to three minutes of etching were needed to obtain a good reflecting surface on the face.

5.4 Results of the Energy Gap Measurements

Energy gap measurements were carried out, at room temperature, on all the samples of the zinc blende and wurtzite single-phase fields of our diagram. Temperature dependent energy gap measurements were carried out on samples of the $Cd_{1-z}Mn_zSe$ edge with the wurtzite structure.

An example of the type of signal obtained at room temperature

for the derivative curve corresponding to a transition through the band gap is shown in Fig. 5.5. This figure shows the "raw" signal (sample signal), as well as the mirror signal and the resultant subtracted signal, from which the energy gap is evaluated. It was found for most of the cases, it was necessary to subtract the $\frac{dI_o}{d\lambda}$ term in order to be able to measure the signal. However as we shall see later, this subtraction proved to be unnecessary for the measurements performed below room temperature.

The method used to evaluate the energy gap from the signal is illustrated also in Fig. 5.5. It simply consists of measuring the energy values at the positive and negative peaks of the derivative curve, and then calculating the value of the energy at the midpoint between them. This midpoint is taken as the energy gap.

Using this arbitrary method in all cases, would systematically reproduce the same relative error in each determination. Furthermore the width between the maximum and the minimum of the signal shown in Fig. 5.5 (which is a typical curve) corresponds to a difference in energy of ~0.05 eV. This is quite small compared to the value of 2.13 eV for the energy gap obtained at the midpoint. Consequently, any systematic error in our method for pinpointing the gap would have to be even smaller than 0.05 eV. An uncertainty of 3 nm for determining where the energy gap is, gives an error of ~0.01 eV in the energy gap. This figure is smaller than the standard deviation obtained when the room temperature energy gap results were fitted to a polynomial equation as we shall see later.

Using the method described above, the energy gap E_g values

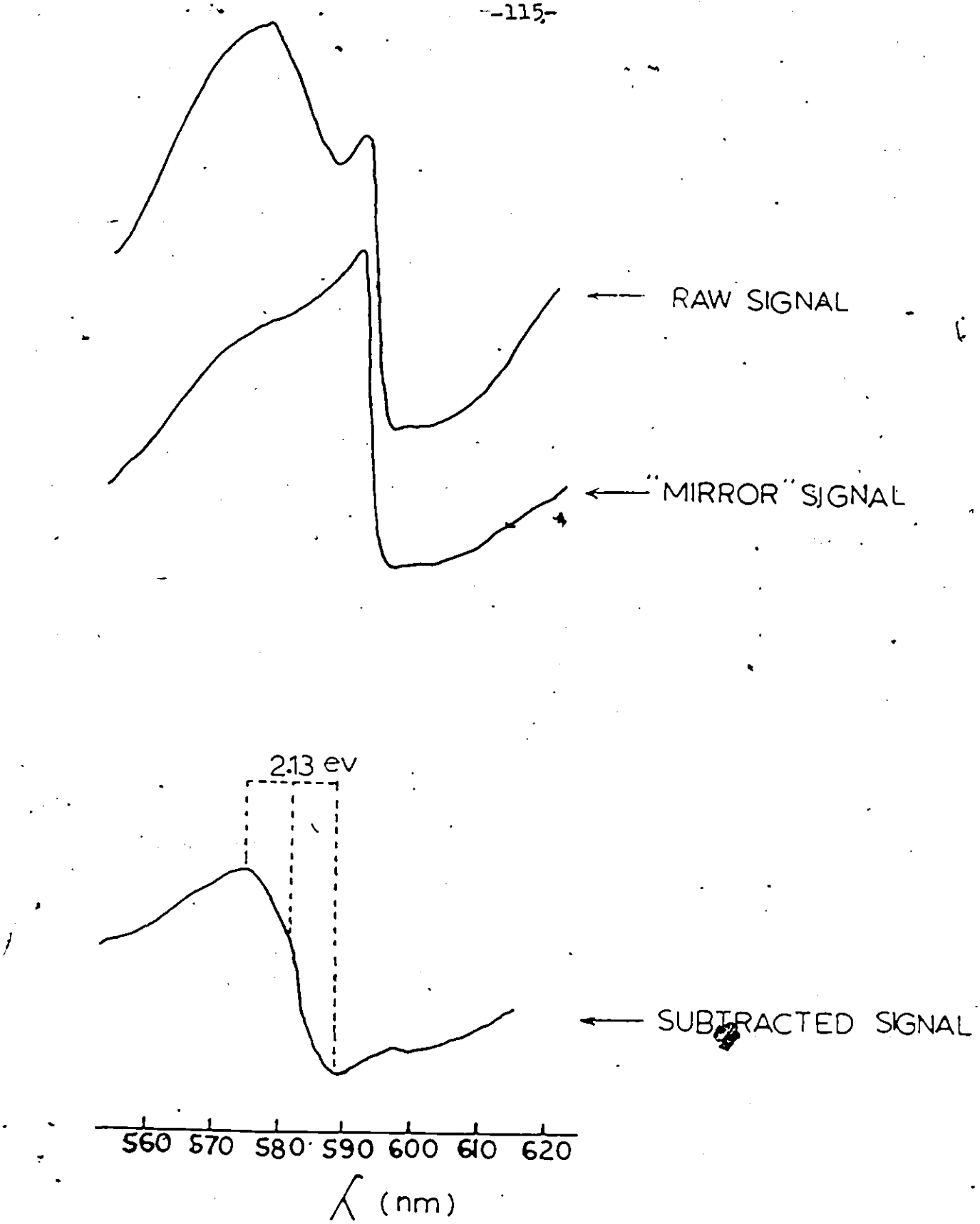

Fig. 5.5. Extraction of energy gap from the derivative signal.

were determined at room temperature, for the wurtzite and zinc blende samples of our alloy system $(Cd_{1-z}Mn_z)(Te_{1-y}Se_y)$. The E_g values were plotted as a function of composition. Fig. 5.6 illustrates the variation of E_g, for lines of constant z(Mn concentration), as a function of y(selenium concentration); on the other hand Fig. 5.7 shows E_g variation, for lines of constant y, as a function of z. While the latter shows a linear behaviour for the E_g dependence on z, the former exhibits a parabolic-like curvature for the E_g dependence on y.

Turning to the temperature dependent energy gap measurements, the energy gap was determined between 300 K and 10 K for alloys along the $Cd_{1-z}Mn_zSe$ edge. Typical wavelength modulated reflectance (WMR) spectra for $Cd_{0.8}Mn_{0.2}Se$ at various temperatures are shown in Fig. 5.8; also the $\frac{dR}{d\lambda}$ curves as a function of wavelength, for CdSe are shown in Fig. 5.9, for three different temperatures. At room temperature, the WMR structure due to the fundamental transition ($E_A = \Gamma_9-\Gamma_7$; also see Fig. 5.1 for the meaning of E_A, E_B,E_C,E_1 and E_2) was small and broad. As a result, the transition from the crystal-field split-valence band to the conduction band (E_B = vb upper Γ_7-cb Γ_7) was not resolved. As the temperature was lowered, the signal became bigger and narrower, with further lowering of T, the signal became sharper and the WMR line finally split into two, so that the E_B transition was resolved. But the E_B transition line was always smaller than that of E_A. The transition from the spin-orbit-split valence band to the conduction band (E_C = vb lower Γ_7 - cb Γ_7) was observed only in the case of CdSe (Fig. 5.9). We were not able to observe this transition for the other alloys, probably because we were dealing with polycrystalline materials

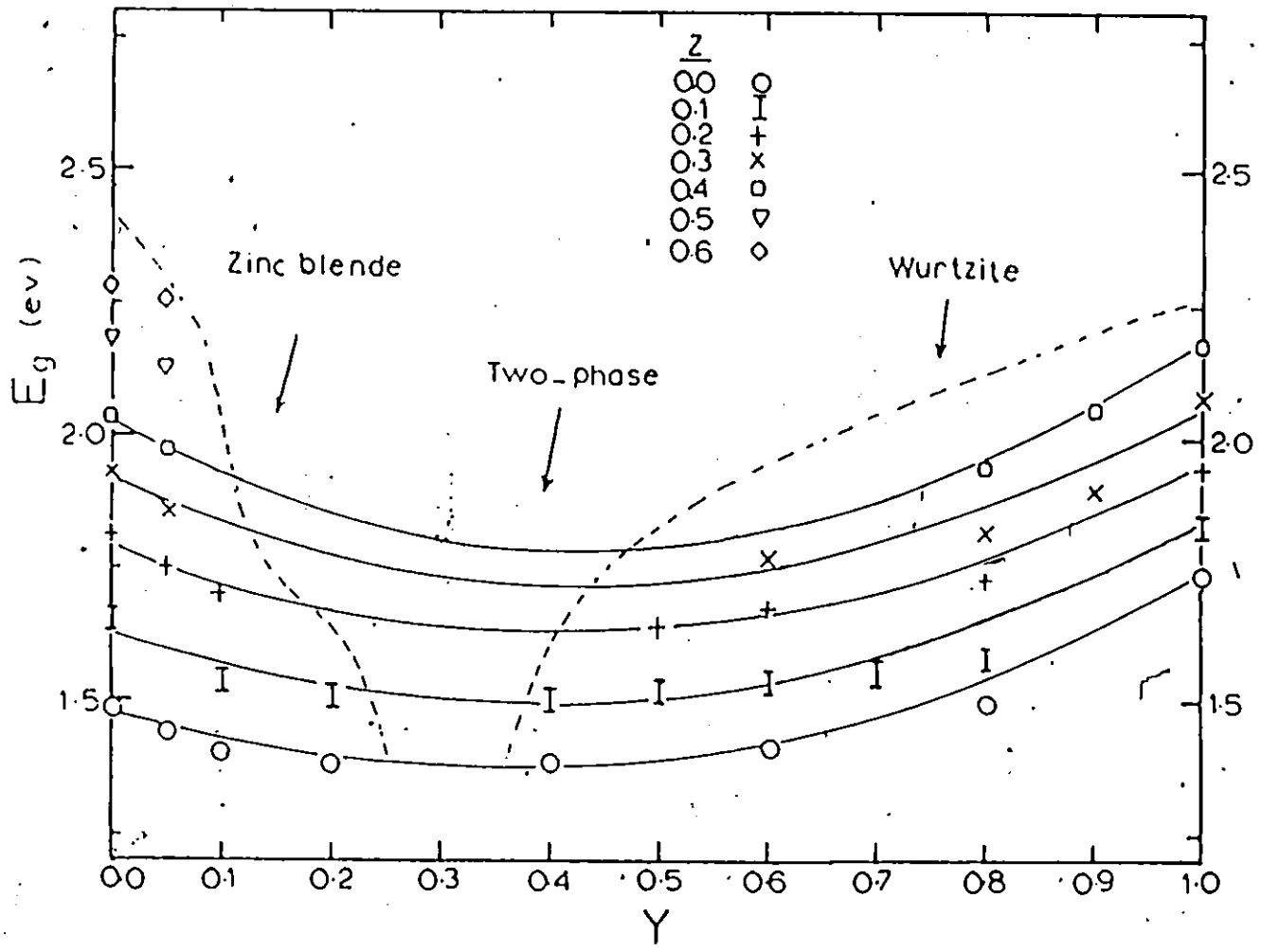

Fig. 5.6. Variation of room temperature energy gap E_g with y for lines of constant z. The solid lines —— are fitted curves obtained by fitting equation 5.4 to the experimental values of E_g. The dashed lines show the boundaries of the single phase fields.

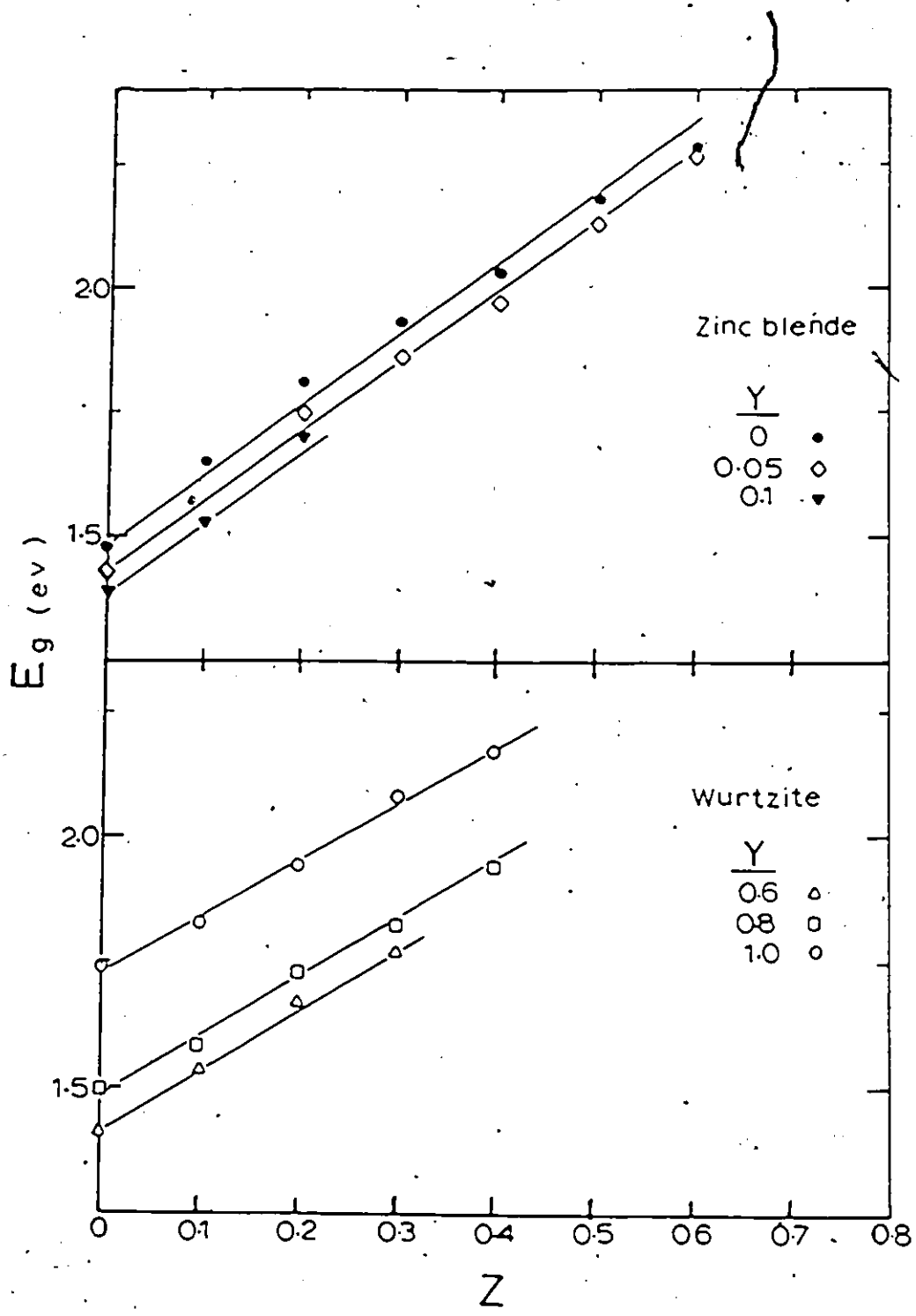

Fig. 5.7. Varition of room temperature energy gap E_g with z for lines of constant y.

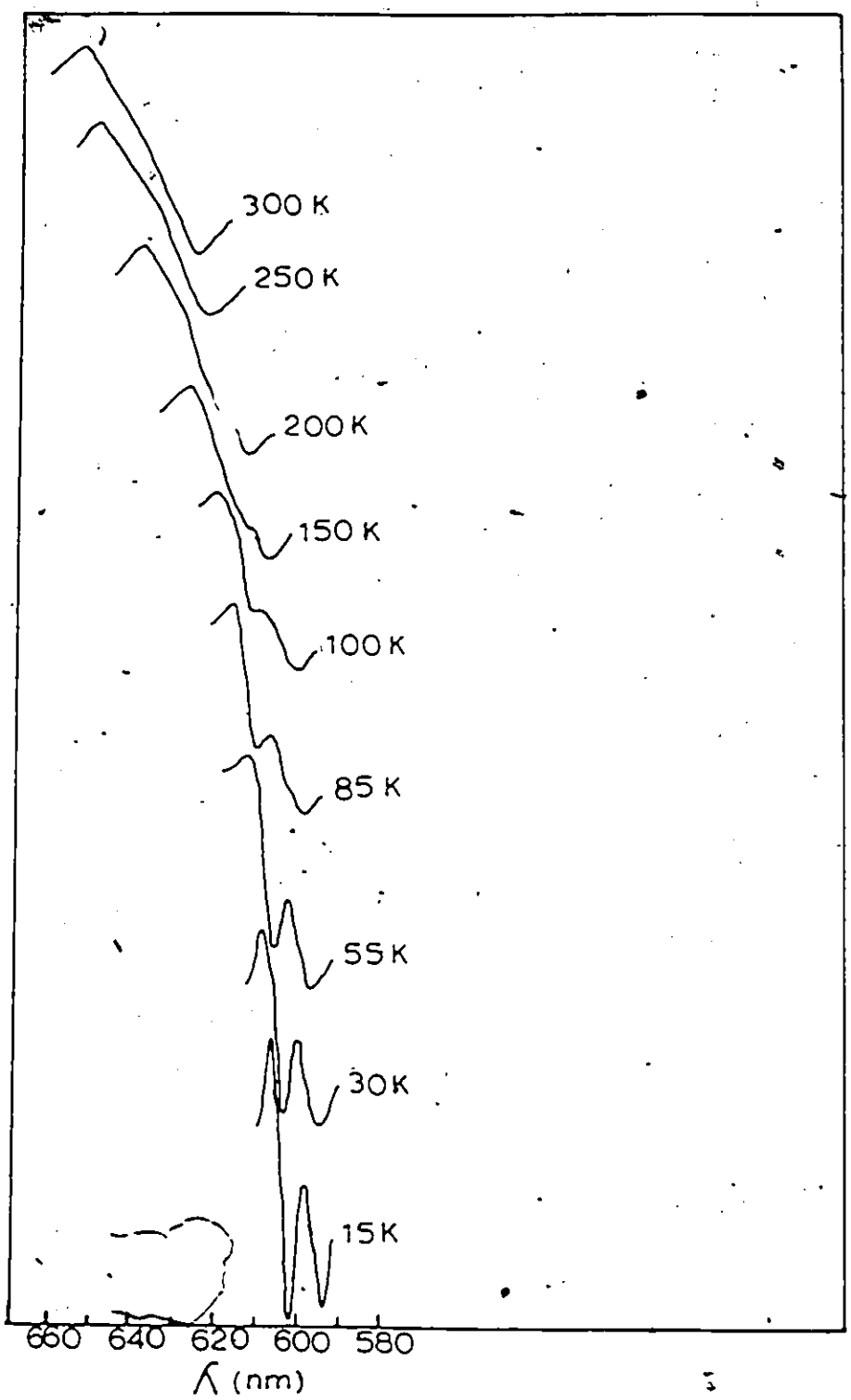

Fig. 5.8. Wavelength Modulated Reflectance spectra at various temperatures of $Cd_{0.8}Mn_{0.2}Se$.

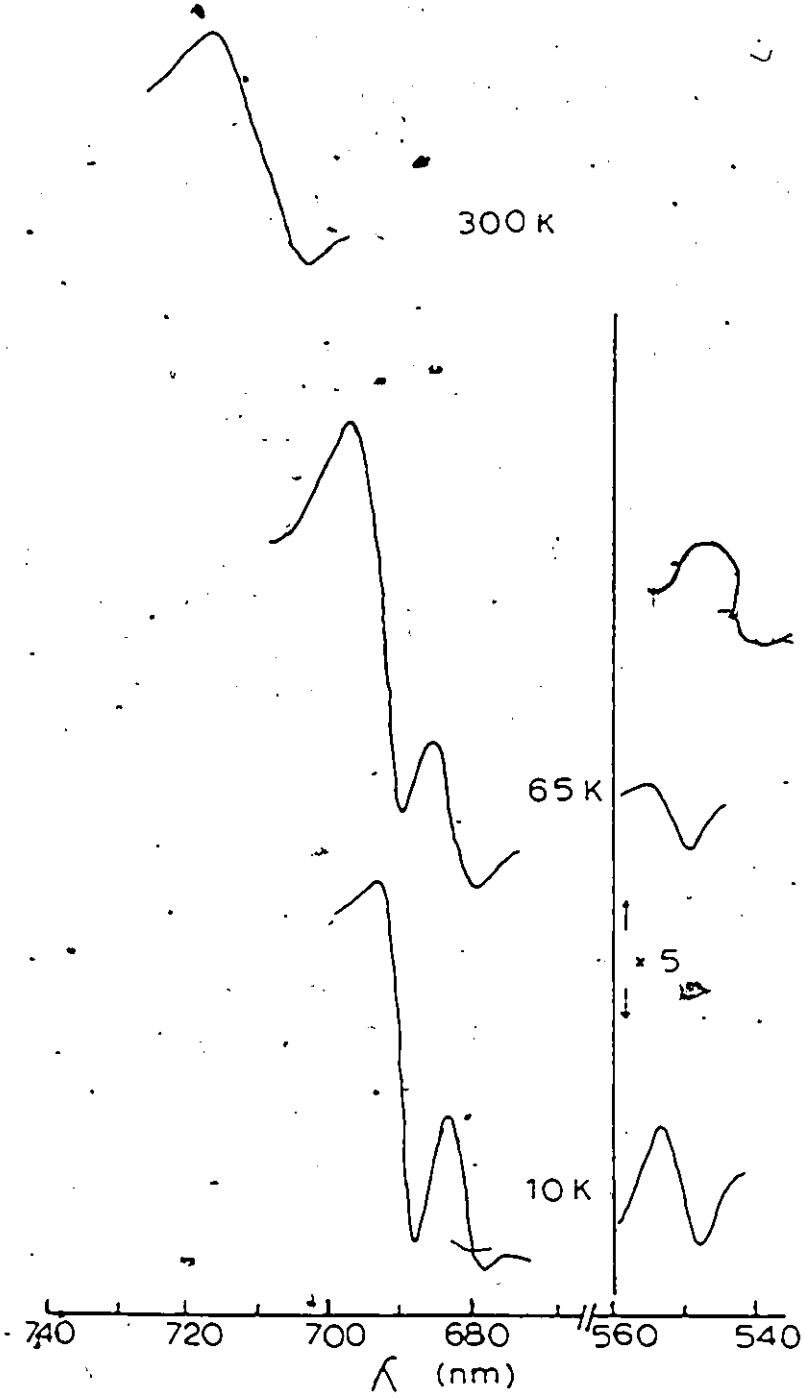

Fig. 5.9. Wavelength Modulated Reflectance spectra at three different temperatures of CdSe .

and not single crystals. However in the case of $Cd_{0.7}Mn_{0.3}Se$ a th[illegible] additional structure was observed in the low temperature region, but we could not be sure if this was due to an E_C-type transition (vb lower Γ_7 - cb Γ_7), or to the excitation of Mn^{2+} states. This will be discussed in a little more detail below.

The dependence of E_A and E_B on temperature is presented in Fig. 5.10. Also the dependence of E_C (for the CdSe) and E_i (the third transition observed in $Cd_{0.7}Mn_{0.3}Se$) on temperature is shown in Fig. 5.11.

5.6 Discussion and Analysis

Looking at the variation of the room temperature energy gap E_g with composition, we see that E_g seems to linearly increase with z (Fig. 5.7), with a variation rate slightly higher in the zinc blende case than in the wurtzite case. On the other hand, although E_g dependence on y is not linear (Fig. 5.6), E_g appears to vary smoothly and continuously with y, regardless of the missibility gap and hence of the change in the crystal structure. This should not be surprising knowing that both the zinc blende and wurtzite structures are identical up to the second nearest neighbour. A close look at Fig. 5.6 shows that E_g variation with y exhibits an upward concave non-linearity, corresponding to what is known as the optical bowing. The latter expresses the reduction in the optical band gaps of semiconductor alloys below a linearly interpolated value, which is the concentration weighted average of the band gaps of the constituant binary semiconductors [12]. The optical bowing has been found in III-V and

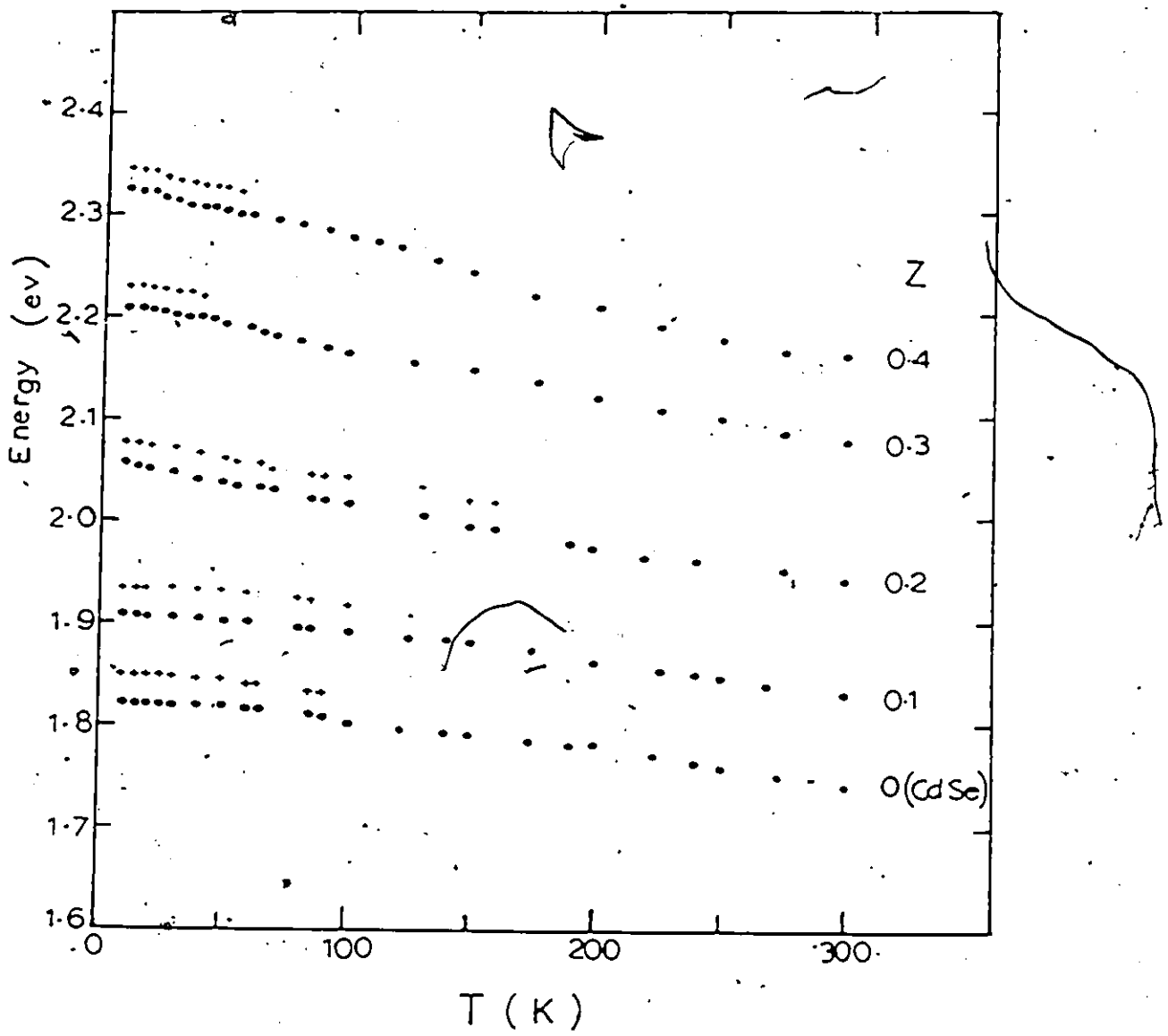

Fig. 5.10. Variation of transitions energy E_A(•) and E_B(+) with temperature for various $Cd_{1-z}Mn_zSe$ alloys. E_A represents the fundamental energy gap; E_B represents the transition from the crystal-field-split valence band to the conduction band.

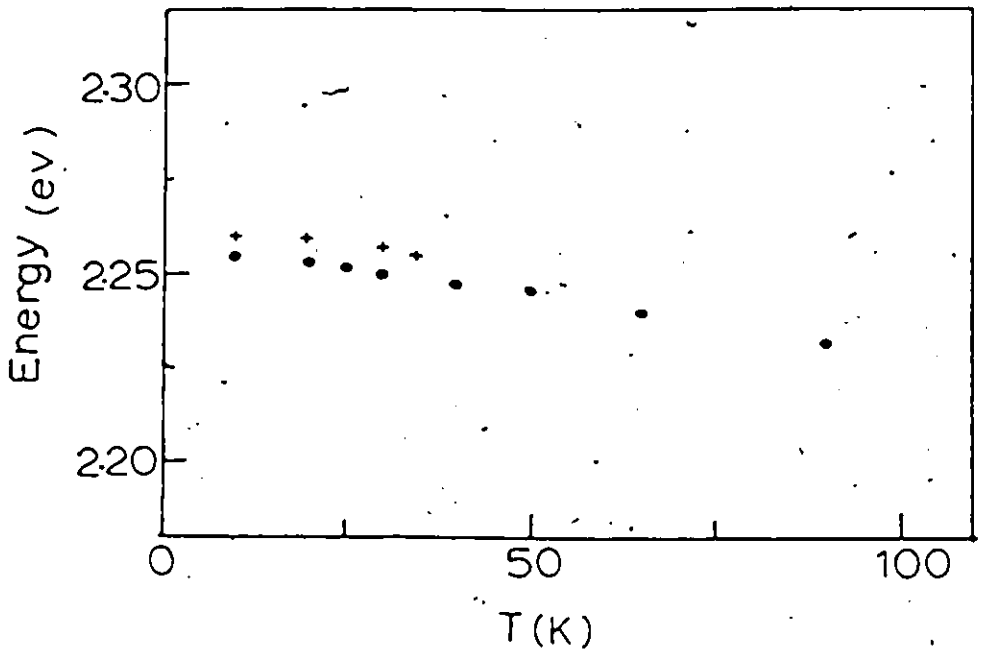

Fig. 5.11. Temperature dependence of the higher-energy transition for CdSe(•) and $Cd_{0.7}Mn_{0.3}Se$(+).

II-VI pseudo binary alloys [13-16] and has been recently discussed by Zunger et al [12].

Turning now to the values of the energy gap plotted in Fig. 5.6, each set of E_g values with constant z could be expressed by a parabola equation of the form:

$$E_g(y)_z = A(z) + B(z)y + C(z)y^2 \qquad (5.4)$$

where A, B and C are constant with respect to y, but depend on z. Consequently, for each line of constant z in Fig. 5.6, a set of values for the constants A, B and C could be obtained by a simple least square fit calculation. These values were determined and plotted as a function of z in Fig. 5.12. The standard deviation values obtained in each case are listed in Table 5.1. A, B and C show a systematic dependence on z; the constant C which is a measure of the curvative of the parabola, increases with z indicating an increase in the concavity and hence in the optical bowing of the constant z lines when going from the edge of z = 0, to the inside of our diagram. This can also be seen graphically in Fig. 5.6 where the fitted curves (represented by the solid lines) of equation (5.4) are drawn using the calculated values of A, B and C. The fact that the optical bowing appears to be stronger inside the diagram is not unreasonable, since here one expects contributions to the optical bowing to come from at least two edges of the diagram. The same behaviour has been previously observed by Moon et al [17].

As indicated earlier, the variation of the fundamental energy gap E_A with temperature is presented in Fig. 5.10 for the series $Cd_{1-z}Mn_zSe$. In all cases, E_A increases with decreasing the temperature. It is seen for the samples with low Mn concentrations (0%

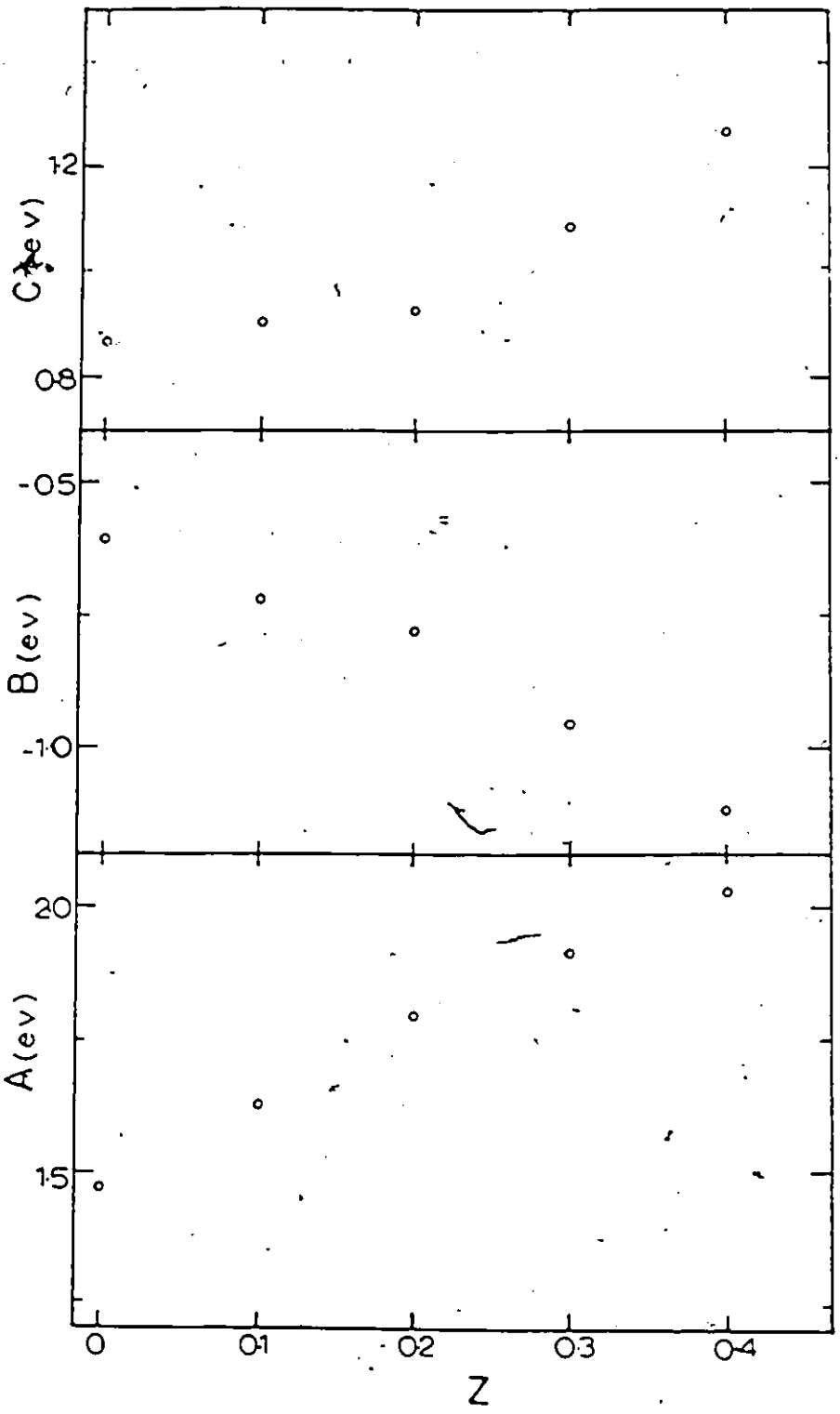

Fig. 5.12: Plot of the variation of the coefficients A, B and C of equation 5.4 with z.

Table 5.1: Standard deviations for the various lines of constant z obtained by fitting Equ. 5.4 to the experimental data of E_g shown in Fig. 5.6.

z	σ(eV)
0	0.022
0.1	0.036
0.2	0.022
0.3	0.039
0.4	0.006

and 10%), the curves of E_A vs T are of the standard form observed with conventional non-magnetic semiconductors. However for the samples with higher Mn concentrations (20%, 30% and 40%), the shape of the curve at lower temperature is changed, an increase in E_A in this range giving a curve which is almost linear, instead of a bent over curve. This increase ΔE in the energy gap is attributed to the presence of the magnetic Mn spins and hence to magnetic effects which are absent in non magnetic semiconductors. We note that the present results are similar to those obtained by Stankiewicz [18] for $Cd_{1-z}Mn_zSe$.

In order to determine the increase ΔE in the band gap due to magnetic effects, it was necessary to extrapolate the higher temperature regions of the curves, where the magnetic effects were negligible. This was done using a simple Manoogian-Leclerc equation

[19] of the form:

$$E_A(0) - E_A(T) = UT^{2/3} + V\theta(\coth \frac{\theta}{2T} - 1) \qquad (5.5)$$

where U, V and θ are constant independent of T. As has been shown previously by Manoogian and Leclerc, the main contribution to the change in E_A is from the $V\theta$ dynamic term (lattice vibration or phonon), the $UT^{2/3}$ static term (lattice dilation effect) contributing only a small fraction over most of the temperature range. The two authors also indicated from the values of θ obtained in their experimental analysis that $K_B\theta$ agrees very well with known values for the mean optical phonon energy for the material concerned. An empirical relation between θ and the semiconductor concerned [20] showed that in the present work, θ could be taken as 240 K.

Knowing the value of θ, the curve of E_A vs T for z = 0 was fitted to equation (5.5) to obtain values of U and V: $U = 7.27 \times 10^{-4}$ eV/$K^{2/3}$, $V = 1.26 \times 10^{-4}$ eV/K. It was then assumed that because of the similarity of the alloys in the series $Cd_{1-z}Mn_zSe$, and the small effect of the $UT^{2/3}$ term, the expression for the samples could be written in the form:

$$E_A(0) - E_A(T) = N(z)\left[UT^{2/3} + V\theta(\coth \frac{\theta}{2T} - 1)\right] \qquad (5.6)$$

We note that a similar assumption had previously been made by Donofrio et al [23] in their study of the $Cd_xZn_yMn_zTe$ alloy system. For the curves with $z > 0$ only the parameter N(z) and $E_A(0)$ needed to be determined. Therefore, each curve was fitted to Equ. 5.6 for the range of temperature between room and ~150 K, in which the magnetic effects could be considered negligible, according to the magnetic susceptibility and ESR studies (chapter 3 and 4). The values of N(z)

and $E_A(0)$ so found, are listed in Table 5.2. By using these values, the values of $E_A(T)$ given by Equ. 5.6 were calculated down to 0 K, and the difference between these and the experimental values were taken as ΔE. The two sets of curves are plotted in Fig. 5.13, and the difference between each pair of curves clearly indicates the variation of ΔE with T.

Table 5.2: Values of the parameters N and $E_A(0)$ obtained by fitting Equ. 5.6 (see text for details).

z	N	$E_A(0)$ eV
0.1	1	1.913
0.2	1.351	2.046
0.3	1.547	2.195
0.4	1.75	2.296

In a theoretical study, Alexander et al [21] considered the effects of spin fluctuation, around a magnetic critical point such as T_g (the spin-glass transition temperature), on the energy value of the conduction band minimum, and indicated how the absorption edge of a semiconductor will change in that region due to these effects. Their analysis is made in terms of spin correlation functions and it shows that for a temperature region close to the critical point, the dominant

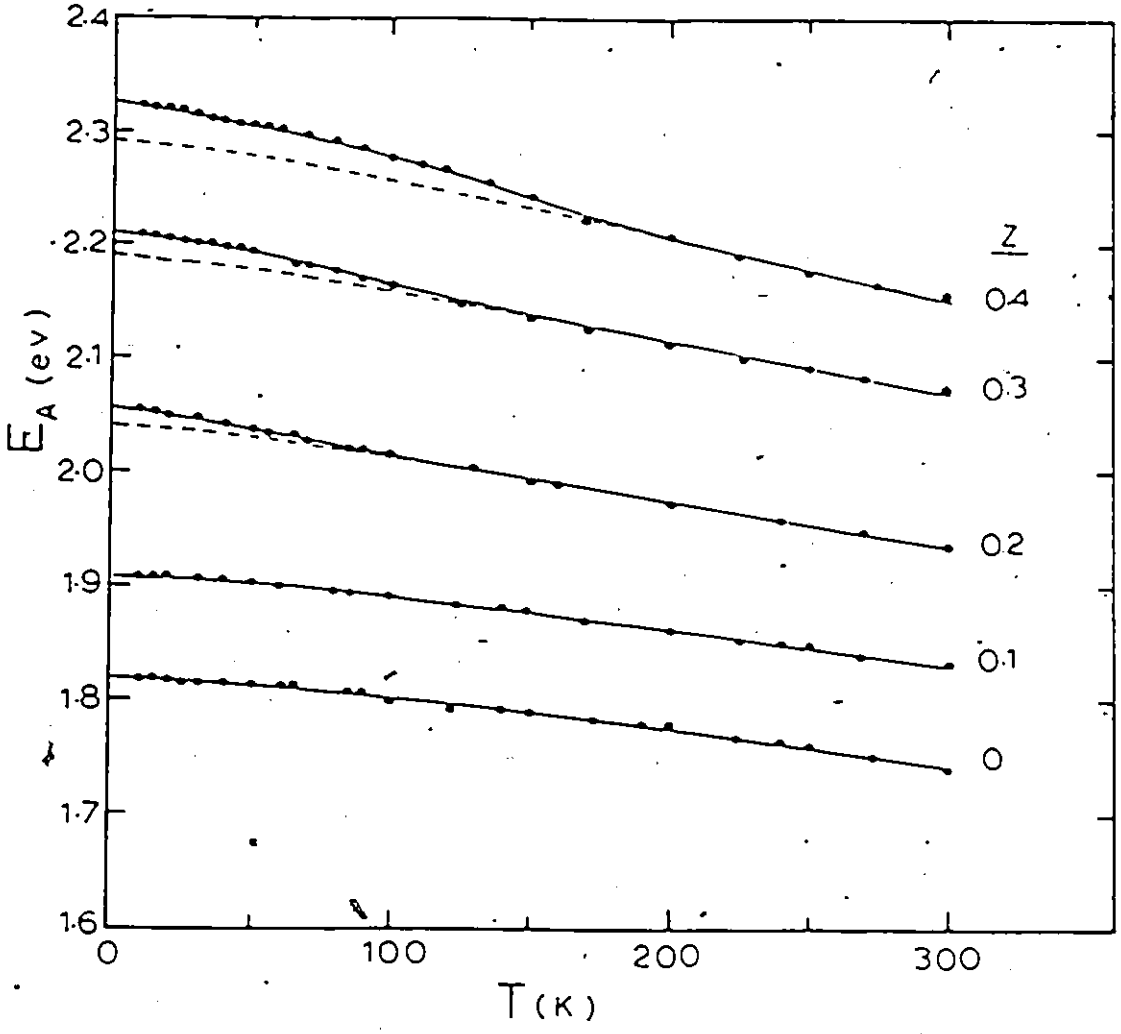

Fig. 5.13. Varition of E_A with temperature for various $Cd_{1-z}Mn_zSe$ alloys; full line —— experimental values, dashed line ---- extrapolated values.

contribution comes from short-range spin correlation, the long-range effects being relatively small in this region, but becoming relatively more important further from T_g. On this basis they showed that the variation of the magnetic contribution ΔE to the band gap satisfies the relation $\frac{d}{dt}(\Delta E) \alpha t^{-\mu}$, where t is the reduced temperature difference $\frac{|T-T_g|}{T_g}$ and the form of the exponent μ depends upon the particular conditions being considered. Including -P as a constant of proportionality, the variation of ΔE with t can be expressed as:

$$\frac{d}{dt}(\Delta E) = -Pt^{-\mu} \qquad (5.7)$$

and integration gives: $$\Delta E = \frac{-Pt^{1-\mu}}{1-\mu} + C \qquad (5.8)$$

Alexander et al, consider two different temperature regions; the critical one, close to T_g, where short-range spin correlations dominate, and non-critical region outside this critical one where the longer-range effects become important. For a semiconductor with antiferromagnetic interaction between the spins, Alexander et al showed that in the non-critical region, μ should have the values of 0.5 while Kasuya and Kondo [22] indicated that in the critical region, μ should have a value close to zero.

If the value of ΔE at T_g is written as ΔE_c, then the constant of integration in Equ. 5.8, $C = \Delta E_c$ and and Equ. 5.8 can then give:

$$\text{Ln}|\Delta E - \Delta E_c| = \text{Ln}\frac{P}{1-\mu} + (1-\mu)\text{Ln}t \qquad (5.9)$$

Thus, the present results can be analysed in terms of Equ. 5.9 and can give values for μ, which may be compared with the theoretical predictions, and values for P, which from Equ. 5.7 measures the strength of the total spin interaction on the band gap variation.

Using the values of T_g determined from magnetic susceptibility measurements (given in Table 5.3), the value of ΔE_c was determined for each sample and values of $Ln|\Delta E - \Delta E_c|$ plotted against Lnt. The results are shown in Fig. 5.14, where it is seen that to a good approximation a straight line can be drawn through each set of points. For each sample, appropriate values of P and μ were determined from these lines. These values are listed in Table 5.3. All three μ values obtained lie very close to zero with a mean value of 0.026 and a deviation σ of 0.021. This is in good agreement with the prediction of Kasuya and Kondo, for the critical region. However, not enough data and lots of scatter prevented us from deducing any sensible results from the plot of $Ln|\Delta E - \Delta E_c|$ vs Lnt points which lie beyond the ones shown in Fig. 5.14. As a result, no conclusion could be drawn on the non-critical temperature region. Values of P also determined from the straight lines drawn in Fig. 5.14, are plotted against the Mn

Table 5.3: Values as a functions of Mn concentration of the parameters from Equ. 5.9.

z	T_g(k)	μ	P(eV)
0.2	~(1.5)	0.057	3×10^{-4}
0.3	6.1	0.009	10×10^{-4}
0.4	12.1	0.011	21×10^{-4}

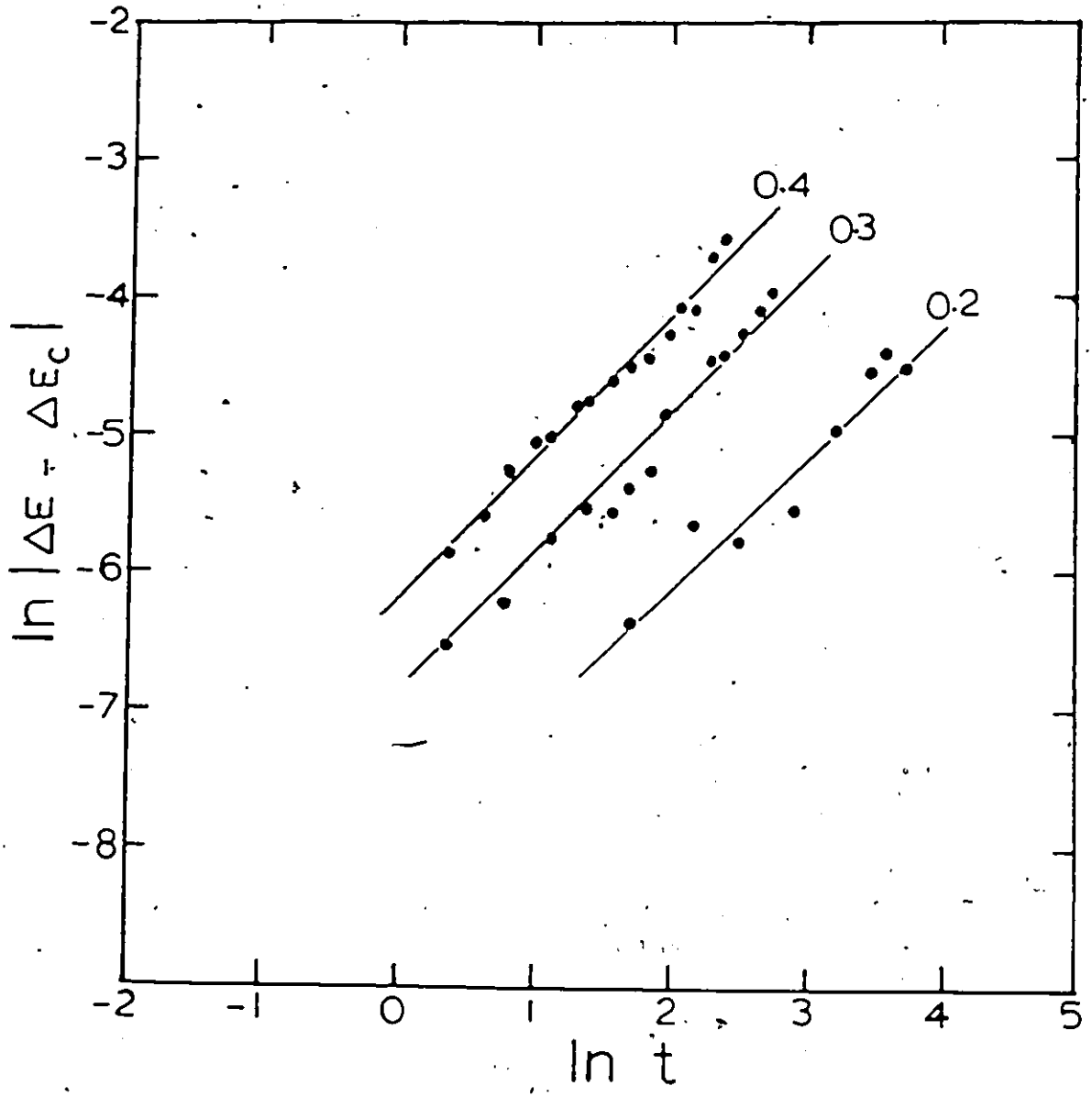

Fig. 5.14. Variation of $\ln|\Delta E - \Delta E_c|$ with ln t for $Cd_{1-z}Mn_zSe$ alloys. Values of z are shown on graph.

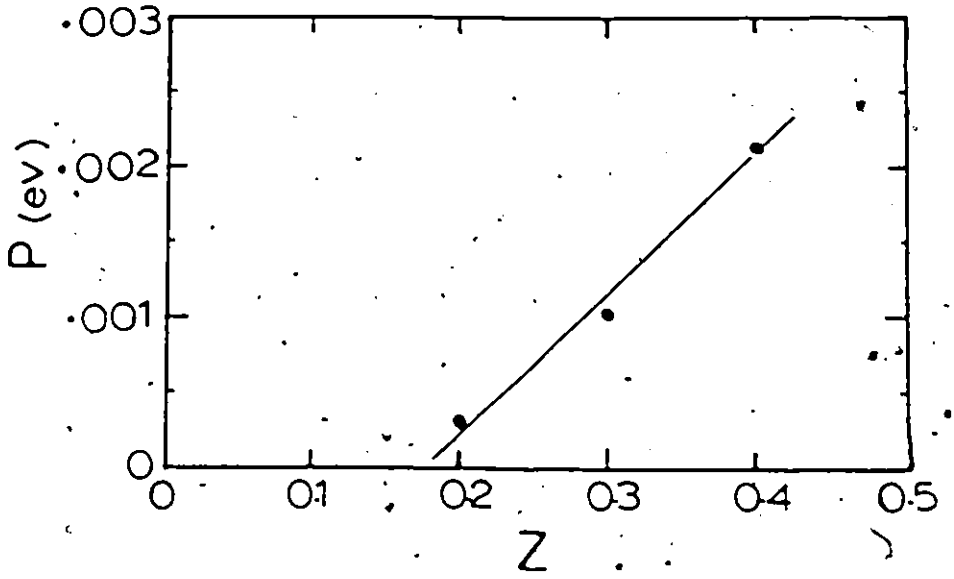

Fig. 5.15. Variation of P with manganese composition z.

concentration z in Fig. 5.15. It is seen that the variation of P with z can be represented by a straight line giving P = 0 at a value of z ~ 0.18, the nearest neighbor percolation limit shown by the magnetic susceptibility results (see chap. 3). Thus, as is not unreasonable in this range, above this percolation limit the magnitude of the magnetic effects varies linearly with Mn concentration. It is important to note that the results of the present analysis agree very well with Donofrio et al results for the $Cd_xZn_yMn_zTe$ alloy system [23].

It is often of interest to know the value of the energy gap E_A near to absolute zero. The graphs of the experimental values of E_A vs T in Fig. 5.13 were extrapolated to give the experimental value of $E_A^{ex}(0)$ and these are shown plotted against z in Fig. 5.16. As can be seen, to a good approximation, a straight line can be drawn through these points. For the sake of comparison the values of the room temperature energy gap $E_A(300)$ ($=E_g$ in Fig. 5.7) plotted against z, are also shown in the same figure. It is of interest to note the divergence between $E_A^{ex}(0)$ and $E_A(300)$ lines. Thus, because of the magnetic effect, the difference $E_A^{ex}(0) - E_A(300)$ is much larger for the sample with z = 0.4 than for the non-magnetic sample (CdSe) with z = 0.

As we indicated earlier, the transition E_B from the crystal-field-split valence band Γ_7 to the conduction band Γ_7, was observed in the low temperature region. The variation of E_B with T is presented in Fig. 5.10 for all the samples investigated. It is seen that the transition E_B lies slightly higher than the fundamental transition E_A, with the separation $E_1 = (E_B - E_A)$ not showing any significant dependence

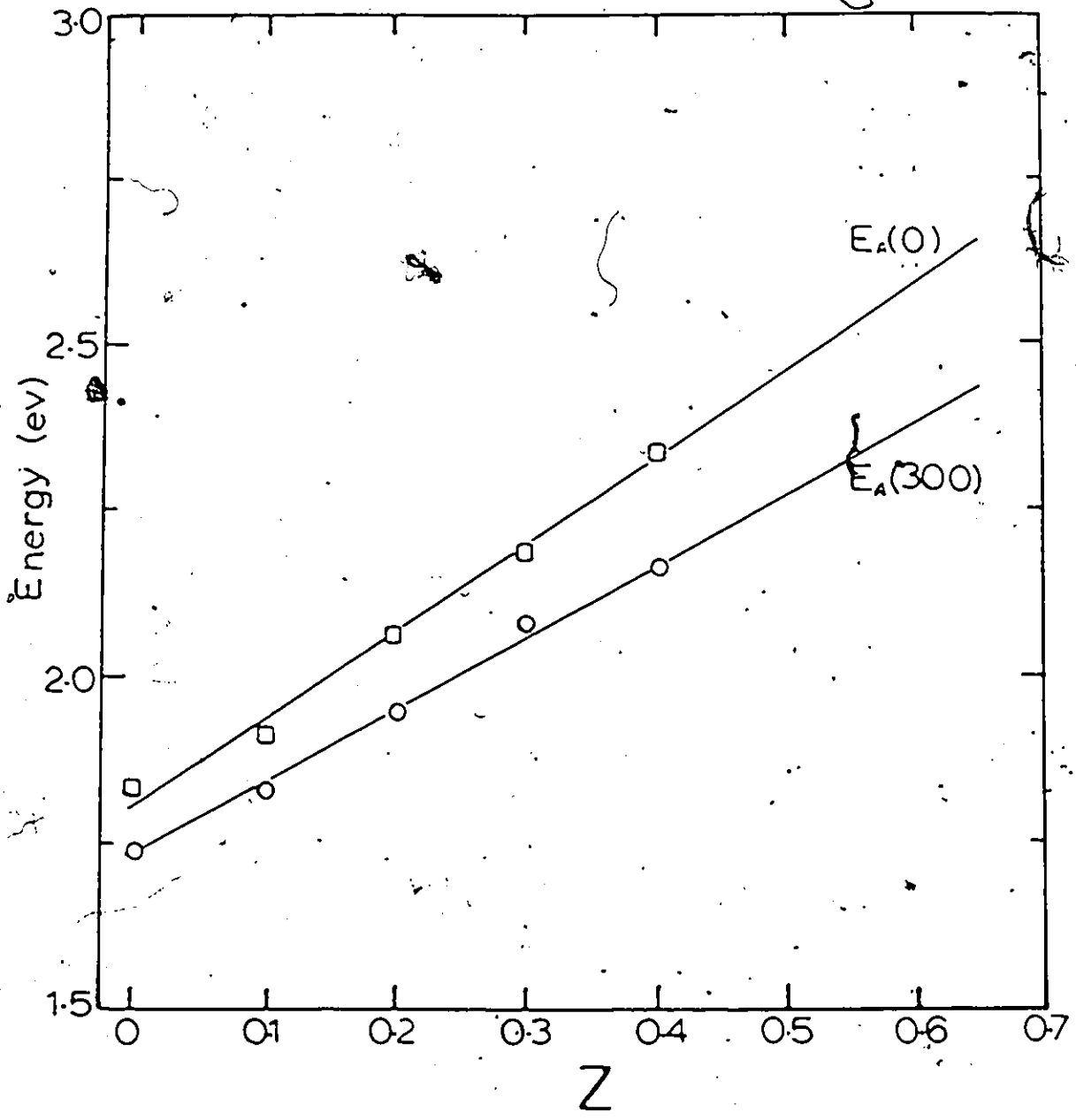

Fig. 5.16. Variation of fundamental energy gap at absolute zero $E_A(0)$, and at room temperature $E_A(300)$, with z .

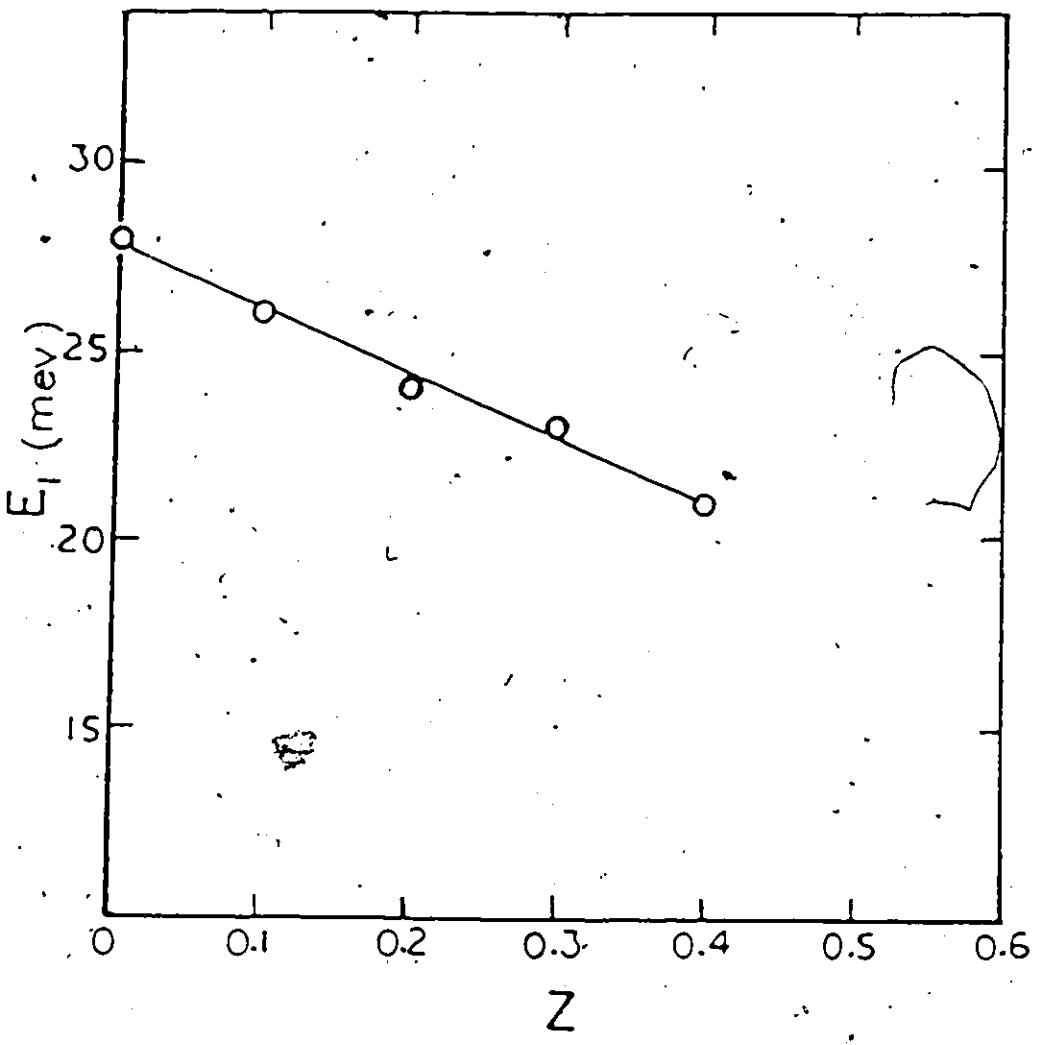

Fig. 5.17. Varition of the energy separation $E_1 = (E_A - E_B)$ as a function of the composition z.

on the temperature. The "crystal-field separation" E_1 is shown as a function of Mn concentration z in Fig. 5.17 where E_1 shows a decrease with increasing z. The present results are in close agreement with those obtained previously by Stankiewicz [18]. As mentioned earlier the valence-band splitting in wurtzite crystals is caused by the noncubic crystalline field, and it is much smaller than the spin-orbit splitting in the case of the CdSe compound [24,25]; its magnitude depends on the bond type (e.g. effective charge) and on the departure from the ideal (perfect) wurtzite structure. Knowing that the lattice-constant ratio $\frac{c}{a}$ of CdSe is practically equal to the ideal value of 1.633, and since the total change in the c/a ratio for the investigated range of composition is less than 10^{-3} (see chap. 2, also [26]), it does not seem probable that the built-in uniaxial deformation due to this change is the dominant factor in the observed splitting. According to Stankiewicz the variation of the crystal-field splitting is due mainly to the difference between substituent and substituted (Mn and Cd) which differ in their ionic radii by 21%.

As we mentioned earlier, a higher-energy transition was observed in the case of CdSe and of $Cd_{0.7}Mn_{0.3}Se$, at low temperatures. The temperature dependence of these transitions, are shown in Fig. 5.21. The assignment of these structures to the transition (E_C) from the spin-orbit-split valence band to the conduction band was certain in the case of CdSe, since the observed spin-orbit splitting, $E_2 = E_C - E_A$ (the energy difference between the higher-energy transition and fundamental transition) was found to be 0.430 ± 0.010 eV in agreement with previous results [18,24,25]. On the other hand, in the case of

the alloy $Cd_{0.7}Mn_{0.3}Se$, the energy difference was ~0.053 eV. Since we could not use the criterion of the light polarization effects, because we were dealing with a polycrystalline instead of a single crystal, and since no previous results have been available in the literature for comparison, we could not be certain about the nature of this transition, whether it was an E_C transition or was due to the excitation of Mn^{2+} states. In Stankiewicz's electroreflectance work on single crystals of $Cd_{1-z}Mn_zSe$ alloys, observation of the transition from the spin-orbit-split valence band to the conduction band has been reported on the samples with z = 0, 0.05, 0.1 and 0.2. No such transition has been observed for alloys with higher z. The E_2 values (the observed spin-orbit splitting) obtained by Stankiewicz show a strong variation with z. However, according to the theory [7], the valence band spin-orbit splitting parameter Δ, should be determined primarily by the p wavefunction and the potential near the anion (selenium) and should depend only weakly on the nature of the cation. This is not the case in $Cd_{1-z}Mn_zSe$, where it is suggested that the decrease in the spin-orbit splitting may result from the presence of Mn^{2+} d levels near the valence band. The admixture of d wavefunctions into the p-like valence band states will result in a reduction of Δ, since the d-orbital of a cation contributes a negative term to the spin-orbit splitting of the valence band at the Γ-point in ionic compounds with zinc-blende and wurtzite structures [27].

Quantitively speaking, one can approximatively estimate the fractional d-like character acquired by the valence band, as a result of the presence of Mn atoms. Using the linear hybridization model,

[27-30] in which the spin-orbit splitting parameter Δ, can be written as a linear sum of the p and d contribution i.e.

$$\Delta = \alpha\Delta_p + (1-\alpha)\Delta_d \qquad (5.10)$$

where α is the fractional p-like character in the valence band, and hence $(1-\alpha)$ the fractional d-like character. Δ_p and Δ_d are the spin-orbit splitting of the p and d levels respectively. In order to obtain α from Equ. 5.10 Δ, Δ_p and Δ_d have to be determined first.

Knowing the values of E_1 and E_2, the energies of the Γ_7 valence band levels relative to the Γ_9 valence band level (to be consistent, we use the results of Stankiewicz [18] for E_1 and E_2 which are listed in Table 5.4), one can calculate the values of the spin-orbit splitting Δ and the crystal field splitting δ, parameters by using the Hopfield relation [31].

Table 5.4: Values of the crystal-field and spin-orbit splitting parameters δ and Δ obtained using the Hopfield relation (Equ. 5.11). The values of E_1 and E_2 are taken from Ref. 18.

z	E_1(meV)	E_2(meV)	δ(meV)	Δ(meV)
0(CdSe)	27	440	42	425
0.05	26	411	40.4	396.6
0.1	25	390	39	376
0.2	22	312	34.4	299.6

$$E_{1,2} = \frac{1}{2}(\Delta+\delta) \mp \left[(\Delta+\delta)^2 - \frac{8}{3}\Delta\cdot\delta\right]^{\frac{1}{2}} \qquad (5.11)$$

The values of Δ and δ obtained this way are listed in Table 5.4.

Following the analysis of Braustein and Kane [32] and of Poplavnoi and Polygalov [33] it will be assumed for the II-VI compounds that:

$$\Delta_p = G_p \left(\frac{2}{8}\Delta_p II + \frac{6}{8}\Delta_p VI\right) \qquad (5.12)$$

where $\Delta_p II$ and $\Delta_p VI$ are the atomic spin-orbit splittings of the elements and G_p is an enhancement factor for the solid. For the case of $Cd_{1-z}Mn_zSe$ Equ. 5.12 becomes:

$$\Delta_p = G_p \left\{\frac{2}{8}\left[(1-z)\Delta_p(Cd) + z\Delta_p(Mn)\right] + \frac{6}{8}\Delta_p(Se)\right\} \qquad (5.13)$$

For both zinc blende [32,34] and chalcopyrite [33] structures, G_p has been taken to be 29/20; we will assume that this is also valid for the case of wurtzite structure, since the latter structure, similarly possesses the tetrahedral symmetry (the atoms have tetrahedral coordinations). The values of $\Delta_p(Cd)$, $\Delta_p(Mn)$ and $\Delta_p(Se)$ have been taken from different sources, and are listed in Table 5.5. In this Table, the two listed values of $\Delta_p(Se)$ are taken from Ref. 33 and they correspond to the total angular momentum quantum numbers J = 2 and J = 1. Neither one of theses two values nor their average gives an exact α value of one for the CdSe (z = 0), the valence band of which has a purely p-like character. So, by using Equ. 5.13 and working backwardly, (take α = 1 for CdSe and use for G_p the previously mentioned value of 29/20) we were able to obtain a value of 334.6 meV for $\Delta_p(Se)$, which will be used in the rest of the analysis. Note that this calculated value for $\Delta_p(Se)$ lies between the other two given values, which makes it acceptable.

Table 5.5: Atomic p spin-orbit splittings of elements used in the analysis (in meV).

Δ_p(Cd) = 210[a]

Δ_p(Mn) = 5[b]

Δ_p(Se) = $\left\{\begin{matrix}370\\202.2\end{matrix}\right\}$[c], used value 334.6[d]

a- Ref. 34

b- Ref. 35,36

c- Ref. 33

d- see text for details

For Δ_d, only the effects of manganese d electrons are considered, since the other d levels, those of cadmium, are much too deep to contribute [3]. Thus, Δ_d is assumed to be given by:

$$\Delta_d = G_d \, z \, \Delta_d(Mn) \qquad (5.14)$$

The fivefold-degenerate d levels, in a tetrahedral environment, splits into a triplet and doublet; the triplet lies at higher energy, and has the same symmetry as the p levels, so that the d triplet under these conditions, acts like the p-levels [28]. As a result, it is assumed that the G_d also has the value of 29/20 [28,29]. Also in a tetrahedral environment, $\Delta_d(Mn) = -3/2 \; \tau_d(Mn)$ [27], where $\tau_d(Mn)$ is the Condon-Shortley one-electron spin-orbit splitting parameter [35]. The minus sign is introduced to indicate that the d-levels spin-orbit splitting is negative. From reference 35, $\tau_d(Mn) = 37.2$ meV i.e. $\Delta_d(Mn) = -55.8$ meV.

Going back to equation (5.10), all three parameters Δ, Δ_p and Δ_d can then be obtained for the three alloys with z = 0.05, 0.1 and 0.2, and hence the fractional p-like character, α, values can be estimated. This is done, and the results of α and its dependence on z are shown in the graph of Fig. 5.18. As seen, α decreases with increasing the Mn concentration z, meaning that the fractional d-like character, $(1-\alpha)$, in the valence band increases when we increase the amount of Mn in the alloy. This indicates that there is a certain degree of delocalization of the manganese d-electrons. Recent synchrotron radiation study of $Cd_{1-z}Mn_zTe$ [37] showed that there is certain degree of delocalization and hybridization of the Mn $3d^5$ levels in this family of materials.

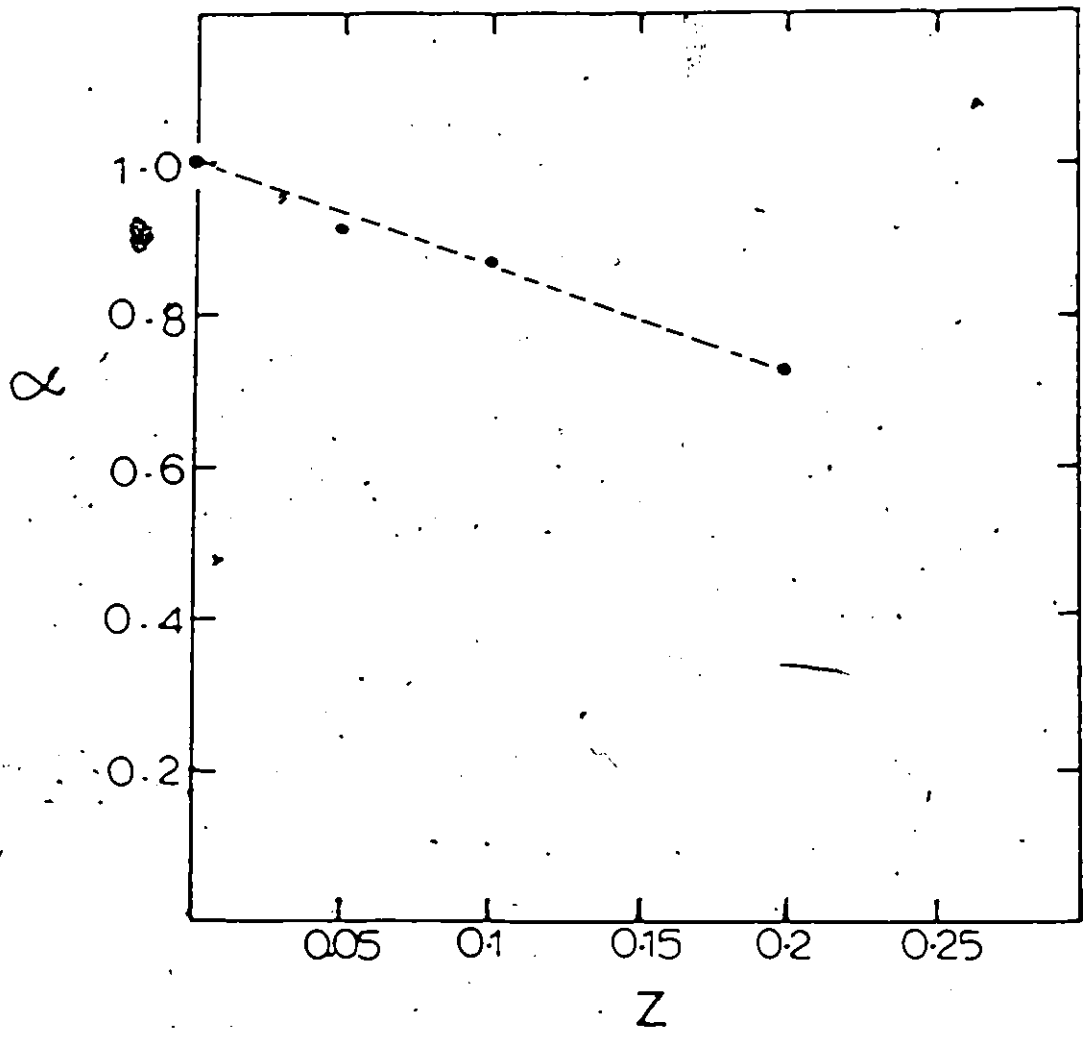

Fig. 5.18. Variation of fractional p-like character of valence band α with z; the fractional d-like character is given by $(1 - \alpha)$.

Finally, we note that we attempted to apply this analysis to the alloy $Cd_{0.7}Mn_{0.3}Se$ using our results for the values of E_1 and E_2 i.e. $E_1 = 23$ meV, $E_2 = 53$ meV; by that we assume that the higher energy transition observed for this alloy is due to the spin-orbit splitting of the valence band. However, the Hopefield relation (Equ. 5.11) was unsolvable for this set of E_1 and E_2 values. To obtain a solution from Equ. 5.11 one has to have $E_2 > 3.73\ E_1$, which makes it also impossible to obtain a solution, using for E_1 the value of 19 meV obtained by Stankiewicz [18]. We are not certain whether the inapplicability of the Hopefield relation in this case, is due to the fact that the third observed transition originates from some kind of Mn^{2+} states excitation rather than being due to an E_C-type transition (vb spin-orbit Γ_7 - cb Γ_9), or to the fact that there is a high degree of p-d hybridization, which makes Equ. 5.11 inappropriate, since as has been been shown by Yoode et al [28], the Hopefield model is a limiting case of the more general model proposed by them.

5.7 Conclusion

In this work, using the wavelength modulated reflectance technique, the room temperature energy gap E_g was determined as a function of composition in the wurtzite and zinc blende single-phase fields of the $(Cd_{1-z}Mn_z)(Te_{1-y}Se_y)$ diagram. It has been found that for constant y the variation of E_g with z is linear, whereas for constant z the variation of E_g with y has a parabolic-like behaviour which seems to be insensitive to the change of the structure (from zinc blende to wurtzite or vice versa).

Temperature dependent energy gap measurements was carried out on the diagram edge $Cd_{1-z}Mn_zSe$. For all the investigated samples, two different structures were observed in the low temperature region, corresponding to the fundamental transition E_A (vb Γ_9 - cb Γ_7) and to the crystal-field-split valence band transition E_B (vb upper Γ_7 - cb Γ_7'). The transition from the spin-orbit-split valence band to the conduction band, E_C, was observed only in the case of the CdSe compound. The variation of E_A with T was studied in some detail. It has been found that for samples with low Mn concentration ($z < 0.2$) E_A depends on T in a classical fashion (linear change in the high temperature region and bending over in the low temperature region); however, for samples with higher Mn concentration ($z > 0.2$) the values of E_A are increased by an appreciable amount, at low temperatures by the magnetic effects in the semiconductor, the increase ΔE being effectively proportional to the Mn concentration z. The magnitude of the effect is illustrated by the results in Fig. 5.17 where the values of $E_A^{ex}(0) - E_A(300)$ are 0.08 eV for $z = 0$ and 0.18 eV for $z = 0.4$. The values of ΔE for any given sample can be analysed in terms of the theoretical relations of Alexander et al for the effect of critical point phenomena on the band gap and good agreement with theory is obtained.

The observed crystal-field splitting $E_1 = (E_B - E_A)$ has been found to decrease when increasing z, this is in agreement with the results of Stankiewicz who has also found a decrease in the observed spin-orbit splitting $E_2 = (E_C - E_A)$, with increasing z. This has been interpreted as due to an admixture of the Mn d-orbitals with normal

p-orbitals forming the valence band . Using Stankiewicz's[9] data, we were able to approximatively estimate the dependence of the fractional d-like character in the valence band (at the Γ-point), on the Mn concentration basing our analysis on the linear hybridization method.

REFERENCES

1. M.B. Brandt and V.V. Moshchalkov, Advances in physics, 33, no.3, 193 (1984).
2. J.K. Furdyna, J. App. Phys. 53, 7637 (1982).
3. David L. Greenaway and Gunther Harbeke, "Optical Properties and Band Structure of Semiconductors", Pergamon press char. 5, 6 (1968).
4. J.L. Birman, Phys. Rev. 115, 1493 (1959).
5. J.L. Birman, Phys. Rev. 114, 1490 (1959).
6. H.L. Lipkin, Phys. Rev. Lett. 2, 159 (1959).
7. S.L. Alder, Phys. Rev. 126, 118 (1962).
8. R.A. Abrew, W. Giriaf, M.P. Vecchi, Phys. Lett. 85A, 399 (1981).
9. N.T. Khoi, J.A. Gaj, Phys. Stat. Sol. (b) 83, K133 (1977).
10. C. Kittel, "Introduction to solid physics", Fifth Ed. Ch. 11, Wiley (1976).
11. David L. Greenaway and Gunther Harbeke, "Optical Properties and Band Structure of Semidonductors" Pergamon press, Ch. 4.
12. A. Zunger and J.E. Jaffe, Phys. Rev. Lett. 51, 662 (1983).
13. A.M. Joullie and c. Allibert, J. Appl. Phys. 45, 547 (1974).
14. A. Onton, M.R. Lorenz and W. Renter, J. Appl. Phys. 42, 3420 (1971).
15. S.S. Vishnubhatla, B. Eyglament and J.C. Woolley, Can. J. Phys. 47, 1661 (1969).
16. S. Larach, R.E. Schrader and C.F. Stockner, Phys. Rev. 108, 587 (1957).

17. R.L. Moon, G.A. Antypas and L.W. James, J. Electrons Mater, 3, 635 (1976).

18. J. Stankiewicz, Phys. Rev. B 27, 3631 (1983).

19. A. Manoogian and A. Leclerc, Phys. Status Solidi B 96, K23 (1979); Can. J. Phys. 57, 1766 (1979).

20. A. Manoogian, Unpublished results.

21. S. Alexander, S.J. Helman and I.Balberg, Phys. Rev. B 13, 304 (1976).

22. T. Kasuya and A. Kondo, Solid State Comm. 14, 249 (1974).

23. T. Donofrio, G. Lamarche and J.C. Woolley, J. Appl. Phys. 57, 1932 (1985).

24. M. Cardona, K.L. Shakla and F.H. Pollack, Phys. Rev. 154, 696 (1967).

25. J.O. Dimmak and R.G. Whaler, Phys. Rev. 125, 1805 (1962).

26. H. Wiedermeier and A.G. Sigai, J. Electrochem. Soc. 117, 551 (1970).

27. K. Shindo, A. Morita, J. Phys. Soc. Jap. 20, 2054 (1965).

28. K. Yoodee, J.C. Woolley and V. Sayakanit, Phys. Rev. B 30, 5904 (1984).

29. S.A. Lopez-Rivera, R.G. Goodchild, O.H. Hughes, J.C. Woolley and B.R. Pamplin, Can. J. Phys. 60, 10 (1981).

30. N. Yamamoto, H. Horinaka, and T. Miyauchi, Jpn. J. Appl. Phys. 16, 1817 (1977).

31. J. Hopfield, J. Phys. Chem. Solids, 15, 97 (1960).

32. R. Braunstein and E.O. Kane, J. Phys. Chem. Solids, 23, 1423 (1962).

33. A.S. Poplavnoi and Y.U.I. Polygalov, Inorg. Mater. (USSR) 7, 1527 (1971); 7, 1531 (1971).

34. M. Cardona, "Modulation Spectroscopy" Academic press, N.Y. 1969 p. 67.

35. E. Condon and G. Shortley, "The Theory of Atomic Spectra", Cambridge University press (1935) Ch. 7.

36. Prof. R. Hodgson, University of Ottawa, private communication.

37. M. Tanigachi, L. Ley, R.L. Johnson, J. Ghisson and M. Cordona, Phys. Rev. B 33, 1906 (1986).

Chapter 6

MAGNETIC PROPERTIES OF THE δ* PHASE-FIELD IN THE $[Cd_{1-z}Mn_z][Te_{1-y}Se_y]$ DIAGRAM

6.1 Introduction

In chapter 2, two isothermal sections of the $(Cd_{1-z}Mn_z)(Te_{1-y}Se_y)$ phase diagram are presented (see Figs. 2.6-2.7). As one can see, in the region of the right top corner of those two isothermal sections, there exists a single-phase field (δ) with sodium chloride structure, with the 960°C section giving a substantially larger field than the 600°C section. This δ-phase field is "derived" from the compound MnSe which has the same structure; consequently, samples which belong to this field are expected, to some extent, to have similar behaviour to that of MnSe.

From neutron diffraction work of Shall et al [1], it has been shown that δ-MnSe(+) at low temperature, order as a fcc type-II antiferromagnet like MnO. Therefore, the magnetic susceptibility of MnSe was expected to behave, with respect to temperature, in a similar fashion to that of a typical antiferromagnetic material, such as MnO (Fig. 6.1). As Fig. 6.1 shows, χ increases while lowering the temperature following the Curie-Weiss law, until the Neel temperature

---

* According to the nomenclature we used in Chapter 2, δ represents the NaCl structure.

(+) We used δ-MnSe instead of the regular convention α-MnSe which means MnSe with NaCl structure.

T_N is reached where a peak-like maximum occurs; in the range of temperatures below T_N, χ decreases with the temperature. Also, for an antiferromagnetic material the χ vs T curve is usually reversible.

However, a number of early investigations showed that [2-4] certain anomalies as well as hysteresis effects were exhibited in the magnetic susceptibility of δ-MnSe in a wide temperature range centered around 160 K. Thermal hysterisis effects were also observed in other physical properties such as electrical resistivity [5] and the intensity of the absorption line in ESR [6]. Specific heat measurements on polycrystalline materials carried out by Kelley [7], revealed two distinct heat effects in the temperature range $50 < T < 300$ K. The measurements were carried out by increasing the temperature. A small "hump" was found around 116 K and a strong peak in the vicinity of 240 K. The latter was reported to be subject to hysteresis, while the former was not reproducible on repeated measurements.

More recent investigations on δ-MnSe [8-12] showed practically the same kind of behaviour as the early ones. All these observations resulted in at least three different characteristic temperatures for MnSe. One around 120 K, a higher one between 160 and 180 K and the highest in the vicinity of 240 K. The anomaly at the last temperature appears only in the heating process. Consequently, there has been confusion over the magnetic ordering temperature of δ-MnSe; also, it was not clear why these anomalies and thermal hysteresis occur. However, the discovery of a new low-temperature phase (NiAs-hexagonal) of MnSe, which was first observed by Taylor [13], using x-ray diffraction experiments performed below 160 K, was

the main key to finding the answers. The transformation from cubic (NaCl-type) to hexagonal (NiAs-type) was reported not to be complete. This is in accordance with a later study [14] in which high pressure experiments on δ-MnSe at room temperature were reported. It was found that under an applied pressure of ~90 Kbar δ-MnSe transforms into a hexagonal (NiAs-type) phase, but this transformation is only partial. Subsequent temperature dependent neutron diffraction studies on polycrystalline materials [15,16] confirmed the presence of the hexagonal phase; it has also been concluded that this phase exists only at low temperatures where it exists with the original cubic phase. The low temperature hexagonal phase reverts to the original cubic structure at room temperature.

More recently, further and more detailed study of the structural and magnetic properties of δ-MnSe in the low temperature region was performed by Van der Heide [17]. The author has established that the complicated behaviour of MnSe is due to a partial transformation to hexagonal-NiAs structure. According to him the sharp anomalies in the magnetic susceptibility at ~160 K and ~240 (see Fig. 6.2) are concomitant with the appearing and disappearing of the hexagonal phase. Also the susceptibility measurements indicate that equilibrium, if any, is reached only in a period of hours. Neutron diffraction and Mössbauer experiments revealed that the magnetic ordering temperature T_N of the cubic phase is ~115 K, and that the hexagonal phase is magnetically ordered at all temperatures at which it is observed. Therefore, he attributes the broad maximum in the susceptibility curve observed at ~150 K in the heating run (see Fig.

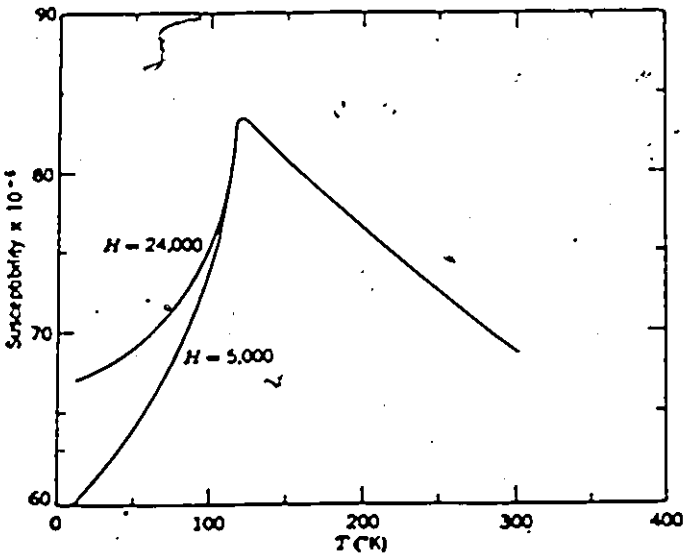

Fig. 6.1. Susceptibility of an MnO powdered specimen as a function of temperature for H = 5000 and 24,000 oe. (H. Bizette, C. Squire and B. Tsai, Compt. rend. (Paris) 207, 449 (1938).)

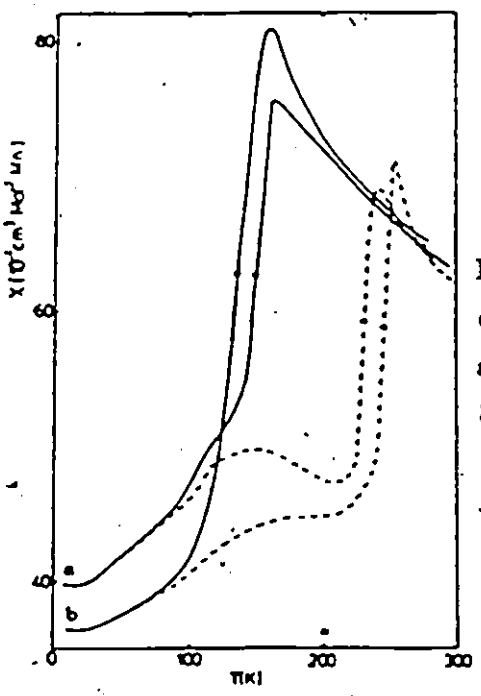

Fig. 6.2. Magnetic susceptibility of δ-MnSe as a function of temperature with an applied field of 8.61 kOe; (a) 1st temperature cycle, (b) 5th temperature cycle. (H. van der Heide Ref.8,17)

6.2) to the interference of two terms: the decreasing paramagnetic susceptibility of the cubic phase and the increasing susceptibility of the antiferromagnetically ordered hexagonal phase. Van der Heide also carried out experiments on the solid solution $Mn_{1-x}Mg_xSe$ ($0 < x < 0.25$). He found that the phase transformation is strongly hampered by the substitution of manganese by magnesium, indicated by a gradual shrinkage of the hysteresis loop in the magnetic susceptibility; for $x > 15$ the transformation has stopped completely as indicated by the disappearance of the anomalies and hysteresis.

In our work, we carried out temperature dependent magnetic susceptibility and electron spin resonance experiments on those single-phase samples with NaCl structure in our diagram, and which are "derived" from MnSe by substituting the Mn and/or Se atoms by Cd and/or Te atoms respectively (the limit of the solid solubility is indicated in Chapter 2). This was done in an attempt to investigate some of the magnetic properties of these alloys, and the dependence of these properties on the composition.

6.2 Experimental procedures and results

The experimental procedures for the susceptibility and ESR measurements are identical to those described in Chapters 3 and 4 respectively. However, in this case, the susceptibility was measured in a warming and then cooling run. Each sample was first precooled in zero-field down to liquid helium temperature (~4.2 K); then, the warming process measurements were performed up to a temperature $T \sim 270$ K. Afterwords, from this temperature the cooling process was

started and proceeded in the presence of the magnetic field; in other words it was a field-cooled situation, the implications of which will be discussed later.

The results of the susceptibility measurements are shown in Figs. 6.3, 6.6, 6.10, and 6.11. Fig. 6.6 shows χ vs T curves for the alloys with y = 1 and z = 0.85, 0.90, 0.95 and 1 (the latter is MnSe). Fig. 6.10 shows χ vs T curves for the alloys with z = 1 and y = 0.9, 0.8, 0.7 and 0.6. Finally, Fig. 6.11 shows χ vs T curves for the samples with y = 0.9, z = 0.9 and 0.95, y = 0.8, z = 0.95. The results of the electron spin resonance measurements are shown in Figs. 6.8(a)-(d).

6.3 Analysis and Discussion

6.3.1 MnSe

Considering first the result of the MnSe magnetic susceptibility shown in Fig. 6.3, as seen χ exhibits a large thermal hysteresis in a wide temperature range, which is in agreement with previous observations [4,8,10,17]. Our results are very similar to those obtained by Van der Heide [8,17] (which are shown in Fig. 6.2 for the purpose of comparison). However the features of the anomalies in our χ vs T curves are sharper than those in Van der Heide curve. We think that this is due to the fact that a small applied magnetic field (~30 gauss) is used in our case, compared to 8.61 K Gauss used by Van der Heide, which probably rounded the anomalies off.

In the warming run, starting from 4.2 K, the susceptibility increases at a very small rate with increasing temperature. At

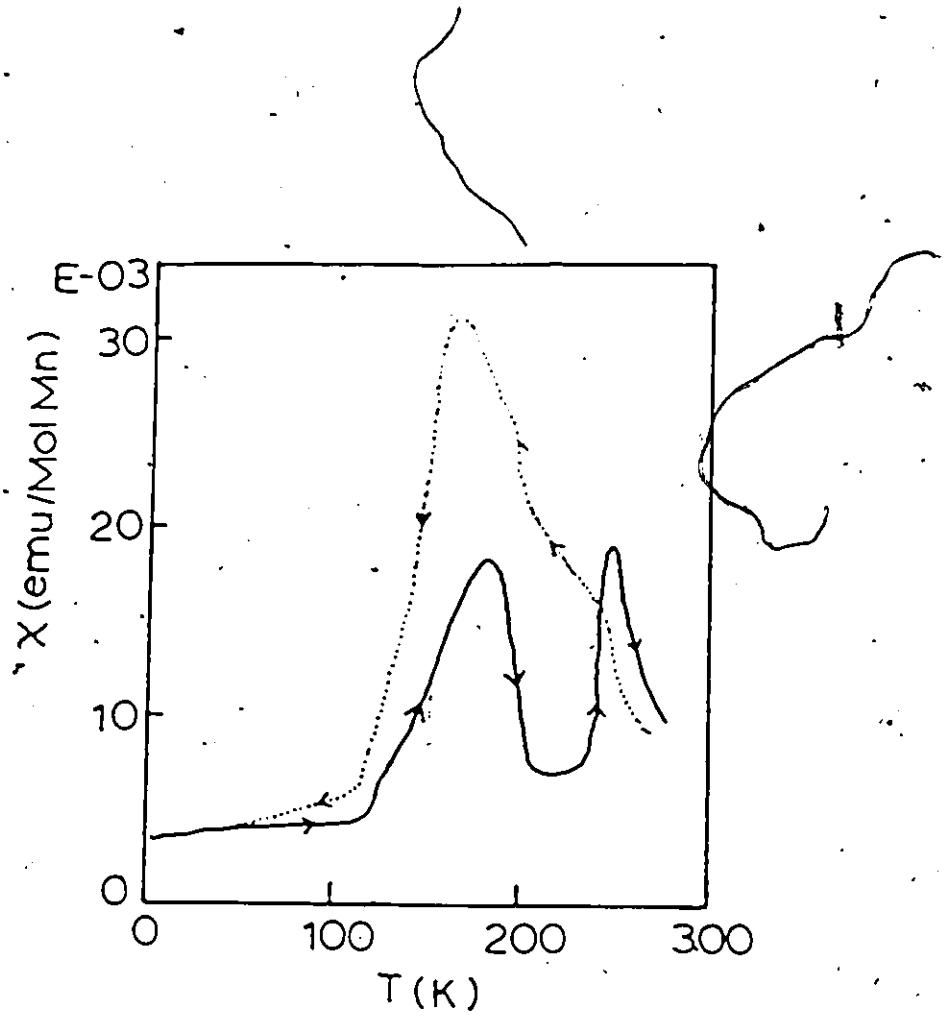

Fig. 6.3. Low-field magnetic susceptibility of δ-MnSe as a function of temperature.

——— Heating run

..... Cooling run

T ~ 118 K a break occurs in the curve of the susceptibility which starts to increase sharply and reaches a maximum at about T ~ 180 K; the change in χ between T ~ 118 K and T ~ 180 K is of the order of 14×10^{-3} emu/(mole Mn) which is a large change in less than 65 K temperature range. Afterwords, χ falls sharply and go through a minimum and starts to increase again in a sharper fashion and reaches another sharp maximum at T ~ 245 K and after that it falls back heading toward lower values. However, our measurements stop at T ~ 275 K. According to previous investigations [4,10] the hysteresis ends at about room temperature above which χ will follow the Curie-Weiss law.

The cooling process starts from T ~ 275 K; the susceptibility starts with slightly lower values than those of the warming run. However, χ increases at a fast rate and reaches a maximum at T ~ 170 K far above all other warming run values. Then χ decreases at a very sharp rate down to about T ~ 117 K where again a break occurs and the rate of decrease of χ becomes much slower, and finally the cooling run curve joins the warming run curve. It is worth noting that the difference: $\chi(T \sim 170\ K) - \chi(T \sim 117\ K)$ is of the order of 26×10^{-3} emu/(mole Mn).

As we indicated earlier the anomalies and hysteresis exhibited by the δ-MnSe susceptibility has been attributed as due to an incomplete phase transformation from cubic-NaCl structure to hexagonal-NiAs structure, that occurs in this compound in the lower temperatures region. As a matter of fact, Van der Heide has shown, from temperature dependent: x-ray diffraction, neutron diffraction and Mossbauer effect experiments [17], that the temperature at which χ

peaks (T_M ~ 170 K) in the cooling process, is associated with this structural phase transition, rather than with a simple paramagnetic-antiferromagnetic transition; furthermore, the Mn spins in the hexagonal-NiAs phase are antiferromagnetically aligned. Also, this transformation seems to stop when a temperature of approximately 120 K is reached upon cooling. We note that this temperature is in the same region where a sharp break occurs in the susceptibility curve. As indicated earlier, in the warming process two maxima are observed in χ vs T curve. Van der Heide has shown that the sharp maximum observed at about 245 K corresponds to the onset of the back transformation of the hexagonal phase into the cubic phase, and this reverse transformation is complete at T ~ 260 K. Also, Van der Heide has attributed the broad maximum that is observed at about 150 K in his case (Fig. 6.2), to the interference of two terms: the decreasing paramagnetic susceptibility of the cubic phase and the increasing susceptibility of the antiferromagnetically ordered hexagonal phase. While this interpretation seems to be plausible in Van der Heide case where the 150 K maximum is very broad and low, it is hard to accept it as the answer in our case, where the maximum is very sharp and high (χ reaches a value of 18×10^{-3} emu/(mole Mn) at T ~ 180 K, compared to a value of about 5×10^{-3} emu/(mole Mn) at T ~ 150 K in Van der Heide case). Such a steep increase after a sharp break in our susceptibility curve (warming run, Fig. 6.3) followed by such a sharp decrease in χ, cannot be thought of as due only to the interference of two susceptibility terms as indicated above. Adding a decreasing paramagnet susceptibility to an increasing antiferromagnet susceptibility, never

can give a resultant curve similar to the one we obtained.

As we mentioned earlier, Van der Heide has established that the ordering temperature T_N of cubic-NaCl-phase of MnSe is about ~115 K. Note that this is about the same temperature at which (the earlier mentioned) sharp break is observed to occur in our MnSe χ vs T curve in both runs, cooling and warming.

From the Mössbauer spectra obtained in the heating process, and for the temperature range of 160 to 220 K, Van der Heide observed, aside from the paramagnetic cubic and antiferromagnetic hexagonal spectra, an additional magnetic spectrum which was attributed to the presence of a second and intermediate type of cation sites in the hexagonal phase. In other words, in addition to the octohedral coordination of cations (which is the normal coordination of cations in the NiAs-type hexagonal structure), a second type of cations coordination exists, which may possibly be tetrahedral or trigonal prismatic as we shall see below. These intermediate cation sites (as called by Van der Heide) start to be occupied above T ~ 120 K where they grow in number at the expense of the regular cations of both the cubic and hexagonal phases, and reach about 23% of the total cations number at ~160 K. Concomitant with the back transformation of the hexagonal phase to the cubic phase (at T ~ 245 K), the occupation of these intermediate cation sites is reduced to zero.

Using the concepts of dislocation theory, Van der Heide has presented two possible schemes for the formation of lamella of NiAs-type phase in the NaCl-type phase.

In the first scheme, the plane-glide direction is determined

by the cations, as a result a single shear movement in a cations layer generates the formation of lamella of NiAs phase with the formation of staking faults with cations in the interstices of trigonal prismatic anions arrangements. This scheme is in agreement with the conclusion obtained from the electron microscopy studies carried out by Van der Heide. However, with this proposed arrangement other difficulties arises; Van der Heide explains that very few of these trigonal prismatic sites can occur and consequently cannot account for the large number of intermediate cation sites observed in the analysis of the Mössbauer spectra; furthermore, Mn^{2+} in a trigonal prismatic coordination is very unlikely and high energy state for Mn^{2+}.

In the second scheme, Van der Heide assumes that the glide direction is determined by the anions, a shear in every other anion layer (of NaCl-type fcc) would generate a hexagonal phase with large number of tetrahedral sites. By an independent shear motion of some of those cations residing in a tetrahedral environment, large lamella of NiAs-type could be formed also. Van der Heide points out that a tetrahedral coordination is more likely for Mn^{2+} as indicated by the existance of MnS and MnSe crystal with tetrahedrally coordinated Mn^{2+} (wurtzite and zinc blende structure). This also could explain the presence of the intermediate cation sites in the hexagonal phase. The ions generated at tetrahedral sites are transferred only gradually to the more stable octohedral sites. However, this explanation is apparently in contradiction with Van der Heide's analysis of the electron microscopy experiments (for more details see Ref. 17).

Whether the intermediate cation sites are due to Mn^{2+} ions in

trigonal prismatic coordination or in tetrahedral coordination, the coexistence of these intermediate sites with the regular cation sites (Mn^{2+} in octohedral environment) in the hexagonal phase, can possibly give rise to slightly different effective atomic moment for the Mn^{2+} ions in the magnetically ordered state, which can result in a net magnetic moment and hence a ferrimagnetic-like behaviour which can give rise to large values for the magnetic susceptibility. This may be a more probable explanation for the presence of the high maximum observed at ~180 K in our χ vs T curve of the warming cycle (Fig. 6.3).

As we mentioned earlier, we carried out ESR experiments on MnSe, and the results of the linewidth variation with temperature in a cooling and then warming process are shown in Fig. 6.4. No significant hysteresis or any anomalies were observed in ΔH vs T curve, and the results of both the cooling and warming runs were almost the same. As seen from Fig. 6.4, the general behaviour of the ΔH vs T curve is similar to that of typical antiferromagnetic materials above the Neel temperature T_N (in other words in the paramagnetic region) (see Ref. 6); ΔH increases monotonically with decreasing temperature, then this increase becomes more rapid when the temperature becomes close to T_N where the linewidth diverges. From our observation ΔH diverges at T ~ 120 K in the case of δ-MnSe.

In contrary to ΔH vs T curve, the intensity of the ESR line (the peak to peak amplitude for the derivative of the absorption line) shows a temperature hysteresis loop as illustrated in Fig. 6.5. In the cooling process, the relative intensity I decreases toward lower temperatures and shows a faster decrease at T ~ 180 K. I continues to

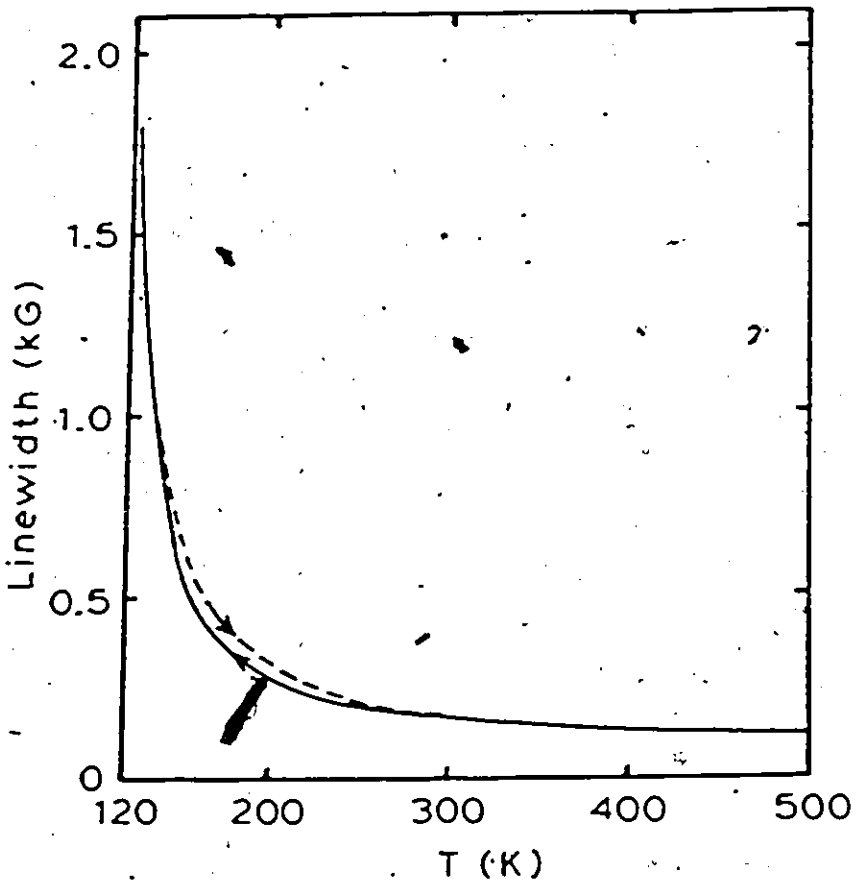

Fig. 6.4. Temperature dependence of the ESR linewidth for MnSe.
—— Cooling run
---- Heating run

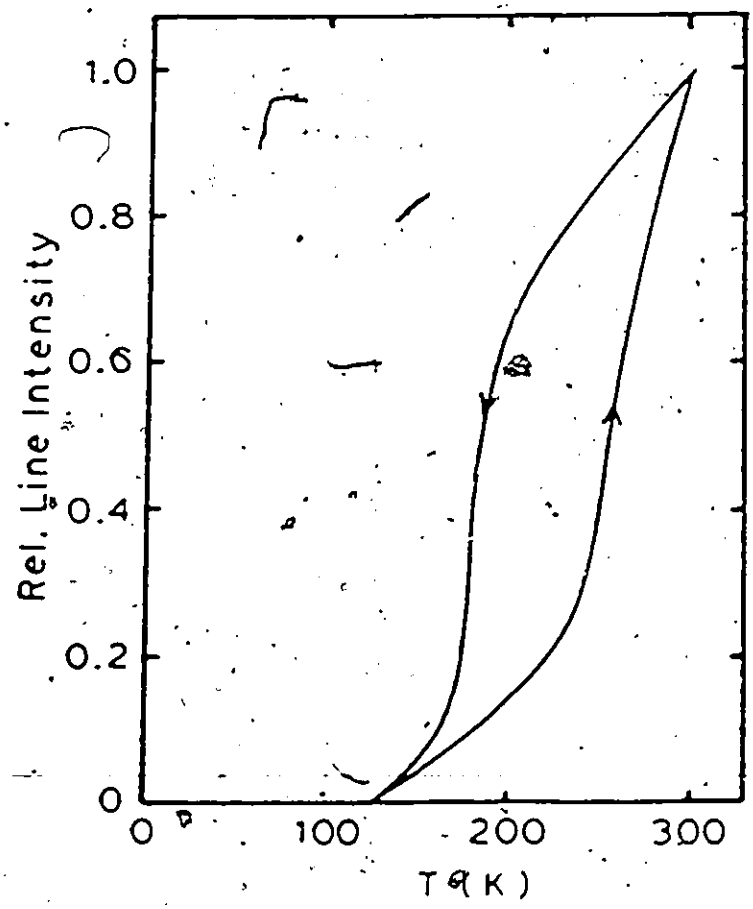

Fig. 6.5. Hysteresis effect in the temperature dependence of the ESR line intensity for MnSe.

decrease at a slower rate below ~150 K and disappears at ~120 K. In the warming process, I is smaller than that in the cooling process over the whole range of temperature, so a large hysteresis loop appears in the I vs T curve. Also, in the warming process, I increases slowly toward higher temperatures up to T ~ 240 K above which I increases at a higher rate, heading toward the values of the cooling process.

These ESR results for δ-MnSe are in agreement with those obtained by L. Maxwell et al [6], and more recently by Y. Watanabe et al [9]. These results can be very well interpreted on the basis of the partial phase transition of δ-MnSe from cubic to hexagonal mentioned earlier. Considering first the cooling cycle, when the MnSe specimen is in the high temperature region (T > 200 K).. The specimen is single-phase with the cubic-NaCl structure, hence the ESR line observed is due to the Mn^{2+} ions which are all in a paramagnetic state in the cubic phase. While lowering the temperature the ESR linewidth slowly increases as expected and the line intensity decreases as a result of the broadening of the line. However, when T reaches about 180 K, the partial structure phase transition begins, and as a result a number of the Mn^{2+} ions become part of the new hexagonal-NiAs phase where they are antiferromagnetically ordered. Consequently these Mn^{2+} ions can no longer contribute to the paramagnetic resonance so that the intensity of the ESR line falls sharply. In this case, the observed ESR line is due only to those Mn^{2+} ions which are still in the cubic phase interacting in a paramagnetic fashion. Consequently the linewidth should continue its normal temperature dependence without being affected by the partial phase transformation, and that what is actually

observed. When the temperature reaches ~120 K the ESR linewidth diverges and the intensity vanishes indicating that the Neel temperature of the cubic-NaCl phase has been attained (Fig. 6.4,5). In the heating run, the ESR line does not appear until T ~ 120 K; the variation of the linewidth practically follows the same path as that of the cooling run. However, the intensity of the line remains lower than in the cooling run while increasing at a slow rate; and that because in this temperature region (120 K > T > 240 K), parts of the specimen are in the hexagonal phase where the Mn^{2+} ions are in the antiferromagnetic state and hence do not contribute to the ESR; the only contribution arises from those Mn^{2+} ions in the cubic paramagnetic phase. Once the back phase transformation (from hexagonal to cubic) begins at T ~ 240 K, the line intensity increases at a faster rate and eventually it will join the curve of the cooling process at around room temperature (Fig. 6.5) where the entire specimen will be again single-phase with the cubic-NaCl structure.

6.3.2 Solid Solution $Cd_{1-z}Mn_zSe$ ($0.85 < z < 1$)

It has been reported that both the low temperature structural and magnetic behaviour of MnSe are strongly influenced by substituting a diamagnetic cation for manganese such as lethium or magnesium [8,17,18]. In our case cadmium is the substituting cation.

Solid solutions $Cd_{1-z}Mn_zSe$ crystallize in the NaCl structure for $0.85 < z < 1$ with the lattice parameter increasing with z decreasing (see Chap. 2 for more details). Magnetic susceptibility as well as ESR measurements were carried out on the alloys with z = 0.95, 0.9 and 0.85.

Comparing the MnSe susceptibility curve with the curve obtained for these alloys (cooling and warming) (Fig. 6.6) one can see that the curve of the alloy with z = 0.95 shows practically the same general features as that of MnSe but with a shrinkage in the hysterisis loop and a shift in the occurrence of the anomalies (maximums and breaks) towards lower temperatures. This can mean a decrease in the amount of NiAs phase appearing at the lower transition temperature, with the increase of the Cd content.

The two alloys with z = 0.9 and 0.85 show no temperature hysteresis or anomalies in their χ vs T curves. These, instead look very similar to the typical antiferromagnetic susceptibility curve of Fig. 6.1. All that indicates that the low temperature hexagonal phase is no longer formed for $z < 0.9$. Each of these two alloys shows one maximum in the cooling process as well as in the warming process at about the same temperature (Fig. 6.6), which we assume to be the Neel temperature (T_N) of the alloy. It is important to note that the observed hysteresis in this case, which is mostly below T_N arises from the different conditions in which the measurements of the warming and cooling processes were performed. As indicated earlier, each sample had been cooled first in zero-field down to ~4.2 K, then the warming process measurements were proceeded up to the highest temperature possible, from here the cooling process measurements were performed. The cooling this time had to be in presence of the magnetic field which causes the higher susceptibility values and hence the hysteresis which is present mostly below T_N. Also, χ shows a paramagnetic like increase at very low temperatures. All this seems to indicate the presence of a

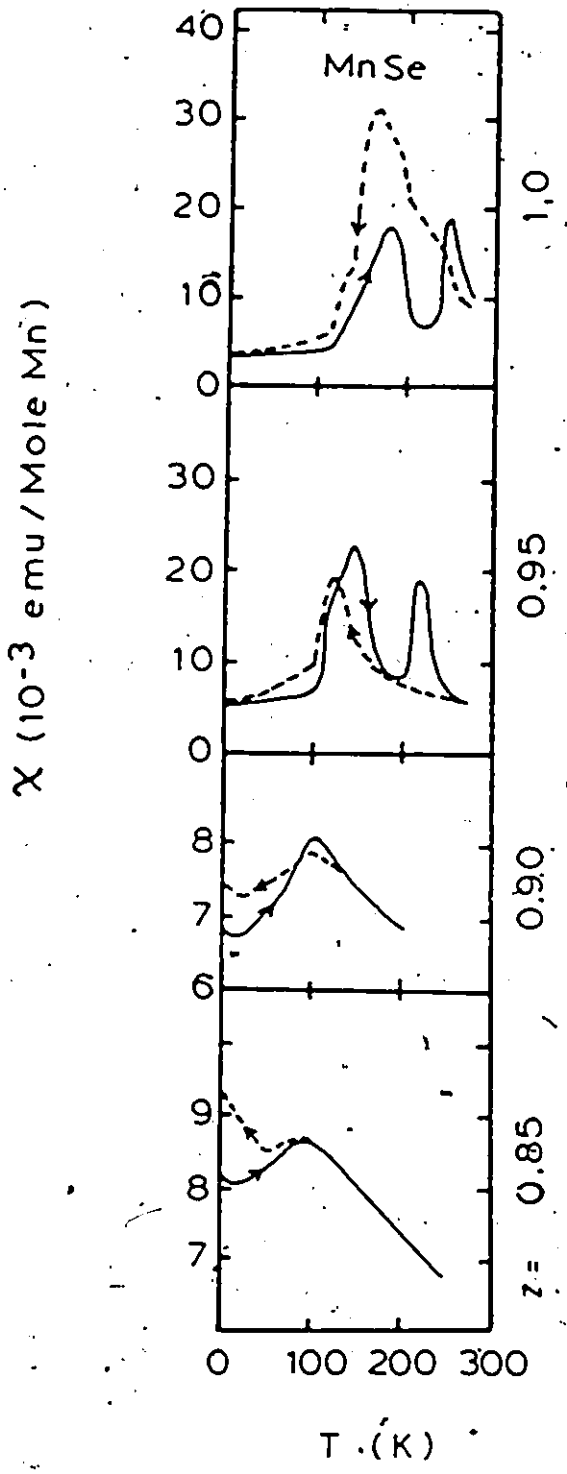

Fig. 6.6. Temperature dependence of the magnetic susceptibility for $Cd_{1-z}Mn_zSe$ alloys.

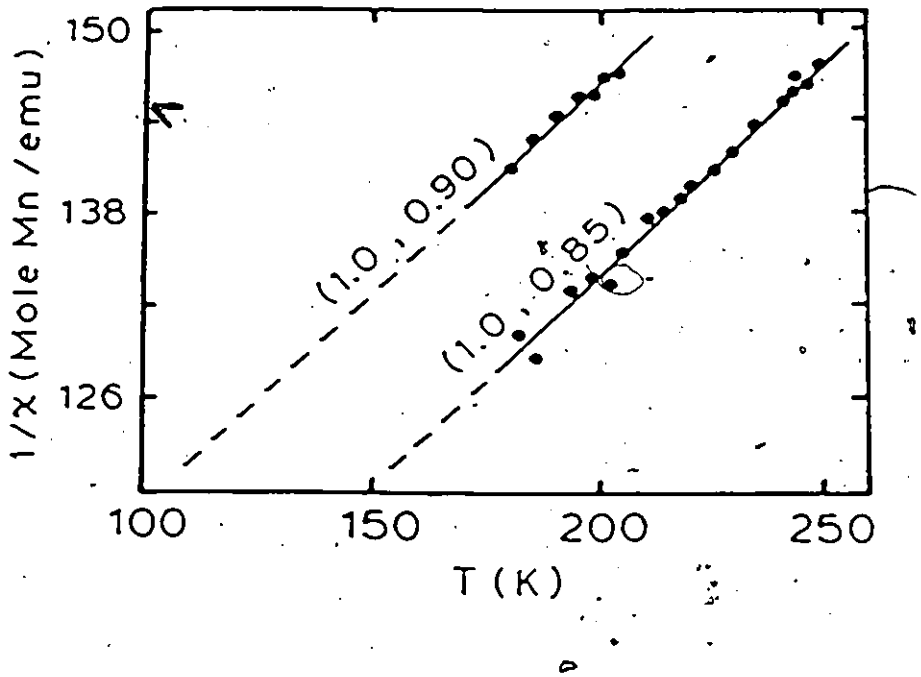

Fig. 6.7. Reciprocal susceptibility above the Néel temperature for the samples $Cd_{1-z}Mn_zSe$ with y = 1 and z = 0.90 and 0.85.

number of clusters of exchange-coupled Mn^{2+} ions and possibly some isolated spins, the effect of which on the susceptibility was discussed in more detail in Chapter 3 (see also Ref. 19).

By plotting the values of $1/\chi$ vs T, in the high temperatures region, for the two alloys with z = 0.9 and 0.85, a linear variation was found, in agreement with a Curie-Weiss behaviour ($1/\chi = \frac{(T-\theta)}{C}$). This is shown in Fig. 6.7 from the slope and the intercept one can obtain the values of the Curie constant C and the paramagnetic temperature θ respectively. The values of the latter are listed in Table 6.1 with θ values for the δ-MnSe reported in the literature. The value of C obtained is about 3.53 Mol. Mn/emu K which correspond to a value of $P_{eff} = 5.44\ \mu_B$. The value of P_{eff} is in fair agreement with the theoretical value of $P_{eff} = 5.92\ \mu_B$ for Mn^{2+}.

In Fig. 6.9(a) the values of the temperature T_M at which the susceptibility peaks in the cooling run are plotted against z. This plot does not convey a linear relation which is not unexpected. However, if one is to plot a straight line through the values of T_M for the two alloys with z = 0.9 and 0.85 which are assumed to remain in the cubic phase over the whole temperature range (i.e. $T_M = T_N$ the Neel temperature) (the molecular field theory and series expansion for a fcc [20] predict a linear dependence of T_N on z), this line extrapolates to T = 117 K at z = 1 (MnSe) which is in agreement with the value of T_N for the cubic phase of MnSe obtained by Van der Heide from neutron diffraction [17], as well as with that obtained from our ESR results.

Turning to the ESR, the linewidth dependence on temperature for all three alloys (z = 0.95, 0.9 and 0.85) is similar to that of

Table 6:1 Values of the Curie-Weiss paramagnetic temperature θ

Composition	-θ(K)
$Cd_{0.15}Mn_{0.85}Se$	283
$Cd_{0.1}M_{0.9}Se$	305
$Cd_{0.05}Mn_{0.95}Se$	
δ-MnSe	373 (a)
	366 (b)
	297 (c)
	347 (d)

[a] Ref. 10

[b] Ref. 36

[c] Ref. 37

[d] Ref. 38

MnSe, as seen in Fig. 6.8(b). The temperature at which ΔH diverges (T_N^{ESR}) shows a systematic dependence on the Mn concentration (Fig. 6.9(b)). It is important to note that T_N^{ESR} for the two alloys with z = 0.9 and 0.85 corresponds in each case to the temperature T_M at which the maximum occurs in χ vs T curve. This constitutes a further evidence that these two alloys behave like normal antifferomagnets i.e. no low temperature structural phase transition as in the case of MnSe.

6.3.3 Solid Solution $MnTe_{1-y}Se_y$ ($0.6 \leq y < 1$)

As it is shown in Chap. 2, the pseudo-binary alloys $MnTe_{1-y}Se_y$ crystallize in the cubic-NaCl structure in the range of y between 1 and 0.6. Magnetic susceptibility and ESR measurements were performed on the alloys with y = 0.9, 0.8, 0.7 and 0.6.

The χ vs T results are shown in Fig. 6.10. As it is seen, again, the susceptibility shows thermal hysteresis and anomalies which mean that these alloys also undergo at low temperatures, a partial structural phase transformation which is assumed to be from the cubic NaCl to hexagonal-NiAs. This is not unexpected since the MnTe actually has the NiAs structure. However, a close look at the details of the χ vs T curves of these alloys shows that these curves appear to be different from the MnSe susceptibility curve, specially in the warming process where instead of exhibiting two large maxima (as it is the case in MnSe and $Cd_{0.05}Mn_{0.95}Se$), the $MnTe_{1-y}Se_y$ alloys exhibit on large maximum and then a little kink at a higher temperature. These results are in a general agreement with the observations of Kamat Dalal et al [21]. These authors had carried out magnetic susceptibility

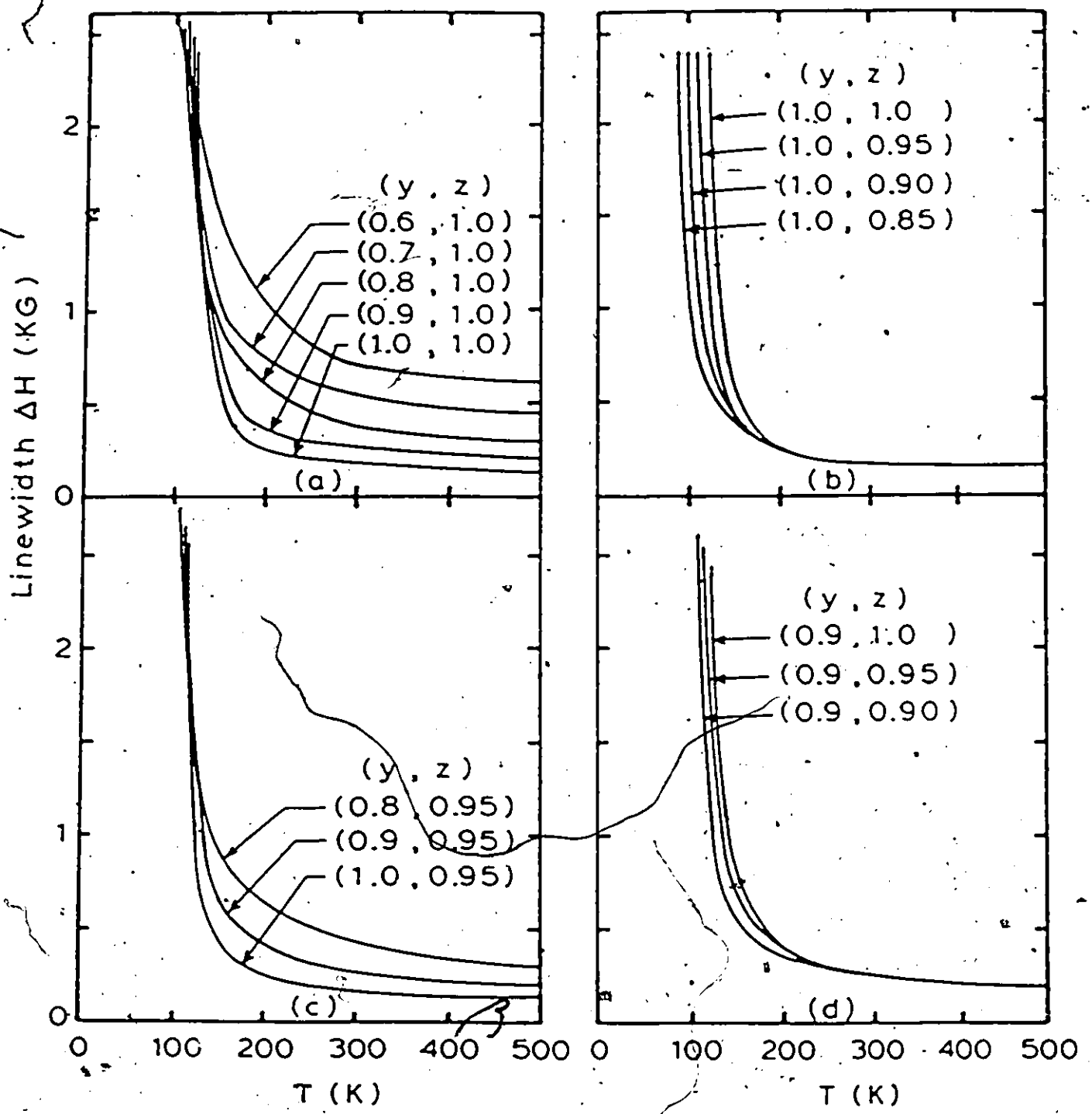

Fig. 6.8. Temperature dependence of the ESR linewidth for the δ phase alloys. (a) for the $MnTe_{1-y}Se_y$ edge, (b) for the $Cd_{1-z}Mn_zSe$ edge, (c) and (d) for sequences within the δ phase region.

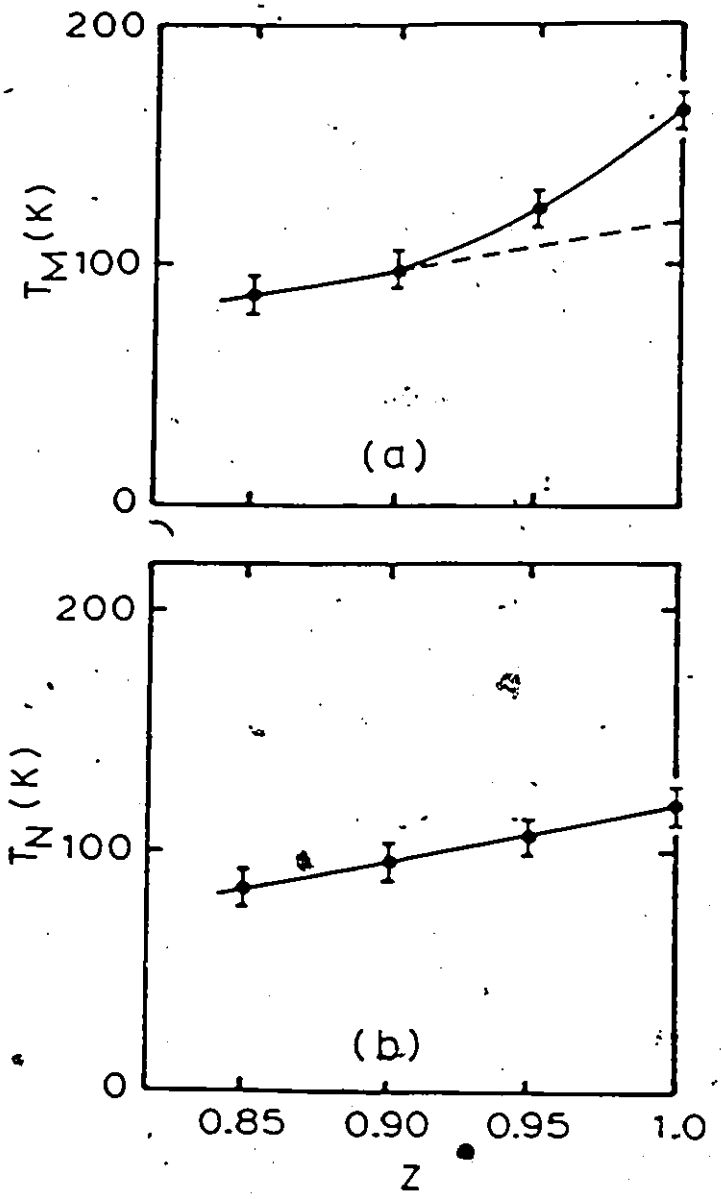

Fig. 6.9. (a) Concentration dependence of the temperature T_M (temperature at which the susceptibility peaks in the cooling run) for $Cd_{1-z}Mn_zSe$. The broken line is the extrapolation of the straight line drawn through the T_M values for z = 0.85 and 0.90. (b) Plot of the Néel temperature T_N values obtained from ESR results versus concentration z for $Cd_{1-z}Mn_zSe$.

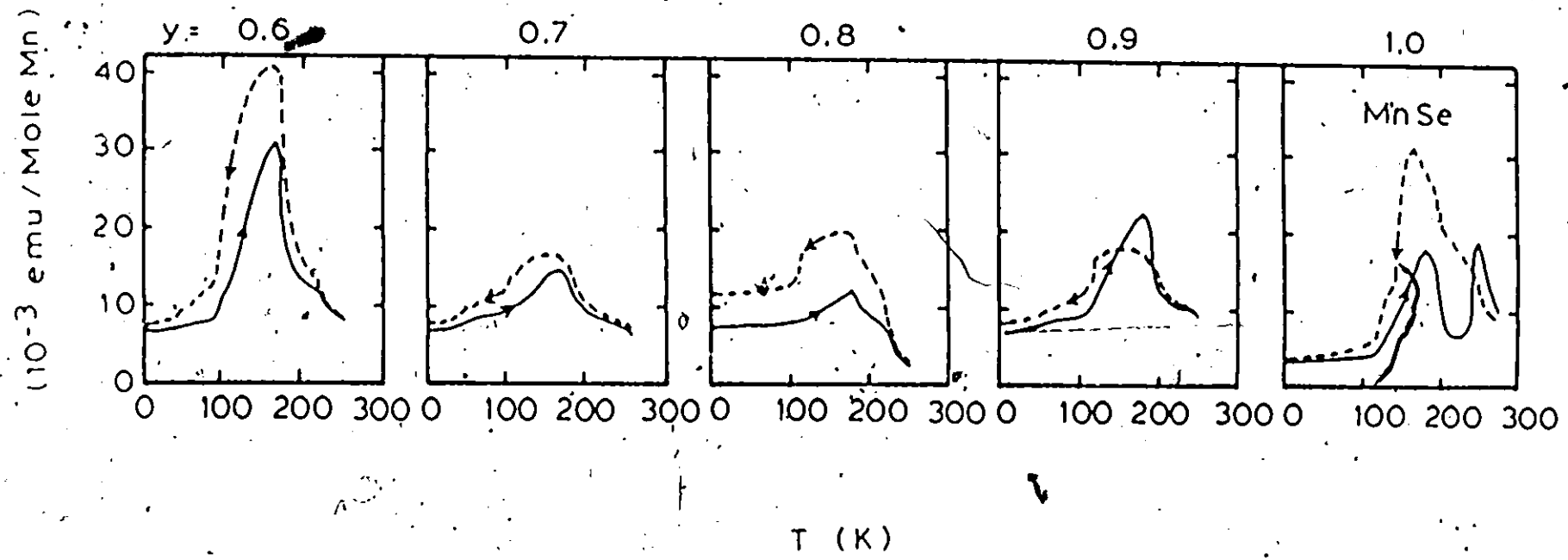

Fig. 6.10. Temperature dependence of the magnetic susceptibility for $MnTe_{1-y}Se_y$ alloys.

measurements on some alloys of the $MnTe_{1-y}Se_y$ system, in a warming process between ~78 K and 340 K. They observed two minima in the P/χ vs T plots for those alloys of the system which have the cubic-NaCl structure.

The ESR linewidth dependence on temperature of these alloys are similar to that of MnSe; the set of curves of ΔH vs T are shown in Fig. 6.8(a). It is seen that from the high temperature tails of these curves and for a given temperature, that ΔH increases when y decreases (between 1 and 0.6). This can mean that the exchange narrowing effect decreases when replacing selenium by tellerium. This is similar to a previous observation discussed in Chapter 4, (see Ch. 4 p. 92-93). On the other hand the values of T_N^{ESR}, the temperature at which ΔH diverges, show a slight decrease with y; this can also be correlated with the decrease in the exchange interaction parameters when y is decreased. The values of T_N^{ESR} are listed in Table 6.2.

6.3.4 The Quaternary Alloys $[Cd_{1-z}Mn_z][Te_{1-y}Se_y]$ $(0.85 < z < 1)$, $(0.6 < y < 1)$.

Magnetic susceptibility and electron spin resonance measurements were carried out on three quaternary alloys: $[Cd_{0.1}Mn_{0.9}][Te_{0.1}Se_{0.9}]$, $[Cd_{0.05}Mn_{0.95}][Te_{0.1}Se_{0.9}]$ and $[Cd_{0.05}Mn_{0.95}][Te_{0.2}Se_{0.8}]$, all of which have the cubic NaCl structure.

The χ vs T curves for all three alloys showed temperature hsyteresis and anomalies as can be seen from Fig. 6.11. Moreover, the warming process curves showed three peaks instead of two in the case of MnSe. A possible interpretation for the existence of a third peak is proposed as follows: These alloys exist in a single-phase field

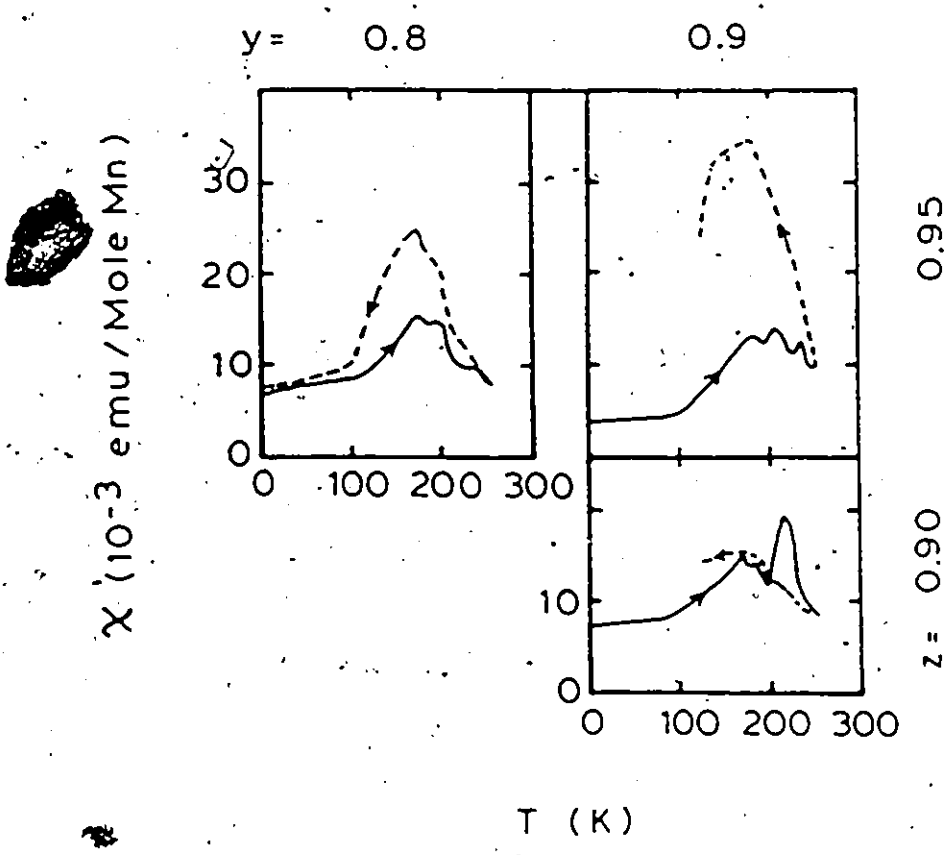

Fig. 6.11. Temperature dependence of the magnetic susceptibility for $Cd_{1-z}Mn_zTe_{1-y}Se_y$ alloys within the δ phase region.

(NaCℓ-type) which has common boundaries with two double-phase fields (see Chap. 2 Fig. 2.7); one consists of wurtzite phase plus NaCℓ-type phase, the other of zinc-blende phase plus NaCℓ-type phase. Therefore, it is possible that these alloys undergo another partial structural phase transformation from the cubic-NaCℓ phase to the wurtzite or to the zinc blende phase in the low temperature region, and that in addition to the original phase transformation from cubic-NaCℓ to hexagonal-NiAs.

Turning to ESR, theses three alloys show a linewidth dependence on temperature similar to that of MnSe. The ΔH vs T curves are shown in Figs. 6.8(c) and (d), and the T_N^{ESR} are listed in Table 6.2.

6.3.5 Analysis of the ESR Results

The ESR linewidth variation with temperature for all the alloys investigated, was found to be similar to that for MnSe compound. As we mentioned earlier, the ΔH vs T results of MnSe were found to be similar to those of a typical fcc antiferromagnetic material such as MnO or MnS [6,24]. Consequently, the experimental data of the variation of ΔH with T in all cases can be expressed in terms of the modified Huber equation [22,23]

$$\Delta H = A\left(\frac{T_N}{T-T_N}\right)^{\alpha} + B\left(1 - \frac{\theta}{T}\right) \qquad (6.1)$$

where A and B are empirical parameters, T_N is the Neel temperature (at which ΔH diverges), α a critical exponents and θ is the Curie-Weiss paramagnetic temperature (which is negative for antiferromagnets). Equation 6.1 applies to antiferromagnets above the Neel temperature

T_N. The first term represents the broadening of the ESR line as a result of the critical phenomenon when T approaches T_N from above; the second term represent the high temperature non-critical paramagentic dependence of ΔH on T (for $T > 3\ T_N$).

By fitting the experimental values of ΔH vs T to equation 6.1, values of the parameters θ, B, α and A were obtained for all the investigated samples. These values are shown in Table 6.2.

The fit was carried out using a graphical method which consisted of two main steps. The first step was to plot the values of T ΔH against T in the high temperature region ($T > 3\ T_N$), where any contribution to the linewidth arises only from the term $B(1-\frac{\theta}{T})$ (since $A(\frac{T_N}{T-T_N})^{\alpha} = 0$ in this region). In this case $T\ \Delta H = B(T-\theta)$ is a linear relation from which B and θ could be determined (by determining the slope and the intercept). Once the values of these two parameters, were known, the value of $\Delta H_p = B(1 - \frac{\theta}{T})$ could be calculated for any value of T; hence the difference $\Delta H - \Delta H_p = \Delta H_c = A(\frac{T_N}{T-T_N})^{\alpha}$ could also be determined. Now by plotting the value of $\log(\Delta H_c)$ against $\log(\frac{T_N}{T-T_N})$, a linear variation was obtained and the values of α and log A(and hence A) could be found from the slope and the intercept respectively. Fig. 6.12 shows an example of this calculation method for MnSe.

The values of θ obtained from ESR for MnSe, $Cd_{0.1}Mn_{0.9}Se$ and $Cd_{0.15}Mn_{0.85}Se$ (as listed in Table 6.2) are to be compared with those obtained from magnetic susceptibility which are listed in Table 6.1.

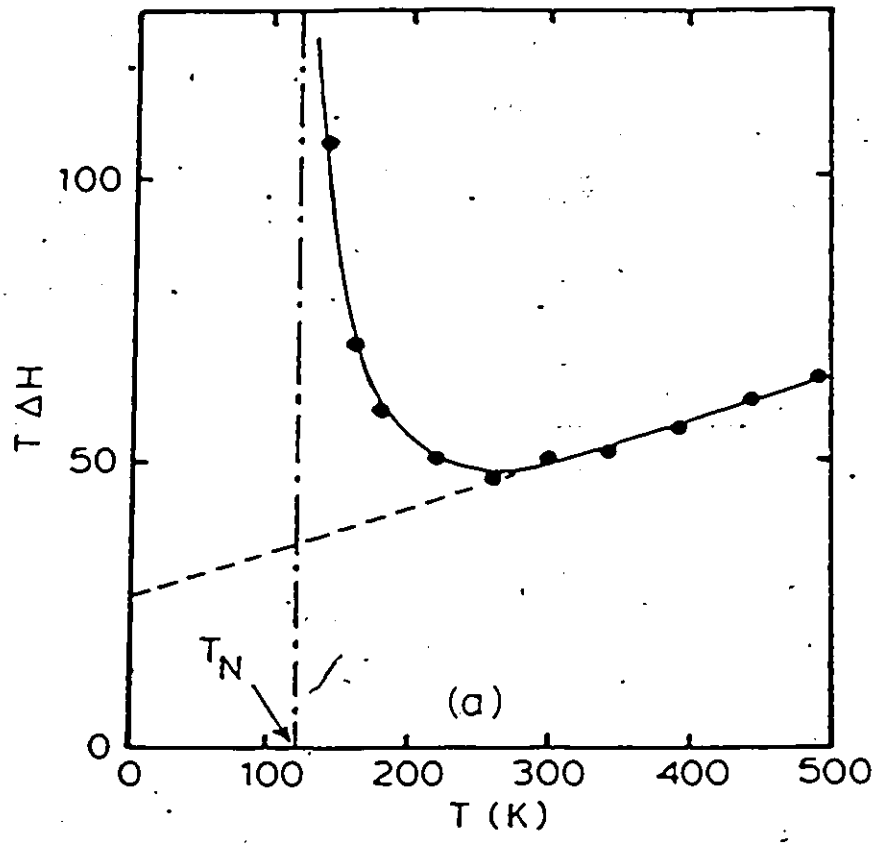

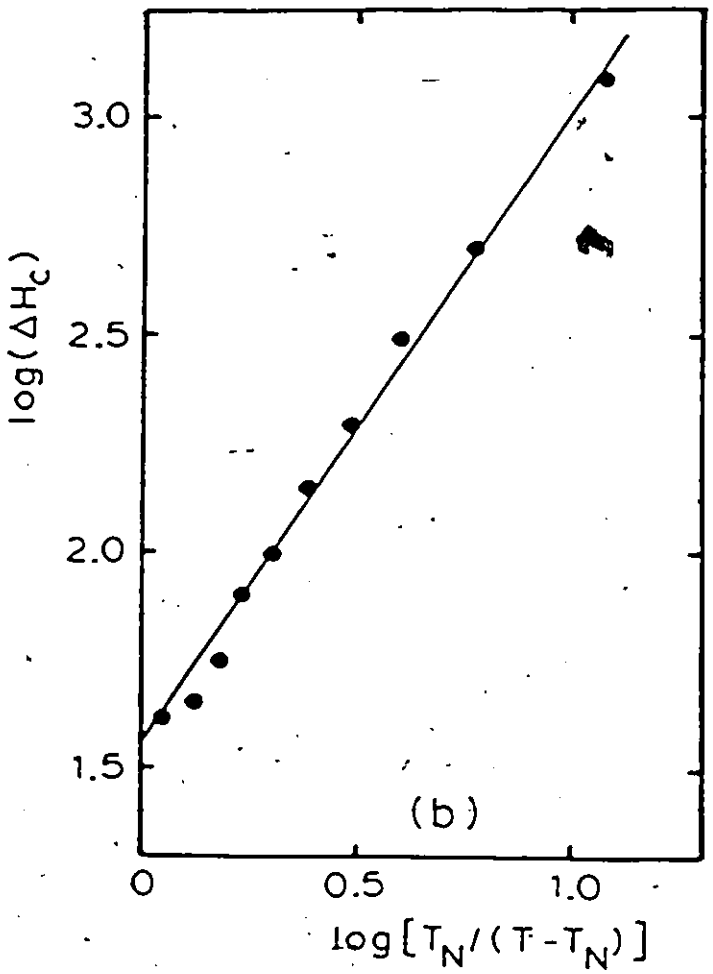

Fig. 6.12. Graphical method of fitting Equ. 6.1 to the ΔH vs T curves. The case of MnSe is shown in the figure.
(a) Plot of the second term of Equ. 6.1 and
(b) plot of the first term of Equ. 6.1.

Table 6.2 Values as a function of composition of the parameter from Equ. 6.1.

Composition	T_N^{ESR}(K)	$-\theta$(K)	B(gauss)	A(gauss)	α
$Cd_{0.15}Mn_{0.85}Se$	86	285	86	101	1.11
$Cd_{0.1}Mn_{0.9}Se$	98	306	85	53	1.39
$Cd_{0.05}Mn_{0.95}Se$	106	319	84	39	1.50
MnSe	120	343	76	37	1.44
	120	-	90	-	1.1 (a)
	119	-	176	63	1.4 (b)
$MnTe_{0.1}Se_{0.9}$	117	295	125	35	1.3
$MnTe_{0.2}Se_{0.8}$	112	270	188	78	1.25
$MnTe_{0.3}Se_{0.7}$	107	227	300	80	1.33
$MnTe_{0.4}Se_{0.6}$	103	182	440	170	1.18
$Cd_{0.1}Mn_{0.9}Te_{0.1}Se_{0.9}$	95	244	135	79	1.51
$Cd_{0.05}Mn_{0.95}Te_{0.1}Se_{0.9}$	107	260	128	64	1.56
$Cd_{0.05}Mn_{0,95}Te_{0.2}Se_{0.8}$	100	210	207	170	1.32

[a] Ref. 9

[b] Ref. 17

The two sets of values seem to be in a good agreement with one another. On the other hand, the values of θ along the $MnTe_{1-y}Se_y$ edge seem to decrease as y decreases i.e. when replacing Se by Te, which is in agreement with what is mentioned earlier about the decrease in the exchange interaction effect as y is decreased, since θ is a measure of this exchange interaction. We note that the θ values of the $MnTe_{1-y}Se_y$ alloys, with the NaCl-type cubic structure, do not extrapolate to the MnTe θ value of -584 K [38], at y = 0. This can be attributed to the fact that MnTe has the NiAs-type hexagonal structure which is quite different from the NaCl-type cubic structure.

Knowing the values of θ and T_N and assuming the same uniaxial type-II spin arrangement in every case. The exchange parameters J_1 and J_2 for the nearest and next nearest neighbour respectively can be estimated. The exchange parameters J_1 and J_2 were determined with the method used by Lines and Jones [25-28], in which Lines' Green's-function theory was used to describe the paramagnetic properties [27], where this theory has proved to be more accurate than the molecular field theory [25]. Table 6.3 shows the values of J_1 and J_2 obtained for the sequence $MnTe_{1-y}Se_y$ ($0.6 \leq y \leq 1$) where the Mn atoms occupy all the sites of the fcc unit cell; also, we list the values of J_1 and J_2 reported in the literature for the compounds δ-MnSe, δ-MnS and MnO. In all the cases, the 180° cation-anion-cation superexchange parameter $|J_2|$ is larger than the 90° superexchange parameter $|J_1|$ in agreement with theory [27,34].

The values of the critical exponent α in all the cases are found to be between ~1.1 and 1.6 (see Table 6.2). These values are not

Table 6.3 Lattice parameter and exchange interaction parameters values.

Composition	Lattice parameters(^{o}A)	$-J_1$(K)	$-J_2$(K)
$MnTe_{0.4}Se_{0.6}$	5.632	1.1	8.2
$MnTe_{0.3}Se_{0.7}$	5.582	2.2	8.6
$MnTe_{0.2}Se_{0.8}$	5.537	3.2	9.1
$MnTe_{0.1}Se_{0.9}$	5.493	3.7	9.6
δ-MnSe	5.462	4.8	10
		6.9	9.8←(a)
δ-MnS	5.223	7.0	12.5←(b)
		7.4	12.2←(c)
MnO	4.444	10	11←(d)

[a] Ref. 17

[b] Ref. 26

[c] Ref. 19

[d] Ref. 25

very different from the value found for the critical line broadening near the Neel temperature of the antiferromagnet MnF_2, $\alpha = 1.2$ [29]. It is worth noting that Kawasaki [30] has predicted a value of 1.5 for the critical exponent characterizing the ESR linewidth in antiferromagnets; also Huber [22] indicated that the α value for MnO and MnS (to which MnSe has very similar ESR behaviour) should not be very much different from the value of 1.25 which he predicted for MnF_2.

6.4 Conclusion

This study has shed a little more light on the complicated behaviour of MnSe, which can be interpreted in terms of an incomplete transformation to a hexagonal structure. The occurrence of such a transformation should not be surprising, knowing that MnSe is intermediate between MnS and MnTe (in the manganese chalcogenides MnX, with X = S, Se, Te). MnTe exist below 1050 C in the NiAs-type structure [31]; also, stable form of MnS at room temperature is NaCl-type structure. Franzen [32] has pointed out that the NiAs-type stucture is found in compounds where the non-metal atoms possess easily accessible d-orbitals. Further more, Hutsman et al [33] has concluded that for central atoms with d^0 configuration (e.g. the non-metal atoms in NiAs-type structure), the trigonal prismatic coordination, found in the NiAs-type structures, may be more stable than the octohedral one, found in NaCl-type structure. Therefore, according to Van der Heide [17], the low temperature transformation of MnSe can be ascribed to the fact that in selenium the d-orbitals are not occupied.

In this work, the magnetic susceptibility and electron spin resonance of the MnSe compound and the $(Cd_{1-z}Mn_z)(Te_{1-y}Se_y)$ alloys with the same phase as MnSe are investigated. The χ vs T curves in most cases show thermal hysteresis and anomalies resulting from low temperature partial phase transformation. In the case of $Cd_{1-z}Mn_zSe$ series ($0.85 < z < 1$), the experiments show that the phase transformation is strongly influenced by the substitution of Mn by Cd; for $z < 0.9$ the transformation has stopped completely, as indicated by the disappearance of the anomalies and temperature hysteresis in χ vs T curves.

A suggestion is put forward in an attempt to interpret the existence of the first large maximum observed in the warming run of the MnSe susceptibility curve; we think that a ferrimagnetic-like behaviour resulting from the presence of Mn^{2+} ions in two different types of sites in the hexagonal phase, is causing this maximum.

The ESR experiment show that the linewidth dependence on temperature for all the alloys is similar to that of MnSe where no significant thermal hysteresis is observed; however, hysteresis is observed in the intensity of the absorption. This was interpreted on the basis of the low temperature phase transition. In each case, the Neel temperature is estimated from the temperature at which the linewidth diverges and line-intensity vanishes simultaneously.

The ΔH vs T curves are fitted to a modified Huber's expression (Equ. 6.1); as a result all the relevant parameters are determined such as the paramagnetic temperature θ and the critical exponent α (Table 6.2). The latter are found to agree with theoretically predicted values.

Knowing the values of θ and T_N, values of J_1 and J_2 the first and second nearest neighbour exchange interaction parameters, are estimated. $|J_2|$ is found to be greater than $|J_1|$ in every case, which is consistent with the theory of superexchange.

REFERENCES

1. C.G. Shull, W.A. Strauser, E.O. Wollan, Phys. Rev. 83, 333 (1951).
2. C.F. Squire, Phys. Rev. 56, 922 (1939).
3. H. Bizitte, B. Tsai, Compt. Rend. 212, 75 (1941).
4. R. Lindsay, Phys. Rev. 84, 569 (1951).
5. W. Palmer, J. Appl. Phys. 25, 125 (1954).
6. L.R. Maxwell, T.R. McGuire, Rev. Modern Phys. 25, 279 (1953).
7. K.K. Kelley, J. Am. Chem. Soc. 61, 203 (1939).
8. H. Van der Heide, J.P. Sanchez and C.F. Bruggen, J. Mag. Mag. Mat. 15-18, 1157 (1980).
9. Y. Wanatabe, S. Saito, T. Ito, K. Ito and M. Oka, Jpn. J. Appl. Phys. 18, 1875 (1979).
10. T. Ito, K. Ito and M. Oka, Jpn. J. Appl. Phys. 17, 371 (1978).
11. H. Van der Heide, C.F. Bruggen and C. Hass, Mat. Rev. Bull. 18, 1515 (1983).
12. Y. Wanatabe, J. Takeuchi and M. Oka, Phys. Stat. Sol. (a) 76, K13 (1983).
13. A. Taylor, Appl. Spect. 14, 116 (1960).
14. L. Cemic, A. Neuchaus, High Temp. and High Press. 4, 97 (1972).
15. A.F. Andersson, H. Rotteruo, Acta Cryst. A25, S250 (1969).
16. A.J. Jacobson, B.E.F. Fender, J. Chem. Phys. 52, 4563 (1970).
17. H. Van der Heide, Ph.D. Thesis, University of Groningen, The Netherland (1982).
18. S.J. Pickart, R. Nathass, G. Shirane, Phys. Rev. 121 707 (1964).

19. H.H. Heikens, R.S. Kuindersma, C.F. Van Bruggen and C. Haas, J. Magn. Magn. Mat. 8, 130 (1978).

20. G.S. Rushbrooke, "Critical Phenomenon in Alloys, Metals and Superconductors" ed's R.E. Mills, E. Asher, R.I. Yaffe, McGraw-Hill, New York (1971).

21. V.N. Kamat Dalal, H.V. Keer, and A.B. Biswas, Nuclear Physics and Solid State Physics Symposium abstract, only. Bombey India 1 Feb. 1972 p. 633.

22. D.L. Huber, Phys. Rev. B6, 3180 (1976).

23. E. Dormann and V. Jaccarino, Phys. Letters, 48A, 81 (1974).

24. J.W. Battles, J. Appl. Phys. 42, 1286 (1971).

25. M.E. Lines and E.D. Jones, Phys. Rev. 139, A1313 (1965).

26. M.E. Lines and E.D. Jones, Phys. Rev. 141, 525 (1966).

27. M.E. Lines, Phys. Rev. 134, A1304 (1965).

28. M.E. Lines, Phys. Rev. B5, A1336 (1964).

29. M.S. Sheera, T.G. Castner jr. Solid State Comm. 8, 787 (1970).

30. K. Kawasaki, Phys. Letters 26A, 543 (1968).

31. W.D. Johnston, D.E. Sestrick, J. Inorg. Nucl. Chem. 19, 229 (1961).

32. H.F. Frenzen, J. Inorg. Nucl. Chem. 28, 1575 (1966).

33. R. Huisman, R.D. Jonge, C. Haas, F. Jellinek, J. Solid State Chem. 3, 56 (1971).

34. A.H. Morrish, "The Physical Principal of Mangetism", R.E. Kinger publishing company inc. 1980 p. 464.

35. J.B. Goodenough, "Mangetism and the Chemical Band", Robert E. Krieger publishing company, New York (1976).

36. R. MacLaren, B.C. Forbes and R.D. Heyding, Canadian Journal of Chemistry, vol. 50, 4059 (1972).

37. J.J. Banewicz, R.F. Heideilberg and A.H. Luxem, J. Phys. Chem. 65, 615 (1961).

38. A. Serres, J. Phys. Radium, 8, 146 (1947).

Chapter 7

CONCLUSION

This thesis describes our investigations of some of the properties of the alloy system $(Cd_{1-z}Mn_z)(Te_{1-y}Se_y)$ which belongs to a new group of materials known as semimagnetic semiconductors. From a magnetic point of view, these materials have interesting properties as disordered magnetic alloys displaying, e.g. the spin glass transition, antiferromagnetically correlated spins in clusters and other magnetic effects of current interest.

The prior requirement of investigating the phase diagram of the alloy system, including the study of the lattice paramater dependence on composition and hence the determination of the single-phase fields, is indicated in Chapter 2. The boundaries of the single, two and three-phase fields which are displayed by the present system, were found to be very much dependent on the annealing temperature. Two isothermal sections of the phase diagram were determined.

Once the limits of solid solutions were defined we could next proceed to investigate the magnetic behaviour of the alloys. This was done by carrying out magnetic susceptibility and electron spin resonance experiments.

The magnetic susceptibility measurements carried out on the zinc blende and wurtzite single-phase sample, as described in Chapter 3, provided us with the spin-glass freezing temperature T_g the Curie-

Weiss paramagnetic temperature θ and the Curie constant C values and, thus, the dependence of these parameters on composition was also established. It was found that they depend mainly on the Mn concentration z. The interesting aspect about the T_g results, was that LnT_g was found to decrease in a linear fashion when the mean spacing between the Mn ions increases with decreasing z. This implied that the exchange interaction decreases exponentially with distance between the magnetic spins. An exchange mechanism proposed by Geertsma et al, involving virtual transitions from the valence band to Mn $3d^5$ levels was assumed as the one occurring in these wide gap semiconductors. Using the expression of this exchange (Equ. 3.7) in conjunction with the mean field theory we were able to predict values for J_1 and J_2, the nearest and next nearest neighbors exchange parameters, as well as values for the Curie-Weiss paramagnetic temperature θ. All these calculated values were found to agree very well with the experimental ones, which was a strong evidence in support of our assumption that the Geertsma exchange mechanism is very likely the one taking place.

The electron spin resonance experiments, described in Chapter 4, revealed other aspects of the magnetic behaviour of the present semimagnetic semiconductor alloys. The ESR line was found to broaden in a symmetric fashion down to a certain temperature below which the line became asymmetrically broadened. This was attributed to an uniaxially anisotropic g-value which, in turn, was attributed to the increasing degree of spins correlation in clusters. The linewidth dependence on temperature was fitted to an empirical equation (6.4)

expressing the fact that the ESR line is broadened by composition inhomogeneity. The parameters (B, T_o and Γ) values obtained from the fit showed consistent dependence on composition and, again, seemed to be mainly determined by the Mn concentration. With regard to the physical significance of these ESR parameters, as discussed in Chapter 6, B' represents the linewidth at the highest possible temperature, T_o is a measure of the potential barrier separating two neighbouring ground states of a disordered spin system, while Γ is determined by the variation in the magnetic environment of a Mn ion in the lattice.

Both the magnetic susceptibility and ESR results, were found to be consistent with the behaviour of a cluster-glass material.

From the optical properties point of view, the room temperature energy gap E_g and its dependence on composition was determined. This was performed using the wavelength modulated reflectance technique, as indicated in Chapter 5. E_g showed a linear increase when the Mn concentration is increased. Also E_g showed optical bowing behaviour when Se was replaced by Te (or vice versa).

Temperature dependent energy gap measurements carried out on the $Cd_{1-z}Mn_zSe$ edge, showed an increase in the energy gap values, when lowering T, larger than that normally obtained with a non-magnetic semiconductor. This was attributed to magnetic effects contribution to the energy gap, resulting from the presence of the Mn^{2+} spins. Other consequences of the presence of Mn, is the observed decrease in the valence band crystal-field and spin-orbit splittings when z was increased. The latter could be accounted for on the basis of Mn d-orbitals admixture with normal p-orbitals forming the valence band.

The fractional d-like character in the valence and its dependence on z were estimated.

In Chapter 6, magnetic properties of MnSe compound and of the single-phase alloys with cubic NaCl-type structure, were discussed. The thermal hysteresis and anomalies exhibited in the magnetic susceptibility of these materials was attributed to be due to a low temperature incomplete phase transformation to an antiferromagnetically ordered hexagonal NiAs-type structure. This phase transformation was found to be strongly influenced by the substitution of Mn by Cd, especially for $Cd_{1-z}Mn_zSe$ ($1 \leq z \leq 0.85$) alloys. From the ESR linewidth dependence on temperature, we were able to estimate the Neel temperature T_N values for the cubic phase of all concerned samples. Also by fitting the linewidth variation with T to a modified Huber's equation, we were able to evaluate the paramagnetic temperature θ and the critical exponent α which is associated the paramagnetic- antiferromagnetic phase transition occurring at T_N.

Finally, we strongly feel that this investigation of the $(Cd_{1-z}Mn_z)(Te_{1-y}Se_y)$ system presented in this thesis, has yielded valuable information which was very useful in giving better understanding of some aspects of the physical behaviour of this intriguing new class of materials called semimagnetic semiconductors.